IPPT Report on Fundamental Technological Research
3/2012

Yuriy Tasinkevych

Electrostatic methods in analysis of acoustic beam-forming structures

Institute of Fundamental Technological Research
Polish Academy of Sciences

Warsaw 2012

IPPT Reports on Fundamental Technological Research
ISSN 2299-3657
ISBN 978-83-89687-78-4

Recenzent:

prof. dr hab. inż. Adam Kawalec

Praca wpłynęła do redakcji 23 czerwca 2012 roku

Instytut Podstawowych Problemów Techniki Polskiej Akademii Nauk
Pawińskiego 5b, 02-106 Warszawa
Nakład 100 egz. Ark. wyd. 12
Oddano do druku w listopadzie 2012 roku

Druk i oprawa: EXPOL, P. Rybiński, J. Dąbek, Sp. J., Włocławek, ul. Brzeska 4

I owe a dept of gratitude to prof. E. Danicki for many helpful discussions, encouragement, for the vision and foresight which inspired me to conceive this work. It would not have been possible to accomplish this work without his warm support and concern. I am also particularly indebted to my parents for inspiring me to this work and to my wife and daughter which have always been a source of inspiration and motivation for me in the moments of despondency. It is also my duty to record my thankfulness to the Directorate of the Institute of Fundamental Technological Research of the Polish Academy of Sciences for financial support in publishing this work.

Yuriy Tasinkevych
Institute of Fundamental Technological Research
of the Polish Academy of Sciences

Abstract

The work aims to present extensions of the developed methods used in electrostatic analysis of planar periodic and finite systems for efficient solving of variety of the acoustic and electromagnetic wave generation and scattering problems. Specifically, their generalization for application in the acoustic beam-forming analysis is reported. Moreover, certain electromagnetic wave scattering problems by periodic waveguiding structures which can be efficiently approached by these methods are also considered.

The monograph consists of seven Chapters. The Chapter 1 presents the introduction where the main objectives of the work are outlined. Mathematical principles of the electrostatic methods which are dealt with in the following are presented in details in the Chapter 2. The cases of infinite periodic and finite aperiodic systems of infinitesimally thin electrodes (conducting strips), generally having arbitrary widths and spacings, are considered separately. In the Chapter 3 the electrostatic methods are generalized and extended to the acoustic beam-forming analysis by linear transducer arrays. The mixed boundary-value problem is stated and solved for the cases of infinite periodic and finite aperiodic arrays of rigid baffles. Also, the developed method of the angular directivity function evaluation for a linear transducer array with arbitrary excitation is presented. In the Chapters 4 and 5 several examples illustrating practical applicability of the developed methods are discussed. Specifically, in the Chapters 4 a developed modified multi-element synthetic transmit aperture algorithm for ultrasound imaging, which incorporates the developed method of linear transducer array modeling, is reported. And in the Chapter 5 a two-dimensional electrostrictive transducer array is analyzed. In the Chapter 6 generalization of the electrostatic methods to the electromagnetic wave scattering analysis is presented. Specifically, the problems of electromagnetic wave scattering by periodic gratings like a thick-walled parallel-plate waveguide array and a periodic system of conducting electrodes of finite thickness are considered. Finally, the Chapter 7 concludes the monograph.

Yuriy Tasinkevych
Instytut Podstawowych Problemów Techniki
Polskiej Akademii Nauk

Streszczenie

Podstawowym celem pracy jest przedstawienie opracowanych uogólnionych metod analizy zagadnień elektrostatyki układów planarnych zarówno periodycznych jak i nieperiodycznych, zawierających skończoną ilość elementów, do celów efektywnego rozwiązywania zagadnień brzegowych w teorii generacji i detekcji fal akustycznych oraz analizy zagadnień brzegowych w teorii fal elektromagnetycznych dla przypadku struktur falowodowych.

Monografia składa się z siedmiu Rozdziałów. Rozdział 1 stanowi wprowadzenie w którym omówiony został cel i zakres pracy. Matematyczne podstawy metod elektrostatyki, rozwijane i generalizowane w dalszej części monografii, zostały szczegółowo omówione w Rozdziale 2. Tu osobno rozpatrzono przypadki periodycznego oraz nieperiodycznego układów infinitezymalnie cienkich elektrod (przewodzących pasków), w ogólnym przypadku o różnych szerokościach oraz odstępach. W Rozdziale 3 przedstawiono uogólnienie metod elektrostatyki do analizy mieszanego zagadnienia brzegowego dla układów sztywnych przegród, zarówno periodycznych jak i zawierających skończoną ilość elementów, oraz zaprezentowano opracowany model analityczno-numeryczny do obliczania charakterystyki promieniowania liniowych szyków przetworników akustycznych dla dowolnego pobudzenia. Przykłady praktycznego zastosowania opracowanych metod przedstawione zostały w Rozdziałach 4 oraz 5. Mianowicie, w Rozdziale 4 zaprezentowano oryginalny nowoczesny algorytm wieloelementowej syntetycznej apertury nadawczej (ang. *multi-element synthetic transmit aperture*) dla obrazowania ultrasonograficznego w którym została zaimplementowana opracowana metoda modelowania liniowych szyków przetworników ultradźwiękowych. Z kolei w Rozdziale 5 przedstawiona została analiza modelu dwuwymiarowej macierzy przetworników elektrostrykcyjnych. W Rozdziale 6 przedstawiono uogólnienie metod elektrostatyki do analizy zjawisk rozpraszania fal elektromagnetycznych dla periodycznych struktur falowodowych takich jak periodyczny układ falowodów płaskich o grubych ściankach oraz periodyczny układ przewodzących elektrod o skończonej grubości. Na koniec, Rozdział 7 przedstawia podsumowanie monografii.

Symbols and abbreviations

The short list of most frequently used symbols and abbreviations is provided below:

ω, Ω – angular frequency
f – temporal frequency
f_0 – central frequency (of a transducer)
λ – wave-length
k – wave-number
Λ – period of strips (group of strips) or baffles (group of baffles)
K – spatial spectrum wave-number of periodic array of strips (baffles)
P_k – Legendre polynomials of the first kind
J_k – Bessel function of the first kind of order k
Γ – gamma function
ϕ – electrostatic or acoustic potential
Q – electrostatic charge
V – potential difference (voltage between strips)
σ – surface charge distribution
x, y, z – Cartesian space variables
ϵ_0 – dielectric permittivity of vacuum
ϵ – effective surface dielectric permittivity
μ_0 – magnetic permeability of vacuum
E_i – components of electric field, $i = x, y, z$
H_i – components of magnetic field, $i = x, y, z$
D_i – components of electric induction, $i = x, y, z$
$G(\xi)$ – planar harmonic Green's function
$\Phi(\xi)$ – spectrum representation of the complex (electrostatic) field function
$\Phi(x)$ – spatial representation of the complex (electrostatic) field function

d – strip half-width
r, s – spectral variables related to the x, y spatial coordinates constrained to one Brillouin zone
$\mathcal{F}$ – Fourier transform
p – acoustic pressure
ρ_a – mass density of the acoustic media
v_z – z-component (normal component) of the particle velocity
Π – acoustic power
Π_z – normal component of the acoustic Poynting vector

SAW – surface acoustic wave
IDT – interdigital transducer
BIS expansion – Blotekjœr, Ingebrigtsen, and Skeie expansion method
FFT – fast (finite) Fourier transform
SNR – signal-to-noise ratio
SA – synthetic aperture
SAFT – synthetic aperture focusing technique
M-SAFT – multi-element synthetic aperture focusing technique
STA – synthetic transmit aperture
MSTA – multi-element synthetic transmit aperture
TM – transverse magnetic wave polarization
TE – transverse electric wave polarization

Contents

1

Introduction

Beam-forming is one of the prevailing signal processing techniques having long history in applications such as radars (electromagnetic wave beam-forming) or sonars (acoustic wave beam-forming). It is usually implied that beam-former is a system which consists of certain phased array of elements which receive or transmit waves and advanced post-processing capabilities. As regards applications in acoustics, a typical beam-forming structures are phased array transducers. Nowadays they are indispensable parts in applications, for example, in medical ultrasound diagnostics where they are exploited with great success for a long time [1, 2]. The nondestructive evaluation and testing is another area where the ultrasonic phased arrays have been receiving great attention recently [3–9]. The inspection speed and fast imaging capabilities, flexible control and signal processing give rise to their advantages over conventional ultrasonic transducers. A typical linear ultrasonic array transducer consists of the alternate sets of acoustically different materials: piezoelectric, which responds to the incident waves by electric signal, and acoustically isolating material (like epoxy) between them. The wave-field excitation by the individual elements of the array with properly chosen strengths and phases allows to realize the beam steering and focusing as well as proper beam shape of the wave radiated into the body. Compact realization of the beam-forming idea developed in microwaves [10] appears to be also perspective for ultrasound applications, exploiting integrated acoustic wave-guides. In the case of receiving transducer arrays, the corresponding spatial filtration is adopted by summing up of signals of the transducer elements with proper weights and phases [11]. In further approximation, the point-like sources are replaced by periodic baffles; such system has been investigated for example in [12].

Different methods of the linear phased array modeling are described in the literature. Among them the most frequently used the beam profile modeling [13] and point spread function modeling [14]. The beam profile modeling is based on the intuitive representation of the array as a set of simple point sources [15]. In the point spread function modeling [16] the ability of the imaging system

which exploits phased array transducer to visualize a point reflector (by means of certain imaging algorithm) is modeled. For this purpose the ultrasonic data from the array due to a point reflector at a particular spatial position are simulated first. Then the image of the reflector is plotted using the appropriate imaging algorithm applied to the simulated data. Both these methods must apply certain model of the individual element of the array (they are typically piezoelectric strips separated by epoxy layers). There are different methods of modeling the array element, including finite element analysis [17–19] or Huygens principle [20–22]. In the later case, usually the integration of a series of point or line sources is performed to obtain the element directivity function due of the finite size of the array element. The above approaches to modeling the array transducer assume that the individual elements respond to the incident wave pressure independently of each other yielding the electric signal proportional to the incident wave amplitude. However, since piezoelectric materials are closer to hard, and epoxy is closer to soft acoustic materials, the Bragg scattering occurs when the incident wave scatters from the array. This phenomenon necessarily distorts the local acoustic pressure on piezoelectric elements of the array affecting its electric response.

In this study the alternative approach for modeling the ultrasonic linear array transducer is developed, which is based on the rigorous full-wave analysis of the corresponding boundary-value problem for wave excitation or scattering. The considered system, modeling a transducer array, consists of periodic acoustically hard strips (baffles) where the normal acoustic vibration vanishes [23], and between them there are acoustically soft domains where the acoustic pressure vanishes (or it is given constant in the excitation problem). It should be noted, that in the classical formulation of the scattering problem, which can be found for example in [24], the reflected and transmitted wave-fields are of primary interest and the problem is solved using Green's theorem. The unknown field on strips is represented by the series of Chebyshev polynomials, and using the Galerkin method the problem is reduced to a certain system of linear algebraic equations for unknown expansion coefficients. The scattered field (transmitted and reflected waves) is finally found as a superposition of infinite number of spatial harmonics. What is considered here is mixed (Dirichlet-Neumann) boundary-value problem formulated as follows: the given pressure between baffles models the wave-beam generation, and the pressure exerted by the incident and scattered waves on the acoustically hard baffles models the response signal from the individual piezoelectric element of the array transducer. Efficient tools for rigorous solution of the above-mentioned problems can be delivered by the methods worked out earlier in electrostatics of planar systems of strips [25–28].

These methods are further investigated and developed in this study for application in acoustic beam-forming analysis.

Electrostatic analysis of planar systems of perfectly conducting strips may explain fundamental features of microwave [29] and micro-acoustic [25] devices. It also provides the approximated solution to diffraction problems in a long-wavelength limit [30]. In this case the induced electric charge distribution on strips varies according to the incident electric field. In classical electrostatics, the boundary value problem is formulated for electric field or its potential governed by the Laplace equation appended by the boundary conditions on the system of strips. The solution provides the electric field in the space around strips and the electric induction (the electric charge density) distribution on their surface [31]. Another approach exploits the theory of complex functions [32]. Both these methods, however, are not applicable for the acoustic beam-forming analysis considered in this study. Here, instead, another approach is presented - the spectral theory [33]. This is a different method for direct evaluation of the spatial spectrum of the charge distribution on planar system of strips. The charge spatial distribution itself can be obtained by the inverse Fourier transformation if needed. In many applications, like extensions of the electrostatic methods for the acoustic beam-forming analysis which are studied here, the spatial spectrum of charge distribution is the quantity of invaluable importance (e.g. for modeling of the frequency response of SAW transducers, beam pattern of acoustic transducers etc.).

In the case of planar system of periodic strips having arbitrary potentials or charge distributions, the spectrum can be obtained using the so-called generalized 'BIS-expansion' method [34]. The approach exploits certain properties of the series of Legendre polynomials in order to satisfy the boundary condition in the consider boundary-value problem. The method was first introduced by **B**lotekjœr, **I**ngebrigtsen, and **S**keie [34] and was referred to as the BIS-expansion method. The detailed discussion concerning the BIS-expansion method and its generalization will be presented in details further in the Chapter 2. The method was also successfully used in the theory of electromagnetic wave scattering by planar systems of periodic conducting strips [35], in the theory of elastic wave scattering by periodic cracks [36], and in generalized form in the theory of surface acoustic wave transducers [37].

For a finite system of strips, generally having arbitrary widths and spacings, in the spectral theory approach a set of the so-called spectral 'template functions', being independent solutions to the charge distributions on the plane of strips expressed in the spectral domain, is defined. The general solution is built up as a superposition of them. To find a particular solution a set of circuit

equations (constraints) is specified which have to be satisfied: given strip potentials or charges, or interconnections [38]. The same set of template functions is used to find the solution of the complementary problem of strips in external spatially variable (harmonic) electric field. This makes the problem analogous to the wave scattering one and thus justifies the application of wave-scattering terminology (like 'radiation conditions', for instance). This method is discussed in details in the Chapter 2.

The main objective of the work is to develop the extensions of the above electrostatic methods for application in acoustic beam-forming analysis, or more specifically, for solving of the afore-mentioned boundary value problems for baffle arrays. To this end a proper generalization of both the BIS-expansion and template functions approaches will be developed and discussed to find the rigorous solution of the boundary-value problem in the case of planar periodic and arbitrary aperiodic finite system of baffles, respectively. The presented methods allow to reduce the initial problem to the small system of linear equations to be solved numerically, and yields the results which satisfy exactly the energy conservation law (with machine accuracy [36, 39]), in both the generation and scattering cases. These problems are studied in details in the Chapters 3-5. There are also given some other interesting examples of application of the developed methods. Namely, in the Chapter 4 a practical implementation of the discussed methods for the performance improvement of the multi-element synthetic transmit aperture (MSTA) method for ultrasound imaging applications is considered [40]. There the results of beam-forming analysis expounded in the Chapter 3 are exploited to develop a set of apodization weights accounting for the transmit and receive aperture directivities in the modified MSTA method. This allows considerably improve the contrast and visualization depth of the final ultrasound images. On the other hand, in the Chapter 5 a 2D transducer array comprised of crossed arrays of electrodes located on the opposite surfaces of thin electrostrictive dielectric is briefly referred following [41]. Such a structure is capable of electronic beam-steering of generated wave-beam both in elevation and azimuth. The wave-beam control is achieved by addressable driving of two-dimensional matrix transducer through proper voltage supply of electrodes on opposite surfaces of the layer.

Furthermore, it appears that the problems of acoustic beamforming analysis are not the only ones which can be successfully treated by the generalized electrostatic methods. Their applicability to a wide range of physical phenomena is illustrated in the further Chapters of the work. Namely, a variety of electromagnetic wave generation and scattering problems can be addressed by these methods. These generalization of the electrostatic methods based on BIS-expansion

are further developed and presented in the Chapter 6 where the problem of electromagnetic wave scattering by the periodic structures like thick-walled parallel-plate waveguide array [42, 43] and a grating comprised of thick conducting bars, widely used in applications, are considered [44]. Electromagnetic scattering and radiation by periodic systems is a classical problem of diffraction theory. From the theoretical point of view it gives a perfect example for the study of periodic structures. In the practical aspect the perfectly electric conductor periodic structures can simulate the phased arrays in micro an millimeter wave applications, such as filters [45, 46], frequency selective structures [47, 48], splitters and antennas [49, 50], widely used in today's communication and radar systems [51, 52]. Recently, periodic systems with a particular arrangement of scatterers including conductors and dielectrics has received growing attention, because such the systems may behave like negative refractive index materials [53, 54] within a certain frequency range. Many approaches [55, 56] have been proposed to analyze them, such as the mode-matching method, finite difference time domain (FDTD) technique, finite element method (FEM) or Fourier series method. In this study the problem of electromagnetic wave scattering by the above-mentioned periodic structures are efficiently solved using a method similar to the BIS-expansion. In particular, a series of spatial harmonics is exploited for scattered field representation and the corresponding mode amplitudes are further expanded into the series of properly chosen Legendre functions (following a similar procedure as in the BIS-expansion method).

Another vivid and interesting example is the electrostatic analysis of the planar system of strips with 'broken' periodicity originating from an infinite periodic system by inclusion of the narrower strip and spacing in the middle of the system [57]. This breaks the system periodicity making it 'quasi-periodic', as the system remains periodic outside of the inclusion. The defective periodic structures are known in physics; they are used in the Fabry-Perot resonators of solid-state lasers, for instance. The method of analysis of such structures is also developed and demonstrated in this study. It presents a generalization of the BIS-expansion method (suitable for periodic structures) and 'template functions' approach (suitable for non-periodic finite structures) and illustrates well the versatility and flexibility of electrostatic methods which are dealt with in this study.

The work is organized in the following way. In the next Chapter the mathematical principles of electrostatic methods are discussed in details. The cases of infinite periodic and finite aperiodic (generally having arbitrary widths and spacings) planar systems of perfectly conducting strips are considered separately. In this Chapter a peculiar example of a finite planar system of strips in

external (harmonic) electric field is presented. The problem is studied using a method combining both the BIS-expansion and 'template functions' approaches (see Section 2.4.). In the Chapter 3 the electrostatic methods are generalized and extended to the analysis of the acoustic linear array transducers. The mixed boundary-value problem mentioned above is solved for the cases of infinite periodic as well as for finite array of baffles separately in Sections 3.2. and 3.3. In the Chapters 4 and 5 several examples illustrating practical applicability of the developed methods of analysis are discussed. In particular, in the Chapter 4 the developed modified MSTA method for ultrasound imaging is presented and in the Chapter 5 the 2D electrostrictive transducer array is analyzed using the generalized extension of the BIS-expansion method for 2D periodic structures. Finally, in the Chapter 6 generalization of electrostatic methods to the electromagnetic wave scattering analysis is presented.

2

Mathematical principles of electrostatic methods

In this Chapter the fundamentals of electrostatics of planar system of perfectly conducting strips are discussed in details. The variety of methods can be found in literature ranging from purely theoretical, based on the theory of analytic functions [32] and up to the numerical ones, exploiting the finite element method, for example [31]. In this study, however, the advantages will be taken from the so-called spectral theory approach [33] which not only delivers the direct solution of electrostatic problem in the spatial spectrum domain (which is extremely important in many practical applications) but also is as much flexible and versatile that can be easily generalized for successful treatment of numerous problems of acoustic (as well as electromagnetic) wave generation and scattering theory. For the sake of clarity it is convenient to consider separately the cases of infinite periodic and finite aperiodic planar systems of conducting strips. Therefore, in the Section 2.2. the BIS-expansion [34] method will be presented first. It is suitable for the case of infinite periodic arrays. Originally it was proposed and used to solve electrostatic problems related to modeling surface acoustic wave interdigital transducer [34]. The method was further successfully used in the analysis of electromagnetic wave scattering by periodic planar system of conducting strips [35] and in the theory of elastic wave scattering by periodic system of cracks [36]. The theoretical background of the BIS-expansion method is outlined in the Section 2.2.1. In the case of finite aperiodic planar system of strips, generally having arbitrary widths and spacings or kerfs (term 'kerf' is widely exploited in the literature related to the acoustic transducers), the so-called 'template functions' method is used [38] in the frame of spectral approach. It is discussed in details in the Section 2.3. The template functions are particular solutions of the corresponding boundary value problem. Their linear combination determines the general solution, and unknown coefficients are determined from the constraints resulting from circuit equations (given voltages, charges

or strips interconnections). And, finally, in the Section 2.4. a generalization of electrostatic methods combining both the BIS-expansion method and template functions method which is suitable for solving the problem of planar system of strips in external, spatially harmonic, field is presented. This problem is similar to the wave scattering one. The developed method will be helpful in further analysis of the of acoustic wave generation and scattering problems presented in Chapter 3. But at the very beginning it is worthwhile to give some basic introduction into the electrostatics of planar systems which is briefly referred in the next Section.

2.1. Basic solution for planar systems

In classical electrostatics the boundary value problem is formulated for electric field or its potential, governed by the Laplace equation and the boundary conditions on the surface of conducting body. The conducting body is actually a system of in-plane perfectly conducting and infinitesimally thin strips (periodic or finite, having arbitrary width and spacing). The solution provides the electric field in the space around the body and the electric induction (the electric charge density) distribution on the body surface. Evaluation of the spatial spectrum of electric charge distribution is then perform by spatial Fourier transform, usually by means of the Fast Fourier Transform (FFT) algorithm. Although the charge distribution and its spatial spectrum are simply related by the Fourier spatial transform, the transformation direct evaluation poses a serious practical problem due to the square-root singularity of the charge distribution on strips (note that there can be tens or even hundreds of strips in the analyzed structures, the spatial spectrum in such cases depends strongly on all these singularities). Moreover, wide domain of the spectrum is interesting for applications, even spanned over several fundamental harmonics (corresponding to transducer overtones). Naturally, the numerical results can only be obtained, and attempting to perform the Fourier transformation, one have to sample the singular field at discrete values of the spatial variable, what inevitably leads to significant numerical errors, even if the field is perfectly evaluated.

This drawback is eliminated in the spectral approach considered here. This means, that the main purpose of the method is to evaluate the spatial spectrum of the electric charge distribution directly, formally without an earlier evaluation of the charge spatial distribution with subsequent application of the FFT algorithm. The integrals of the field and induction are only necessary for evaluation of the strip potentials and charges in order to formulate the equations resulting

from the circuit theory (the Kirchhoff's laws), taking into account that some strips have given potentials, others can be isolated or interconnected. To proceed further with the methods of analysis of planar systems of strips, a brief introduction to the corresponding electrostatics basics connected with this problems is presented below.

Let a harmonic potential on the plane $z = 0$, assumed independent of y, be of the form $e^{-j\xi x}$, where ξ is an arbitrary spatial spectral variable of real value corresponding to the x spatial coordinate (see Fig. 2.1). On the basis of the Laplace equation for the potential of electric field $\vec{E} = -\nabla\varphi$:

$$\Delta\varphi = 0, \tag{2.1}$$

it is seen that the z-dependence of the solution for φ vanishing with growing distance from the plane $z = 0$ (in the other words, satisfying the equivalent 'radiation condition' in the wave-scattering terminology) is $e^{-|\xi z|}$.

Assuming a dielectric permittivity of the surrounding media to be ϵ_e (for example it can be vacuum with dielectric constant ϵ_0), the following equations for the field components, as a function of spectral variable, are obtained on the plane $z = 0+$ (just above the plane)

$$E_x(\xi) = j\xi\varphi(\xi),\ D_z = \epsilon E_z(\xi) = \epsilon\xi S_\xi\varphi(\xi),\ \epsilon = 2\epsilon_e, \tag{2.2}$$

where $S_\xi = 1$ for $\xi \geq 0$ and -1 otherwise ($\xi S_\xi = |\xi|$); ϵ - is an effective surface permittivity [58]. In Eq. (2.2) a typical notation for the electric field vector E_x and electric induction D_z is applied.

It is convenient to introduce the planar harmonic Green's function [37, 59]

$$G(\xi) = E_x(\xi)/D_z(\xi) = jS_\xi/\epsilon, \tag{2.3}$$

defined for the tangential electric field E_x and normal electric induction D_z on the plane $z = 0$, which components vanish at $|z| \to \infty$. The other, complementary class of the field, satisfying the opposite condition:

$$E_x^I(\xi) = -G(\xi)D_z^I(\xi), \tag{2.4}$$

that is growing at infinity, will be exploited further in the problem of strips in external spatially harmonic electric field; E_x^I, D_z^I denote the components of the external or 'incident' field which source resides outside the planar structure, at infinity. The Green's function $G(\xi)$ will replace the Laplace equation in all the analysis that follows for the fields on the plane $z = 0$. In the spectral approach described here the concept of the so-called 'complex field function'

plays fundamental role in the numerical analysis. It is defined in the following way:

$$\Phi \equiv E_z - jE_x = D - jE \tag{2.5}$$

both in spectral and spatial domain. To simplify notation and to emphasize the fundamental importance of the spatial spectrum of the surface charge distribution, determined by the jump discontinuity of the normal electric induction D_z, the new variables $E = E_x$ and $D = D_z/\epsilon = E_z$ were introduced in Eq. (2.5) and will be exploited in the following (the exception is the Sec. 2.2.1., where $D = D_z$, which is annotated explicitly there). This is equivalent to the proper choice of the units for electric induction (which makes $\epsilon = 1$). In what follows, the independent variable will be written explicitly to avoid ambiguity, if needed; otherwise, if it is clear from the context whether the spectral representation or its spatial counterpart is meant, the independent variable will be dropped to shorten notation. Taking into account the definition of the Green's function, Eq.(2.3), one obtains the fundamental property of the spectral representation of the complex field:

$$\Phi(\xi) = 0,\ \xi < 0, \tag{2.6}$$

which property considerably simplifies the numerical analysis (it is discussed in details in the following). To illustrate the idea of the complex field function, the following example is considered. Namely, the simplest conducting body, for which the analytic solution of electrostatic problem can be found is a conducting half-plane (see Fig. 2.1). It is known [60] that the charged half-plane $x < 0$

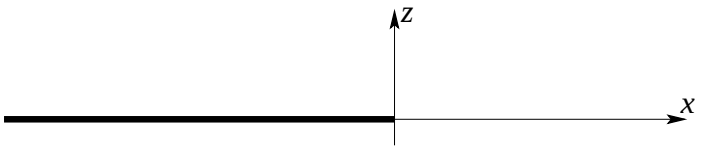

Figure 2.1. A perfectly conducting charged half-plane $z = 0$, $x < 0$

induces the following field on the plane $z = 0+$:

$$\begin{aligned} E^{(0)}(x) &= \begin{Bmatrix} 1/\sqrt{x}, & x > 0 \\ 0, & x < 0 \end{Bmatrix}, E^{(0)}(\xi) = \frac{1}{2\sqrt{\pi|\xi|}} \begin{Bmatrix} e^{j\pi/4}, \xi > 0 \\ e^{-j\pi/4}, \xi < 0 \end{Bmatrix}, \\ D^{(0)}(x) &= \begin{Bmatrix} 0, & x > 0 \\ 1/\sqrt{-x}, & x < 0 \end{Bmatrix} D^{(0)}(\xi) = \frac{1}{2\sqrt{\pi|\xi|}} \begin{Bmatrix} e^{-j\pi/4}, \xi > 0 \\ e^{j\pi/4}, \xi < 0 \end{Bmatrix}, \end{aligned} \tag{2.7}$$

in the spatial, and spectral representations. The complex field function for the

half-plane, therefore, is:

$$\begin{aligned}\Phi^{(0)}(x) &= \frac{1}{\sqrt{-x}} = \left\{ \begin{array}{ll} -j/\sqrt{|x|}\,, & x>0 \\ 1/\sqrt{|x|}\,, & x<0 \end{array} \right\}, \\ \Phi^{(0)}(\xi) &= \left\{ \begin{array}{ll} e^{-j\pi/4}/\sqrt{\pi\xi}, & \xi>0, \\ 0, & \xi<0 \end{array} \right\}. \end{aligned} \tag{2.8}$$

The square-root value is chosen to be positive for $x \geq 0$, and $\sqrt{-1} = j$ otherwise. The above follows the well-known electrostatic theorem that real and imaginary parts of any harmonic function represent a solution of certain electrostatic problem. The appropriate boundary conditions considered here:

$$\begin{aligned} &E(x) = 0, \quad \text{on the conducting body} \\ &D(x) = 0, \quad \text{outside the conducting body} \end{aligned} \tag{2.9}$$

are appended by the condition that the field vanishes at $|z| \to \infty$ (analogous to the 'radiation condition' in the wave-scattering theory). Besides, the electric field exhibits square-root singularity near the strips edges (it will be referred to as the edge conditions, in what follows) [61]:

$$\begin{aligned} &E = O(\rho^{-1/2}),\ D = O(\rho^{-1/2}),\ i = x, z, \\ &\rho \to 0, \rho = \left((x \pm d)^2 + z^2\right)^{1/2}. \end{aligned} \tag{2.10}$$

This idea is exploited in the further analysis. Concerning the spectral representation, it is very important to note that it has a semi-finite support. Namely, it results from Eq. (2.3) that $\Phi(\xi) = D(\xi) - jE(\xi) = (1 + S_\xi)D(\xi)$ that is zero for $\xi < 0$, for fields satisfying the radiation condition, Eq. (2.3). The definition (2.5) has been chosen to obtain the convenient support $\xi \geq 0$. For given $\Phi(\xi)$, the representation of D and E in spectral domain can be inferred from the above results as

$$\begin{aligned} D(\xi) &= \frac{1}{2} \left\{ \begin{array}{ll} \Phi(\xi), & \xi \geq 0 \\ \Phi^*(-\xi), & \xi < 0 \end{array} \right\}, \\ E(\xi) &= jS_\xi D(\xi) = \frac{j}{2} \left\{ \begin{array}{ll} \Phi(\xi), & \xi \geq 0 \\ -\Phi^*(-\xi), & \xi < 0 \end{array} \right\}, \end{aligned} \tag{2.11}$$

which can be easily checked by substitution to Eq. (2.5) and (2.3). Moreover, functions $\{D(\xi - \nu), E(\xi - \nu)\}$ are constituents of another harmonic function $[D(x) - jE(x)]\mathrm{e}^{-j\nu x}$ satisfying Eq. (2.1), but not necessarily Eq. (2.3) (this will be exploited later in the Section 2.4.)

2.2. Electrostatics of periodic system of strips

Let's now consider the case of infinite Λ-periodic system of perfectly conducting strips of width $2d$, as shown in Fig. 2.2. The spatial complex field function

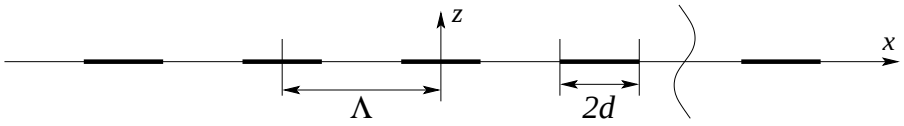

Figure 2.2. A Λ periodic system of conducting strips of width $2d$ placed on the plane $z = 0$.

$\Phi(x)$ results from the known identity (see Eq. (3.10.2) in [62]):

$$\sum_{n=0}^{\infty} P_n(\cos\theta)\cos\left(n+1/2\right)v = \begin{cases} \dfrac{1}{\sqrt{2\left(\cos v-\cos\theta\right)}}, & 0 \le v < \theta, \\ 0, & \theta < v < \pi, \end{cases} \qquad (2.12)$$
$$0 < \theta < \pi,$$

where P_ν are the Legendre polynomials. Applying Euler formula for cosine function, the sum in Eq. (2.12) can be rewritten as follows:

$$\sum_{n=0}^{\infty} P_n(\cos\theta)\cos\left(n+1/2\right)v = \frac{1}{2}\sum_{n=0}^{\infty} P_n(\cos\theta)e^{j(n+1/2)v} + \frac{1}{2}\sum_{n=0}^{\infty} P_n(\cos\theta)e^{-j(n+1/2)v} = \qquad (2.13)$$
$$\frac{1}{2}e^{-jv/2}\left(\sum_{n=0}^{\infty} P_n(\cos\theta)e^{j(n+1)v} + \sum_{n=0}^{\infty} P_n(\cos\theta)e^{-jnv}\right).$$

The first sum in brackets can be further transformed by introducing a new summation index $p = -n - 1$:

$$\sum_{-\infty}^{p=-1} P_{-p-1}\left(\cos\theta\right)e^{-jpv} = \sum_{-\infty}^{p=-1} P_p\left(\cos\theta\right)e^{-jpv}. \qquad (2.14)$$

In Eq. (2.14) the known property of the Legendre polynomials $P_{-p-1} = P_p$ was exploited. Reverting to the previous summation index in the above expression, and substituting it together with Eq. (2.13) into Eq. (2.12), after straightforward

rearrangement of terms, one finally obtains:

$$\sum_{n=-\infty}^{\infty} P_n(\cos\theta)\, e^{-jnv} = \begin{cases} \dfrac{\sqrt{2}e^{jv/2}}{\sqrt{\cos v - \cos\theta}}, & 0 \le v < \theta, \\ 0, & \theta < v < \pi. \end{cases} \tag{2.15}$$

Another expansion, similar to Eq. (2.15), can be deduced if one substitutes $\theta \to \pi - \theta$, $v \to \pi - v$ in place of θ and v into Eq. (2.12), which yields:

$$\sum_{n=0}^{\infty} P_n(-\cos\theta)\cos(n+1/2)(\pi - v) = \begin{cases} 0, & 0 \le v < \theta, \\ \dfrac{1}{\sqrt{2(\cos\theta - \cos v)}}, & \theta < v < \pi, \end{cases} \tag{2.16}$$

Repetition of the same steps as above (see Eqs. (2.13), (2.14)) results in the following expansion (here the property of Legendre polynomials $P_n(-x) = (-1)^n S_n P_n(x)$ is exploited additionally):

$$\sum_{n=-\infty}^{\infty} S_n P_n(\cos\theta)\, e^{-jnv} = \begin{cases} 0, & 0 \le v < \theta, \\ \dfrac{-j\sqrt{2}e^{jv/2}}{\sqrt{\cos\theta - \cos v}}, & \theta < v < \pi. \end{cases} \tag{2.17}$$

The expansions given by Eqs. (2.15) and (2.17) can be successfully used to represent the components of electric field on the plane of strips $z = 0$ (see Fig. 2.2). For this purpose it is convenient to substitute the new variables instead of v and θ as follows: $v \to Kx$, where $K = 2\pi/\Lambda$ is the spatial wave-number of the periodic system, and $\theta \to \Delta$, where $\Delta = Kd$. Replacing the variables in Eqs. (2.15) and (2.17) and multiplying the equations by the exponential term e^{-jrx}, where $r \in (0, K)$ is a spectral variable related to the x spatial coordinate and constrained to one Brillouin zone for the sake of uniqueness of the representation, (note, ξ is defined in the entire spectral domain) the following expressions for the normal electric induction $D(x)$ and tangential electric field

$E(x)$ vector on the plane of strips can be obtained:

$$D(x)=\sum_{n=-\infty}^{\infty} P_n(\cos\Delta)e^{-j\xi_n x}=\begin{cases}\dfrac{\sqrt{2}e^{-j(r-K/2)x}}{\sqrt{\cos Kx-\cos\Delta}}, & |x|<d,\\ 0, & d<|x|<\dfrac{\Lambda}{2},\end{cases}$$
$$E(x)=\sum_{n=-\infty}^{\infty} jS_nP_n(\cos\Delta)e^{-j\xi_n x}=\begin{cases}0, & |x|<d,\\ \dfrac{\sqrt{2}S_xe^{-j(r-K/2)x}}{\sqrt{\cos\Delta-\cos Kx}}, & d<|x|<\dfrac{\Lambda}{2}.\end{cases} \tag{2.18}$$

In the above $\xi_n = r + nK$ was introduced. It should be noted that the functions defined by expansions on the left-hand side in Eqs. (2.15) and (2.17) are well defined for either positive or negative v. If one replace v with $-v$, the corresponding left-hand side counterpart remains unchanged if its value is real (that is for $0 \le v < \theta$) or changes its sign in the other case (for $\theta < v < \pi$). This explains the introduction of S_x in Eqs. (2.18) and extension of the expansion to the negative values of Kx. The partial solution for electrostatic field represented by Eqs. (2.18) obeys the boundary and edge conditions on the plane of strips specified by Eq. (2.9) and Eq. (2.10), respectively. The spatial spectrum representations $D(\xi)$ and $E(\xi)$, defined on the entire ξ-axis, immediately result from Eq. (2.18) (and taking into account Eq. (2.3)) [58]:

$$D(\xi) = P_{\lfloor \xi/K \rfloor}(\cos\Delta),\ E(\xi) = jS_\xi D(\xi) = jS_\xi P_{\lfloor \xi/K \rfloor}(\cos\Delta). \tag{2.19}$$

(note, $S_n = S_{nK+r}$ for $r \in (0, K)$) $\lfloor k/K \rfloor$ is an integer floor of k/K. From Eqs. (2.18) using Eq. (2.5) the complex field function in the spatial domain is

$$\Phi(x) = D(x) - jE(x) = 2\sum_{n=0}^{\infty} P_n(\cos\Delta)e^{-j\xi_n x},\ \xi_n = r + nK, \tag{2.20}$$

and it spatial spectrum counterpart obtained from Eq. (2.19)

$$\Phi(\xi) = D(\xi) - jE(\xi) = 2P_{\lfloor \xi/K \rfloor}(\cos\Delta),\ \xi \ge 0 \tag{2.21}$$

has semi-finite support with respect to the spectral variable ξ (see Eq. (2.6) of the previous Section). Using the spatial representations of the electric field, Eq. (2.18), the strip charges and potentials can be easily evaluated. Consider a strip centered at the spatial point $x_i = i\Lambda$. Integration of the first equation of

Eq.(2.18) with respect to x over the interval $(i\Lambda - d, i\Lambda + d)$ yields:

$$Q_i(r) = Q_r e^{-jri\Lambda}, \;\; Q_r = \epsilon \int_{-d}^{d} D(x)dx = \epsilon \int_{-\Lambda/2}^{\Lambda/2} \sum_{n=-\infty}^{\infty} P_n(\cos\Delta) e^{-j\xi_n x} dx. \tag{2.22}$$

Changing the order of summation and integration an integrating term by term one obtains:

$$Q_r = 2\epsilon \sin(\pi r/K) \sum_{n=-\infty}^{\infty} \frac{(-1)^n P_n(\cos\Delta)}{\xi_n}. \tag{2.23}$$

Note, that integration in Eq. (2.22) is performed over entire period since $D(x) = 0$ outside the domain occupied by the strip. Similarly, the value of the integral in the second equation of Eq. (2.18) at the point $x_i = i\Lambda$ yields the potential of the strip:

$$\varphi_i(r) = \varphi_r e^{-jri\Lambda}, \;\; \varphi_r = -\int E(x)dx|_{x=0} = -j \int \sum_{n=-\infty}^{\infty} S_n P_n(\Delta) e^{-j\xi_n x} dx|_{x=0}. \tag{2.24}$$

Integration of Eq.(2.24) term by term yields:

$$\varphi_r = \sum_{n=-\infty}^{\infty} \frac{S_n P_n(\cos\Delta)}{\xi_n}. \tag{2.25}$$

The sums in Eqs. (2.23), (2.25) can be evaluated analytically using the following (Dougall) identity (see Eq. (3.10.2) in [62]):

$$P_\nu(\cos\theta) = \frac{\sin\nu\pi}{\pi} \sum_{n=0}^{\infty} (-1)^n \left(\frac{1}{\nu - n} - \frac{1}{\nu + n + 1} \right) P_n(\cos\theta), \tag{2.26}$$

valid for $-\pi < \theta < \pi$. Introducing a new summation index $p = -n - 1$ in the second sum in brackets, Eq. (2.26) can be rewritten as follows:

$$P_\nu(\cos\theta) = \frac{\sin\nu\pi}{\pi} \left(\sum_{n=0}^{\infty} \frac{(-1)^n P_n(-\cos\theta)}{\nu - n} - \sum_{p=\infty}^{-1} \frac{(-1)^{-p-1} P_{-p-1}(-\cos\theta)}{\nu - p} \right). \tag{2.27}$$

Using the known property of Legendre polynomials $P_{-p-1} = P_p$, already exploited for derivation of Eqs. (2.15), (2.18), and reverting to the previous summation index, after simple rearrangement of terms the above equation can be transformed to:

$$P_{-\nu}(\cos\theta) = -\frac{\sin\nu\pi}{\pi}\sum_{n=-\infty}^{\infty}\frac{(-1)^n P_n(\cos\theta)}{n+\nu}. \tag{2.28}$$

In a similar manner, starting with Eq. (2.26) and using the property of Legendre polynomials $P_n(-x) = (-1)^n S_n P_n(x)$ one obtains:

$$P_{\nu}(\cos\theta) = \frac{\sin\nu\pi}{\pi}\left(\sum_{n=0}^{\infty}\frac{P_n(-\cos\theta)}{\nu-n} - \sum_{n=0}^{\infty}\frac{P_n(-\cos\theta)}{\nu+n+1}\right). \tag{2.29}$$

Repetition of the same steps as above, namely, introducing the summation index $p = -n-1$, using the property $P_{-p-1} = P_p$ and reverting previous summation index, followed by simple rearranging the terms, yields:

$$P_{-\nu}(-\cos\theta) = -\frac{\sin\nu\pi}{\pi}\sum_{n=-\infty}^{\infty}\frac{S_n P_n(\cos\theta)}{n+\nu}. \tag{2.30}$$

Expansions on the right-hand sides of Eqs. (2.28), (2.30) are analogous to those in Eqs. (2.23), (2.25), respectively. Substitution of Eq. (2.28) into Eq. (2.23) (with $\cos\theta = \cos\Delta$ and $\nu = r/K$) yields:

$$Q_r(r) = -\epsilon\Lambda P_{-r/K}(\cos\Delta). \tag{2.31}$$

Similarly, substituting Eq. (2.30) into Eq. (2.25), one obtains:

$$\varphi_r(r) = -\frac{\pi}{K}\frac{P_{-r/K}(-\cos\Delta)}{\sin(\pi r/K)}. \tag{2.32}$$

Note, that both Q_r and φ_r are the functions of the reduced spectral variable r. They in fact can be interpreted as the Fourier transforms of discrete functions Q_i and φ_i taking values at the strip centers $x_i = i\Lambda$. In real systems some of the strips may have given potentials while the rest of them are grounded (zero potential). The solution for arbitrary distribution of strip potentials along the system can still be obtained using the superposition principle over the domain of $r \in (0, K)$ with some weighting function $\alpha(r)$ defined for $r \in (0, K)$:

$$\varphi_i = \frac{1}{K}\int_0^K \alpha(r)\varphi_r(r)e^{-jri\Lambda}dr = \varphi_l\delta_{li}, \tag{2.33}$$

where δ is the Kronecker delta, φ_l is the given (specified) potential of the strip centered at $x_l = l\Lambda$. Applying $\alpha(r)$ in the form:

$$\alpha(r) = \varphi_l \frac{e^{jrl\Lambda}}{\varphi_r(r)} \tag{2.34}$$

Eq. (2.33) can be satisfied directly, because the integral is zero for $i \neq l$, and it is φ_l for $i = l$. The function $\alpha(r)$ modifies the spatial spectrum of the electric charge distribution on the plane of strips:

$$Q(r) = \alpha(r) Q_r. \tag{2.35}$$

It yields the charge of the strip centered at $x_i = i\Lambda$ which results from the given potential applied to the strip centered at $x_l = l\Lambda$:

$$\begin{aligned} Q_i = \frac{1}{K} \int_0^K Q(r) e^{-jri\Lambda} dr = \\ \frac{2\epsilon}{K} \varphi_l \int_0^K \frac{P_{-r/K}(\cos\Delta)}{P_{-r/K}(-\cos\Delta)} e^{-jr(i-l)\Lambda} \sin(\pi r/K)\, dr. \end{aligned} \tag{2.36}$$

Another formulation of electrostatic problem can be stated in terms of given charges Q_l and the resulting voltages between neighboring strips, $V_i = \varphi_{i+1} - \varphi_i$ are treated as unknown quantities. The spatial spectrum representation of the voltages V_i is then given by:

$$V_r = \varphi_r e^{-jr\Lambda} - \varphi_r = j\Lambda P_{-r/K}(-\cos\Delta) e^{-j\pi r/K}. \tag{2.37}$$

The weighting function $\alpha(r)$ in this case can be deduced from the following condition, similar to Eq. (2.33). Namely, in terms of given charges Q_l it sounds:

$$Q_i = \frac{1}{K} \int_0^K \alpha(r) Q_r(r) e^{-jri\Lambda} = Q_l \delta_{il}, \tag{2.38}$$

which yields for the $\alpha(r)$ a similar expression as that given by Eq. (2.34):

$$\alpha(r) = Q_l \frac{e^{jrl\Lambda}}{Q_r(r)}. \tag{2.39}$$

Integrating the weighted spatial spectrum (see Eq. (2.35)) $V(r) = V_r(r)\alpha(r)$, where V_r is defined by Eq. (2.37), from 0 to K with respect to spectral variable r

one readily obtains the following expression for the voltage between neighboring strips V_i resulting from the given charge of the strip centered at $x_l = l\Lambda$:

$$V_i = \frac{jQ_l}{\epsilon K}\int_0^K \frac{P_{-r/K}(-\cos\Delta)}{P_{-r/K}(\cos\Delta)} e^{-jr(i-l+1/2)\Lambda} dr. \tag{2.40}$$

The weighting function $\alpha(r)$ introduced above in Eqs. (2.34) and (2.39), depending on the strips excitation, modifies the spectral representation of the complex field function $\Phi(\xi)$ in the entire domain (see Eq. (2.19)):

$$\begin{gathered}\Phi(\xi) = 2\alpha(r)P_n(\cos\Delta), \\ D(\xi) = \alpha(r)P_n(\cos\Delta),\ E(\xi) = \alpha(r)S_nP_n(\cos\Delta).\end{gathered} \tag{2.41}$$

In the above equation the corresponding functions are defined in subsequent domains of spatial spectrum variable of width K. It is worth noting that in real systems of strips the total charge of all strips vanishes. Since the charge is defined as the integral of $D(x)$ with respect to x in spatial domain:

$$Q(x) = \epsilon\int_{-\infty}^{x} D(x)dx, \tag{2.42}$$

its spectral representation therefore is:

$$Q(\xi) = j\epsilon D(\xi)/\xi. \tag{2.43}$$

The total electric charge in the plane of strips is $Q(\infty)$, and if the limit exists in spectral domain

$$\lim_{\xi\to 0} D(\xi)/\xi = 0, \tag{2.44}$$

then the total charge of the system vanishes. Thus, for real systems $\alpha(0) = 0$, because $P_0(\cos\Delta) = 1$.

2.2.1. Principles of the BIS-expansion method

The essence of the BIS-expansion method which is further used in generalized form for modeling of acoustic beam-forming structures in the Chapter 3 can be distinctly presented following the work of **B**lotekjœr, **I**ngebrigtsen, and **S**keie [34]. To this end, it is assumed here that the dielectric permittivity in the Green's function definition (see Eq. (2.3)) is a function of the spectral variable, tending to certain limit for large value of its argument:

$$\epsilon = \epsilon(\xi),\ \epsilon(\xi\to\infty)\to\epsilon_\infty. \tag{2.45}$$

In electrostatic analysis of the surface acoustic wave interdigital transducers this corresponds to the wavenumber dependent dielectric permittivity, which for many practical cases, considered for example in [34], possess the above property, given by Eq. (2.45). In this Section the notation $D = D_z$ is adopted in Eq. (2.5) (assuming $\epsilon = 1$ for clarity of presentation). To derive the expression for general solution of electrostatic problem for periodic system of strips the partial solution given by Eq. (2.18) is used. Multiplying the equations by the exponential term e^{-jmKx}, where m is arbitrary integer, and taking a linear combination of the resulting terms, one readily obtains:

$$\begin{aligned}
&\sum_{m=-\infty}^{\infty} \alpha_m \sum_{n=-\infty}^{\infty} jS_n P_n(\cos\Delta) e^{-j\xi_n x} = \\
&\qquad \begin{cases} 0, & |x|<d, \\ \dfrac{\sqrt{2}S_x e^{-j(r-K/2)x}}{\sqrt{\cos\Delta - \cos Kx}} \displaystyle\sum_{m=-\infty}^{\infty} \alpha_m e^{-jmKx}, & d<|x|<\dfrac{\Lambda}{2}, \end{cases} \\
&\sum_{m=-\infty}^{\infty} \beta_m \sum_{n=-\infty}^{\infty} P_n(\cos\Delta) e^{-j\xi_n x} = \\
&\qquad \begin{cases} \dfrac{\sqrt{2}e^{-j(r-K/2)x}}{\sqrt{\cos Kx - \cos\Delta}} \displaystyle\sum_{m=-\infty}^{\infty} \beta_m e^{-jmKx}, & |x|<d, \\ 0, & d<|x|<\dfrac{\Lambda}{2}, \end{cases}
\end{aligned} \tag{2.46}$$

where α_m and β_m are certain unknown coefficients. Simple rearrangement of terms (hint: introduce a new summation index $p = m + n$ and retrieve to the previous notation $p \to n$) immediately results in:

$$\sum_{m=-\infty}^{\infty}\sum_{n=-\infty}^{\infty} j\alpha_m S_{n-m} P_{n-m}(\cos\Delta) e^{-j\xi_n x} = \begin{cases} 0, & |x|<d, \\ \dfrac{\sqrt{2}S_x e^{-j(r-K/2)x}}{\sqrt{\cos\Delta-\cos Kx}} \displaystyle\sum_{m=-\infty}^{\infty} \alpha_m e^{-jmKx}, & d<|x|<\dfrac{\Lambda}{2}, \end{cases}$$

$$\sum_{m=-\infty}^{\infty}\sum_{n=-\infty}^{\infty} \beta_m P_{n-m}(\cos\Delta) e^{-j\xi_n x} = \begin{cases} \dfrac{\sqrt{2}e^{-j(r-K/2)x}}{\sqrt{\cos Kx-\cos\Delta}} \displaystyle\sum_{m=-\infty}^{\infty} \beta_m e^{-jmKx}, & |x|<d, \\ 0, & d<|x|<\dfrac{\Lambda}{2}. \end{cases} \tag{2.47}$$

The functions defined by expansions on the left-hand side of Eq. (2.47) are Λ-periodic in x, vanishing in certain domains as required by the boundary conditions for field components on the plane of strips $z = 0$ (see Eq. (2.9)). Moreover, they exhibit square-root singularities at the strips edges, as required by the edge conditions (see Eq. (2.10)). Hence, the functions are well suited for representation of the tangential electric field and normal electric induction in the form of series expansion, as follows:

$$\begin{aligned} E(x) &= \sum_{n=-\infty}^{\infty} E_n e^{-j\xi_n x}, \;\; E_n = \sum_{m=-\infty}^{\infty} j\alpha_m S_{n-m} P_{n-m}(\cos\Delta), \\ D(x) &= \sum_{n=-\infty}^{\infty} D_n e^{-j\xi_n x}, \;\; D_n = \sum_{m=-\infty}^{\infty} \beta_m P_{n-m}(\cos\Delta). \end{aligned} \tag{2.48}$$

The Eqs. (2.48) represent the Fourier series expansions of the electrostatic field components E and D. The corresponding coefficients E_n and D_n are further expanded into the series of properly chosen ('properly' means here that the corresponding functions on the right-hand side in Eqs. (2.18), (2.46) have suitable square-root singularities near the strips edges) Legendre polynomials. Thus, the boundary and edge conditions are satisfied directly by the field components D and E. One only needs to check if the Laplace equation is not violated, that is the relationship described by the Green's function, Eq. (2.3), holds. Apparently, Eq. (2.3) has to be satisfied identically for each component:

$$E_n = G(\xi_n), \;\; D_n = \frac{jS_n}{\epsilon_n} D_n, \;\; \epsilon_n = \epsilon(\xi_n), \tag{2.49}$$

The Eq. (2.49) states the relationship between the modes amplitudes of the electrostatic field components vanishing at infinity (satisfying equivalent 'radiation conditions', see Sec. 2.1.). It has to be obeyed for all n. To obtain a finite series expansion of the mode amplitudes E_n, D_n in Eq. (2.48), the following approximation can be used:

$$\epsilon_n = \epsilon_\infty, \; n \notin [N_{min}, N_{max}], \tag{2.50}$$

where N_{min} and N_{max} are some large but finite integers. Then, substituting Eq. (2.50) into Eq. (2.49) within some finite domain of $m \in [M_{min}, M_{max}]$ one obtains:

$$\begin{aligned} E_n &= \sum_{m=M_{min}}^{M_{max}} j\alpha_m S_{n-m} P_{n-m}(\cos\Delta), \\ E_n &= \frac{jS_n}{\epsilon(\xi_n)} \sum_{m=M_{min}}^{M_{max}} \beta_m P_{n-m}(\cos\Delta), \end{aligned} \tag{2.51}$$

To find the expansion coefficients α_m, β_m for the above finite range of m, it is convenient to apply the approximation given by Eq. (2.50). Hence, the Eqs. (2.51) should be solved for α_m, β_m with $n \in [N_{min}, N_{max}]$ assumed. For $n \notin [N_{min}, N_{max}]$, on the other hand, Eqs. (2.51) must be satisfied identically which is possible only if the following relationships hold [34]:

$$\beta_m = \epsilon_\infty \alpha_m, \;\; S_{n-m} = S_n. \tag{2.52}$$

Taking into account that $S_n = 1$ for $n \geq 0$ and -1 otherwise, and that $r \in (0, K)$ is restricted to the first Brillouin zone in the definition of $\xi_n = r + nK$, the following requirements for the bounds N_{max} and N_{min} result:

$$N_{min} \leq 0, \;\; N_{max} \geq -1. \tag{2.53}$$

Besides, from Eq. (2.52) for $n \notin [N_{min}, N_{max}]$ and $m \in [M_{min}, M_{max}]$ in view of Eq. (2.53) it also follows that:

$$N_{min} - 1 - M_{min} < 0, \;\; N_{max} + 1 - M_{max} \geq 0. \tag{2.54}$$

Substituting Eq. (2.52) into Eq. (2.51) the coefficients β_m can be eliminated, which yields:

$$\sum_{m=M_{min}}^{M_{max}} \alpha_m \left[S_{n-m} - \frac{\epsilon_\infty}{\epsilon_n} S_n \right] P_{n-m}(\cos\Delta) = 0. \tag{2.55}$$

The above system of linear equations is valid for any integer n. Taking into account Eq. (2.52), one can easily observe that Eqs. (2.55) are satisfied identically for $n \notin [N_{min}, N_{max}]$. Accounting for the conditions specified by Eq. (2.54), the following limits M_{min} and M_{max} can be obtained:

$$M_{min} = N_{min}, \quad M_{max} = N_{max} + 1, \tag{2.56}$$

which means that there are $N_{max} - N_{min} + 1$ equations for $N_{max} - N_{min} + 2$ unknown coefficients α_m. To obtain a closed system additional equation is required. To this end, for example, the following one can be used [34]:

$$\sum_{m=M_{min}}^{M_{max}} j\alpha_m S_{-m} P_{-m}(\cos\Delta) = E_0. \tag{2.57}$$

which allows to express all unknown coefficients α_m in terms of E_0 (E_0 assumed given; for instance normalized value $E_0 = 1$ can be applied). Alternatively, one can use the circuit conditions, for example, given potentials of the strips (or charges). The potential $\varphi(x)$ evaluated at the l^{th} strip's center position $x = x_l = l\Lambda$ (note, potentials is constant on strip and for convenience is evaluated at its center) is:

$$\varphi_r(l\Lambda) = -\int E(x)dx|_{x=l\Lambda}, \tag{2.58}$$

where the subscript r indicates dependence of $\varphi(l\Lambda)$ on r - reduced spatial spectrum variable. Substituting expansion given by Eq. (2.48) into Eq. (2.58) one obtains:

$$\varphi_r(l\Lambda) = \sum_m \alpha_m \sum_{n=-\infty}^{\infty} \frac{S_{n-m} P_{n-m}(\cos\Delta)}{r + nK} e^{-jrl\Lambda}, \tag{2.59}$$

where summation over $m \in [N_{min}, N_{max} + 1]$ is assumed. Using the expression of the previous Section given by Eq. (2.28), a sum over n can be transformed as follows (making a simple change of summation index $p \to n - m$):

$$\varphi_r(l\Lambda) = -\frac{\pi}{K \sin \pi r/K} \sum_m (-1)^m \alpha_m P_{-m-r/K}(-\cos\Delta) e^{-jrl\Lambda}. \tag{2.60}$$

The solution, which is sought here, must satisfy the condition that the potentials at different strips takes different (specified) values φ_l, dependent on l. This requires integration of the Eq. (2.60) over $r \in (0, K)$, which is analogous to the

inverse Fourier transform of the discrete function $\varphi_l = \varphi_r(l\Lambda)$ defined by (note that the harmonic term $e^{-jrl\Lambda}$ is already included in the φ_r evaluated above):

$$\frac{1}{K}\int_0^K \varphi_r(l\Lambda)\,dr = \varphi_l. \tag{2.61}$$

This finally yields the last condition for α_m dependent on r (φ_l are given):

$$\sum_m (-1)^m \alpha_m P_{-m-r/K}(-\cos\Delta) = j\frac{K}{\pi}\,\varphi_l\, e^{jrl\Lambda}\sin \pi r/K. \tag{2.62}$$

Simple substitution of Eq. (2.62) into Eq. (2.60) verifies that Eq. (2.61) is satisfied. This is the last equation that must be appended to the system of linear equations given by Eq. (2.55) in order to obtain equal number of equations and unknowns. Now, one can evaluate α_m dependent on given φ_l, and finally, evaluate the electrostatic field components using Eq. (2.48).

2.3. Electrostatics of finite system of strips

For a finite planar system of conducting strips in the frame of the spectral approach, discussed in this Section, a set of the so-called 'template functions' in the spatial spectrum domain is defined. These functions are the partial solutions of the corresponding electrostatic problem. The general solution is obtain by the linear combination of the 'template functions', and unknown coefficients are determined from the supplementary conditions: given strip voltages or charges (or interconnections).

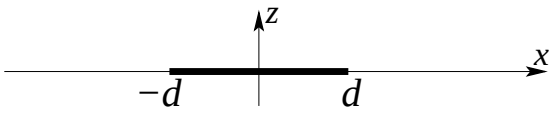

Figure 2.3. A conducting strip of width $2d$ placed on the plane $z = 0$.

It is convenient to start the analysis from considering a single conducting strip, illustrated in Fig. 2.3. To derive the corresponding 'template function' the results obtained in Sec. 2.1. (see Eqs. 2.7 and (2.8)) for a conducting half-plane can be used. Namely, the complex field function in spatial domain for the strip is described by the product of corresponding functions for half-planes as follows [60]:

$$\Phi^{(1)}(x;d) = \Phi^{(0)}(x+d)\Phi^{(0)}(d-x) = \begin{cases} |d^2 - x^2|^{-1/2}, & |x| < d, \\ jS_x|d^2 - x^2|^{-1/2}, & |x| > d. \end{cases} \tag{2.63}$$

Using the convolution theorem, stating that the Fourier transform of a convolution of two functions is the point-wise product of their Fourier transforms, the spectral representation of the complex field function in Eq. (2.63) is:

$$\Phi^{(1)}(\xi;d) = [\Phi^{(0)}(\xi)e^{j\xi d}] * \left[\Phi^{(0)}(\xi)e^{j\xi d}\right]^{*}. \tag{2.64}$$

(the superscript $*$ means the complex conjugation). Taking into account the semi-finite support of the complex field function $\Phi(\xi)$ (see Eq. 2.6), the convolution (2.64) can be written explicitly (hint: change the variable into $y - \xi/2$):

$$\Phi^{(1)}(\xi;d) = \int_0^{\xi} \frac{e^{j(\xi-y)d}e^{-j\pi/4}}{\sqrt{\pi(\xi-y)}} \frac{e^{-jyd}}{\sqrt{\pi y}} e^{j\pi/4} dy = J_0(\xi d), \tag{2.65}$$

where J_0 is the 0^{th} order Bessel function of the first kind. Following the same

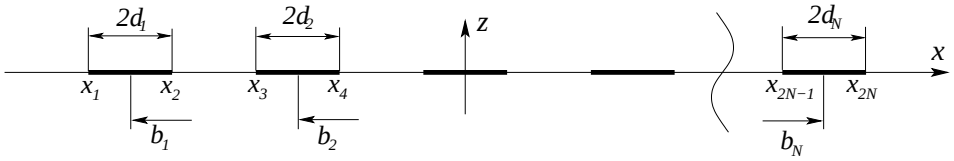

Figure 2.4. System of N conducting strips of different widths $2d_n$ placed on the plane $z = 0$ with displacements b_n with respect to the origin $x = 0$.

considerations, one easily obtains a similar expression as in Eq. (2.63) for the system of two strips (see Fig. 2.4):

$$\Phi^{(2)}(\xi) = [\Phi^{(1)}(\xi;d_1)e^{j\xi b_1}] * [j\Phi^{(1)}(\xi;d_2)e^{j\xi b_2}], \tag{2.66}$$

where $d_{1,2}$ and $b_{1,2}$ are the corresponding widths and displacements of strips having the shifted spatial field representation given by Eq. (2.63). Multiplication by j in the second term in Eq. (2.66) is necessary to obtain $D(x) = \text{Re}\{\Phi(x)\}$ and $E(x) = \text{Im}\{\Phi(x)\}$, conveniently analogous to Eq. (2.7). For three or more strips ($N \geq 3$), one has:

$$\begin{aligned} \Phi^{(N)}(\xi) &= [\Phi^{(N-1)}(\xi)] * \left[j\Phi^{(1)}(\xi;d_N)e^{jrb_N}\right], \\ \Phi^{(N)}(x) &\sim [|(x-x_1)(x-x_2)...(x-x_{2N})|]^{-1/2}, \end{aligned} \tag{2.67}$$

for spectral and spatial representations, respectively, where x_{2i-1}, x_{2i} are the i^{th} strip's edges.

It can be easily checked, that the electrostatic field discussed above vanishes fast with $|x| \to \infty$, indicating the multi-pole character of the charge distribution on the strips. Thus, it cannot form a basis of complete representation of the arbitrary field generated by the system of strips. The system can, for instance, possess a net charge different from zero, inducing the electric field vanishing at infinity like $1/x$. The harmonic function representing such cases and exhibiting square-root singularity at the strip edges is the above derived function $\Phi^{(N)}(x)$ multiplied by a polynomial function of a degree not exceeding $N-1$. Hence, N independent 'template functions' (partial solutions) result, all satisfying the boundary and edge conditions, given by Eqs. (2.9) and (2.10), respectively, and vanishing at infinity (that is, obeying the Eq. (2.4)):

$$\begin{aligned} \Phi^{(N,0)}(x) = \Phi^{(N)}(x),\ \Phi^{(N,1)}(x) &= x\Phi^{(N)}(x),\ \cdots, \\ \Phi^{(N,n)}(x) &= x^n\Phi^{(N)}(x),\ \cdots, \end{aligned} \tag{2.68}$$

which yield the corresponding field components $E^{(n)}$ and $D^{(n)}$ on the plane $z=0$. Applying the known Fourier transform theorem stating that multiplication by x in spatial domain corresponds to differentiation in spectral domain, one formally obtains the above functions in the spectral domain:

$$\begin{aligned} \Phi^{(N,0)}(\xi) = \Phi^{(N)}(\xi),\ \Phi^{(N,1)}(\xi) &= -j\frac{d}{d\,\xi}\Phi^{(N)}(\xi),\ \cdots, \\ \Phi^{(N,n)}(\xi) &= (-j)^n\frac{d^n}{d\,\xi^n}\Phi^{(N)}(\xi),\ n<N, \end{aligned} \tag{2.69}$$

yielding the spectral field representations $E^{(n)}(\xi)$ and $D^{(n)}(\xi)$, according to Eq. (2.11). For the purpose of numerical evaluation it is convenient to redefine the 'template functions' as follows [63]:

$$\begin{aligned} \Phi^{(N,0)}(x) &= j^{N-1}\prod_{i=1}^{N}\Phi^{(1)}(x-b_i,d_i) = \Phi^{(N)}(x), \\ \Phi^{(N,n)}(x) &= \Phi^{(N)}(x)\prod_{i=1}^{n}(x-b_i),\ n=1..N-1, \end{aligned} \tag{2.70}$$

where $b_i = (x_{2i}+x_{2i-1})/2$ is the i^{th} strips center position and $d_i = (x_{2i}-x_{2i-1})/2$ is the i^{th} strips half-width; x_{2i-1}, x_{2i} are the i^{th} strip edges positions (see Fig. 2.4). It is immediately results from the definition of template functions in Eq. (2.70) that they take real values on strips (representing the charge

distribution there), and imaginary values between them (representing electric field there). The subtle difference in definitions of the 'template functions' in Eq. (2.70) and in Eq. (2.68) is the choice of the polynomials: $\prod_{k=1}^{i}(x-b_k)$ instead of x^i. This enables derivation of the analytic expressions for the spatial spectrum representation of the template functions $\Phi^{(N,i)}(\xi),\ i=0,N-1$. To do this, it is convenient to rewrite them in the form of a product of similar terms:

$$\Phi^{(N,i)}(x) = -j \prod_{m=1}^{i} \frac{j(x-b_m)}{\sqrt{d_m^2-(x-b_m)^2}} \prod_{m=i+1}^{N} \frac{j}{\sqrt{d_m^2-(x-b_m)^2}}, \qquad (2.71)$$
$$i=0,\ldots,N-1.$$

The first product in Eq. (2.71) disappears for $i=0$. The spectral representations $\Phi^{(N,i)}(\xi)$ thus immediately results from the convolution theorem:

$$\Phi^{(N,i)}(\xi) = \Phi_1'(\xi) * \cdots * \Phi_i'(\xi) * \Phi_{i+1}(\xi) * \cdots * \Phi_N(\xi), \qquad (2.72)$$

where the corresponding terms are defined as follows ($\mathcal{F}$ denotes the Fourier transform):

$$\Phi_m(\xi)=\mathcal{F}\left\{\frac{1}{\sqrt{d_m^2-(x-b_m)^2}}\right\};\ \Phi_m'(\xi)=\mathcal{F}\left\{\frac{x-b_m}{\sqrt{d_m^2-(x-b_m)^2}}\right\} \qquad (2.73)$$

The Fourier transforms of the functions in Eq. (2.73) can be computed in the closed form. The first term in Eq. (2.73) is essentially the same as in Eq. (2.63) (with the shift in spatial domain defined by b_m). Its Fourier transform can be written in analogous manner as in Eq. (2.65). Making use of the shift theorem, that is, multiplying the spectral counterpart (see Eq. (2.65)) by the exponential term $e^{j\xi b_m}$ one obtains:

$$\Phi_m(\xi) = \begin{cases} J_0(\xi d_m)\, e^{j\xi b_m},\ \xi \geq 0, \\ \\ 0,\ \xi < 0. \end{cases} \qquad (2.74)$$

The generalized transform of the second term in Eq. (2.73) can be done using the differentiation theorem: $\mathcal{F}\{xf(x)\} = -jd\,F(\xi)/d\xi$, yielding:

$$\Phi_m'(\xi) = \begin{cases} -j[\delta(\xi) - \xi_m J_1(\xi d_m)]\, e^{j\xi b_m},\ \xi \geq 0, \\ \\ 0,\ \xi < 0. \end{cases} \qquad (2.75)$$

It is due to the Dirac δ-function in $\Phi_m'(\xi)$ that the evaluation order in Eq. (2.72) is important: the convolutions of functions $\Phi_m(\xi)$ should be evaluated first

(counting from the right to the left) to obtain an integrable product of the regular and δ functions. The algorithm of numerical evaluation of convolutions in Eq. (2.72), thus, would run as follows:

$$\Phi_{N-1} * \Phi_N \Rightarrow \Phi, \cdots, \Phi_{i+1} * \Phi \Rightarrow \Phi, \Phi'_i * \Phi \Rightarrow \Phi, \cdots, \Phi'_1 * \Phi \Rightarrow \Phi^{(N,i)}(\xi).$$

The superposition of these N independent template functions (see Eq. (2.71)) suffices for representation of an arbitrary field that can be generated by the system of N strips subjected to N circuit constraints: given strip voltages or charges, or interconnections. In practical systems usually (e.g. SAW interdigital transducers) both source terminals are connected to different strips, rendering the system electric neutrality (the currents flowing into and out of the system are in perfect balance as flowing through the same source). This means that the electrostatic field excited by the charge distribution on strips is dipole-like, at most, vanishing faster than $1/x$. Consequently, its spatial spectrum must vanish at $\xi = 0$. It is evident that the function $\Phi^{(N,N-1)}(x)$, having the Fourier transform $\Phi^{(N,N-1)}(\xi = 0) \neq 0$, must be excluded from the set of 'template functions' representing the charge distributions on strips because this and only this function represents electric field vanishing like $1/x$ at infinity:

$$\begin{aligned} D^{(N-1)}(\xi) &= \frac{1}{2} \begin{cases} \Phi^{(N,N-1)}(\xi), & \xi \geq 0, \\ \Phi^{(N,N-1)*}(-\xi), & \xi < 0, \end{cases} \\ D^{(N-1)}(x) &= \mathcal{F}^{-1}\{D^{(N-1)}(\xi)\} \sim 1/|x| \text{ at } |x| \to \infty. \end{aligned} \tag{2.76}$$

($\mathcal{F}^{-1}$ means the inverse Fourier transform). The other functions represent field vanishing like $x^{-k}, k = 2, ..., N$, and their spectral representations behave like $\xi^n, n = 1, ..., N-1$ at $\xi \to 0$, according to the limit theorem for the Fourier transforms. The above shows that a linear combination with arbitrary (real valued) coefficients of $N-1$ template functions generates a solution of electrostatic problem for real system of N strips (vanishing net charge):

$$\Phi = \sum_{i=0}^{N-2} \alpha_i \Phi^{(N,i)}, \tag{2.77}$$

To find the coefficients for particular case the circuit equations must be satisfied. Let each strip be connected to either of the source terminals. It is clear that the conditions can be set only on the voltages (potential differences) between strips, not on the potentials of strips itself. There are $N-1$ circuit equations in this case, and one has a complete system of equations for evaluation of all superposition coefficients mentioned earlier. To formulate the equations however,

one needs to evaluate voltages V_i (or, alternatively, charges Q_i) for fields represented by each template function. Without loss of generality, this procedure can be illustrated on the field components $D^{(0)}$ and $E^{(0)}$ evaluated from Eq. (2.11) using $\Phi^{(N,0)}$ in place of Φ: $D^{(0)}(\xi) = \Phi^{(N,0)}(\xi)/2, \xi \geq 0$ or $\Phi^{(N,0)*}(-\xi)/2, \xi < 0$, yielding results marked by the superscript (0). The analysis for the other field components involving the template functions $\Phi^{(N,i)}$, $i = 1..N-2$, is similar. According to the definition of the electric potential $E = -d\varphi/dx$, the strips potentials can be obtained by integration of $E^{(0)}(x)$, what in spectral domain corresponds to the division by ξ of the $E^{(0)}(\xi)$ (with accuracy to an unimportant constant due to the potential difference being only involved in the circuit equations). As concerns the strip's charge $Q^{(0)}(x)$ being the integral of $\Delta D_y = D_y(y+0) - D_y(y-0) = \epsilon D^{(0)}$, using the Green's function defined by Eq. (2.3), one obtains:

$$\begin{aligned} \varphi^{(0)}(x) &= \mathcal{F}^{-1}\{-jE(\xi)/\xi\} = \frac{1}{2\pi}\int_{-\infty}^{\infty} |\xi|^{-1} D^{(0)}(\xi) e^{-j\xi x} d\xi, \\ Q^{(0)}(x) &= \mathcal{F}^{-1}\{j\epsilon D(\xi)/\xi\} = \frac{j\epsilon}{2\pi}\int_{-\infty}^{\infty} \xi^{-1} D^{(0)}(\xi) e^{-j\xi x} d\xi. \end{aligned} \tag{2.78}$$

Naturally, $\varphi(x)$ is constant on the strips because $E(x) = 0$ there, and $Q(x)$ is constant between the strips because $D(x) = 0$ there. Therefore, the voltage V_i between the i^{th} and $(i+1)^{\text{th}}$ strips and the charge Q_i of the i^{th} strip are:

$$\begin{aligned} V_i^{(0)} &= \varphi^{(0)}(\tilde{x}_{i+1}) - \varphi^{(0)}(\tilde{x}_i), \\ Q_i^{(0)} &= [Q^{(0)}(\hat{x}_i) - Q^{(0)}(\hat{x}_{i-1})],\ i = 1, \ldots, N, \end{aligned} \tag{2.79}$$

where $\tilde{x}_i$ is a point within the i^{th} strip domain (for instance - at its center), and $\hat{x}_i$ can be at the center of spacing between two neighboring strips, the $(i+1)^{\text{th}}$ and i^{th}. They can be easily evaluated from the strip edges, except $\hat{x}_0$ and $\hat{x}_N$ the value of which can be applied at certain distances in front of the first strip and after the last one. Both values are equal because $Q^{(N)}(x \to \pm\infty)$ are equal. Note that all the above evaluations involve only the spectral representation of $D^{(0)}(\xi)$.

Applying the same analysis to all field components $D^{(n)}$ and $E^{(n)}$ as above (see Eqs. (2.78) and (2.79)) the following system of linear equations can be deduced:

$$\begin{aligned} &\boldsymbol{A}\boldsymbol{\alpha} = \boldsymbol{V},\ \boldsymbol{V} = [V_i],\ \boldsymbol{A} = [A_{ij}],\ i, j = 1, \ldots, N-1, \\ &A_{ij} = \varphi^{(N,j-1)}(b_{i+1}) - \varphi^{(N,j-1)}(b_i), \end{aligned} \tag{2.80}$$

where the elements of the matrix of the system of linear equations A_{ij} are evaluated using the first equation in Eq. (2.79) by means of Eq. 2.78. Here, the care should be taken to evaluate the spatial spectrum (or equivalently $\Phi^{(N,n)}(\xi)$) with high accuracy. Subsequent application of the FFT (Fast Fourier Transform) in order to evaluate $\varphi^{(N,j)}(x)$ in discrete representation yields the corresponding values of $\varphi^{(N,j)}(\tilde{x}_i)$ - the potential of i^{th} strip (which is taken in the corresponding nearest point to the strip's center from the FFT output series). It should be noted that the matrix elements A_{ij} are evaluated without numerical integration of the square-root singular template functions $\Phi^{(N,n)}(x)$, only their spectral counterparts, evaluated earlier (see Eqs. (2.72), (2.74) and (2.75)) are used. Another, equivalent, formulation of the electrostatic problem can be stated in terms of given charges Q_l. The analysis connected with evaluation of unknown coefficients α_i is similar as in the case of given strip potentials (see Eq. (2.80)).

2.4. Electrostatics of strips - generalization for strips in 'incident' (external) electric field

To illustrate the flexibility of the discussed electrostatic methods based on the spectral theory approach, the problem of planar system of strips in external or, referring to the wave-scattering theory, in the 'incident' spatially variable (harmonic) field is considered as an example in this Section. It is therefore convenient in what follows to adopt the corresponding terminology ('radiation conditions', 'incident' or 'scattered' field and so on). The obtained results will be further exploited in the Chapter 3 where the acoustic wave generation and scattering problem will be considered. In the present analysis not only the strip total charge is evaluated, but also the Bloch harmonics of the 'scattered' field in wide spatial spectrum domain. A periodic system of conducting strips in the 'incident' electric field is considered first. Then, the same problem for a finite system is solved. In this case the method of analysis uses the elements of both the 'template functions' approach, presented in details in the Section 2.3., and the BIS-expansion, discussed in the Section 2.2.1.

2.4.1. Periodic system

Consider the planar periodic system of conducting strips (see Fig. 2.2) in external spatially variable electric field. Without loss of generality the harmonic filed is assumed here. It is convenient to consider the external field on

the plane of strips as an 'incident' wave field in the wave-scattering theory: $(D^I, E^I)e^{-j\xi^I x}$, $\xi^I \neq 0$, where $\xi_I = r + IK$, $r \in (0, K)$, r is again a reduced spectral variable, the 'wave number', from the first Brillouin zone and I is an arbitrary integer. In contrast to the 'scattered' field resulting from the induced strip charges and satisfying the 'radiation condition', that is vanishing at $|z| \to \infty$, the 'incident' field grows there, being a function of the type $e^{|\xi_I z|}$. The components of the 'scattered' field (D^s, E^s) and 'incident' field (D^I, E^I) on the plane of strips obey the conditions given by Eq. (2.3) and Eq. (2.4) respectively. The components of 'incident' field (D^I, E^I) are known and the total electric field is a sum of the 'incident' and 'scattered' fields:

$$(D, E) = (D^I, E^I) + (D^s, E^s). \tag{2.81}$$

Applying a harmonic expansion one obtains:

$$\sum_{n=-\infty}^{\infty} (D_n, E_n)e^{-j\xi_n x} = \sum_{n=-\infty}^{\infty} (D^I, E^I)\delta_{nI}e^{-j\xi_n x} + \sum_{n=-\infty}^{\infty} (D^s_n, E^s_n)e^{-j\xi_n x}. \tag{2.82}$$

The harmonic amplitudes of the total field satisfying the boundary and edge conditions, specified by Eqs. (2.9) and (2.10), respectively, ($E(x)$ vanishes on strips and $D(x)$ vanishes between strips) can be expanded into the series in a similar manner as in the Section 2.2.1. (see Eq. (2.48)):

$$D_n = \sum_{m=-\infty}^{\infty} \alpha_m P_{n-m}(\cos\Delta),\ E_n = j\sum_{m=-\infty}^{\infty} \alpha_m S_{n-m} P_{n-m}(\cos\Delta). \tag{2.83}$$

Substitution of Eq. (2.83) into Eq. (2.82) yields for the n^{th} harmonic field component:

$$\begin{aligned} \sum_{m=-\infty}^{\infty} \alpha_m P_{n-m} &= D^I\delta_{In} + D^s_n, \\ \sum_{m=-\infty}^{\infty} \alpha_m S_{n-m} P_{n-m} &= D^I\delta_{In} + E^s_n, \end{aligned} \tag{2.84}$$

where $E^s_n = jS_n D^s_n$ (vanishing at infinity) and $E^I_n = -jS_n D^I_n$ (growing at infinity), in accordance with Eq. (2.3) and Eq. (2.4), respectively. Taking into account the above relationships and combining both equations in Eq. (2.84) one obtains an infinite system of linear equations for unknown coefficients α_m, as follows:

$$\sum_{m=-\infty}^{\infty} \alpha_m \left(1 - S_n S_{n-m}\right) P_{n-m} = 2D^I\delta_{nI}. \tag{2.85}$$

However, only the finite number of equations are nontrivial, for n in certain domain dependent on I [25]. Particularly, for large $|n| > \max\{|m|, I\}$, the equations are identically satisfied due to $1 - S_{n-m}S_n = 0$ and $\delta_{nI} = 0$ (compare analogous consideration regarding the BIS-expansion method discussed in the Section 2.2.1., Eq. (2.55)). Namely, assume that the 'incident' harmonics field belongs to the domain $I \in [N_{min}, N_{max}]$. Without loss of generality and to simplify notation, one can apply $N_{min} = -N$ and $N_{max} = N$, where N some arbitrary integer. Consequently, it is sufficient to account for $m \in [-N, N+1]$ in Eq. (2.85). For $m \notin [-N, N]$ the equations for α_m are satisfied directly, what can be checked by inspection (note, it must be $N > |I|$). Hence, Eq. (2.85) yields $2N+1$ equations for $2(N+1)$ unknowns α_m. The last equation can be obtained, for example, from the condition of the system electric neutrality (zero net charge). To this end it is convenient to exploit Eqs. (2.42), (2.43) from the Section 2.2. Taking into account Eq. (2.82), the total charge of the considered system in 'incident' electric field can be written as follows:

$$Q(x) = j\epsilon \sum_{n=-\infty}^{\infty} \frac{D_n e^{-j(r+nK)x}}{r+nK};\ Q(\xi) = j\epsilon D_{\lfloor \xi/K \rfloor}/\xi,\ \xi = r + nK, \tag{2.86}$$

where $\lfloor \xi/K \rfloor$ is an integer floor of ξ/K (see Eq. (2.19)). Substituting the expansion of harmonics D_n from Eq. (2.83), the spectral representation of charge distribution results immediately:

$$Q(\xi) = j\epsilon \sum_m \alpha_m P_{\lfloor \xi/K \rfloor - m}(\Delta)/\xi. \tag{2.87}$$

Accounting for the above equation, the condition of the system electric neutrality Eq. (2.43) yields:

$$\sum_m \alpha_m P_{-m}(\Delta) = 0. \tag{2.88}$$

This equation together with Eq. (2.85) form a closed system of linear equations for unknown coefficients α_m in harmonic mode expansion given by Eq. (2.82). Evaluating α_m dependent on given (D^I, E^I), one can finally find the total field at the plane $z = 0$ (and elsewhere in the media). In Fig. 2.5 a computed example is shown for periodic planar system of conducting strips in external 'incident' wave-field.

2.4.2. Finite system

Electrostatic analysis of a finite planar system of strips in external spatially variable (harmonic) electric field can be conducted combining the elements of

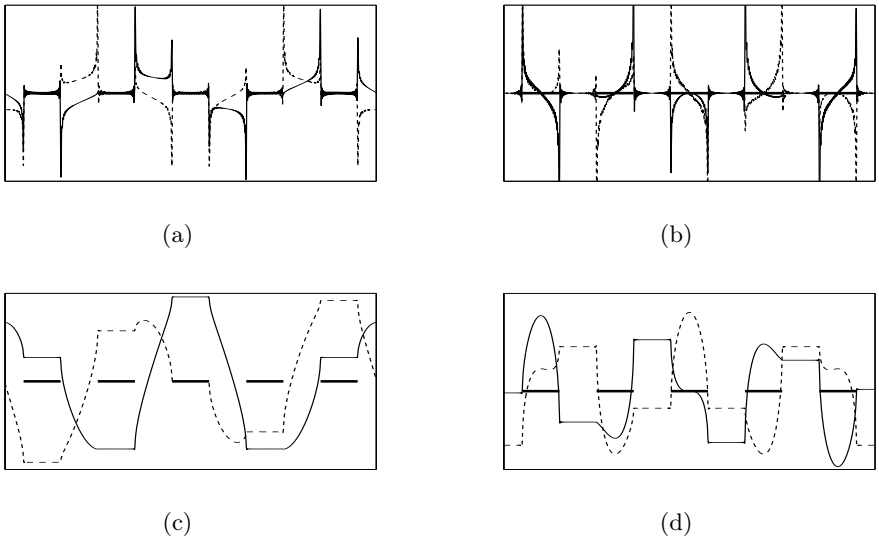

(a) (b)

(c) (d)

Figure 2.5. A Λ-periodic planar system of conducting strips of width $2d = \Lambda/2$ in external electric field: (a) the surface electric field $E_x(x)$, and (b) the normal induction $D_z(x)$. The surface spatial distributions of (c) the electric potential $\varphi(x)$ (note its constant values on strips) and (d) the charge $Q(x)$. Solid and dot lines represent real and imaginary values, respectively. Vertical scales are arbitrary; thick lines in lower figures represent the strips (at the zero level of the corresponding integrals).

both the 'template function' approach and the BIS-expansion method. It is shortly presented in this Section. The main results, obtained here, will be exploited further in the acoustic beam-forming analysis of finite baffle array, discussed in the Section 3.3. The method of analysis benefits of the main features of the approach described in [25] for the case of planar periodic system of groups of strips. Each group is identical and consists of N strips of different width and spacing between them. Such the system is referred to as a multi-periodic one [58]. The template functions defined in [25], due to the system periodicity, are actually the discrete spectral functions represented by certain Fourier series F_n being the convolutions like these given by Eqs.(2.63) and (2.72) but involving Legendre polynomials $P_n(\cdot)$ instead of the Bessel function $J_0(\xi)$ (for the periodic system, considered in the Section 2.2. F_n is simply P_n). On the strength of the asymptotic expansion [64]:

$$P_n(\cos\Delta) = J_0([2n+1]\sin[\Delta/2]) + O(\sin^2[\Delta/2]),\ \Delta \sim Kd \to 0, \qquad (2.89)$$

it can be inferred that the difference between the functions obtained in both cases vanishes if $\xi = nK, K \to 0$. This approximation for K small but finite is exploited here in developing the solution of the finite planar system of strips in external spatial harmonic field, using the earlier evaluated function $D^{(N-1)}(\xi)$ (see Eq.(2.17) in the Section 2.3.) [37], which is denoted here as $\hat{D}(\xi)$ to shorten notation. As it was discussed in the Section 2.3., the template function $\Phi^{(N,N-1)}(\xi)$ which defines the function $\hat{D}(\xi)$, requires only numerical evaluation of multiple convolutions (see Eq. 2.72). This can be done using the convolution theorem as follows:

$$\begin{aligned} &\int_{-\infty}^{\infty} f_1(\xi-\xi')f_2(\xi')d\,\xi' = \mathcal{F}\{f_1(x)f_2(x)\},\ f_i(x) = \mathcal{F}^{-1}\{f_i(\xi)\},\\ &f(x) \approx \kappa \sum_{i=0}^{M-1} f_i\, e^{-jx\xi_i},\ \kappa = \xi_M/M,\ \xi_i = i\kappa;\ f_i = f(\xi_i), \end{aligned} \tag{2.90}$$

where the FFT algorithm is used for numerical evaluation of the Fourier transforms. Its input data is the set of samples of the transformed function evaluated at discrete spectral points $k_i = i\kappa, i = 0 \ldots M-1$, where M is typically a power of 2. Therefore, it is the discrete series in the numerical analysis and it actually represents, on the basis of the theory of FFT [65], the periodic function in spatial domain with a certain large period $2\pi/\kappa$. This justifies approximation of the considered system of strips by certain multi-periodic one and, thus, enables one to introduce the notations:

$$\hat{D}_i = \hat{D}(i\kappa),\ \hat{E}_i = jS_i\hat{D}_i;\ \hat{D}_{-i} = \hat{D}_i^*. \tag{2.91}$$

In the case of multi-periodic system of strips, only one series is evaluated, namely P_n [25]. All the other which correspond to $\Phi^{(N,n)}$ for different $n \in (0, N-1)$, are obtained by shifting the index of P_n to obtain the series P_{n-m}. Moreover, if $m \leq N/2$, the template functions P_{n-m} satisfy the 'radiation conditions' and thus are accounted for in the field representation in order to satisfy the corresponding circuit equations, including electric neutrality of the system. This is because $F_{|k|\leq N/2} = 0$ [58]. In the case of the finite system of strips considered here, the functions $\Phi^{(N,n)}$ have an analogous property that, behaving like ξ^{n-N}, they have small values over a broader domain of $\xi \approx 0$ (see Eq. (2.67) and corresponding discussion in the Section 2.3.) In the following analysis the series $\hat{D}_i$ introduced in Eq. (2.91), with $\hat{D}_0 \neq 0$, play an important role in the solution of the considered problem of strips in external electric field. Note that the pair of functions with shifted indices $\hat{D}_{n-m}$ and $\hat{E}_{n-m}$ places the values $\hat{D}_0, \hat{E}_0$ at the spectral line $k = m\kappa$, what corresponds to multiplication by e^{-jmKx} in the

spatial domain. Naturally, such multiplied functions still satisfy the boundary conditions on the plane of strips ($E(x) = 0$ on the strips and $D(x) = 0$ outside the strips). This property is exploited below with this important remark that D and E evaluated from Eq. (2.11) using the shifted $\hat{D}_{i-m}$

$$D_i = \hat{D}_{i-m} \text{ and } E_i = \hat{E}_{i-m} = jS_{i-m}\hat{D}_{i-m} \tag{2.92}$$

fail to satisfy Eq. (2.3) ($E_i \neq jS_iD_i$, this can be easily verified by inspection), and thus they fail to satisfy the 'radiation condition' (the corresponding field does not vanish at $|z| \to \infty$). This failure, however, takes place only due to the spectral components within domain $0 \leq i \leq m$; all the other ones satisfy well Eq. (2.3).

In a similar way as in the case of periodic strips, the 'incident' field is introduced in the form $(D^I, E^I)e^{-j\xi^I x}$, $\xi^I \neq 0$, where $\xi_I = r + IK,\ r \in (0, K)$. This field is a function of type $e^{|\xi_I z|}$ for at $|z| \to \infty$ and obeys Eq. (2.4); explicitly:

$$E^I = -G(IK)D = -jS_I D^I. \tag{2.93}$$

To simplify the analysis, $I > 0$ is assumed. The field on the strip plane $z = 0$ is the sum of the 'scattered' (marked by the superscript s) and 'incident' spatial waves; it must satisfy the boundary and edge conditions on this plane. Noticing that the field $(\hat{D}_{i-m}, \hat{E}_{i-m})$ does, it is convenient to express the surface field by the combination (the summation convention applied over repeated indices):

$$\begin{aligned} E_i &= E_i^s + E^I\delta_{iI} = j\alpha_m S_{i-m}\hat{D}_{i-m}, \\ D_i &= D_i^s + D^I\delta_{iI} = \alpha_m\hat{D}_{i-m}, \end{aligned} \tag{2.94}$$

where δ is the Kronecker delta and α_m are unknown coefficients. One needs only to add the requirement that the 'scattered' field obeys Eq.(2.3), that is $E_i^s = jS_iD_i^s$; explicitly:

$$\alpha_m(1 - S_iS_{i-m})\hat{D}_{i-m} = 2D^I\delta_{iI}. \tag{2.95}$$

It may be checked by inspection that the solution to this infinite system of equations (for i in infinite domain) can be solved with $\alpha_m, 1 \leq m \leq I + 1$, for the assumed $I > 0$. Indeed, for any $i > I$, the term in brackets turns to zero satisfying the homogeneous equation ($\delta_{I,i>I} = 0$), and similarly for any $i \leq 0$, provided that m takes values in the above limits (compare with the case of periodic strips discussed in the previous Section). For $i = I$ one has $\alpha_{I+1} = 1/\hat{D}_1^*$. Other α_m can be evaluated in recursive manner, starting with

equation $i = I$ down to $i = 1$. The resulting field distribution may include a net charge, $D_0 \neq 0$. To assure the system electric neutrality, one needs to add $\alpha_0 \hat{D}_i$ to the evaluated D_i with coefficient α_0 chosen to obtain:

$$D_0 + \alpha_0 \hat{D}_0 = 0. \tag{2.96}$$

This completes the solution of the problem of planar finite system of strips in external spatial harmonic field; the resulting surface field in the spectral representation is:

$$D_i = \alpha_m \hat{D}_{i-m},\ E_i = j\alpha_m S_{i-m} \hat{D}_{i-m};\ 0 \leq m \leq I+1, \tag{2.97}$$

satisfies the boundary and edge conditions on the plane of strips. In Fig. 2.6 a computed example is presented for the planar system comprising 4 conducting strips of different width and spacing between them.

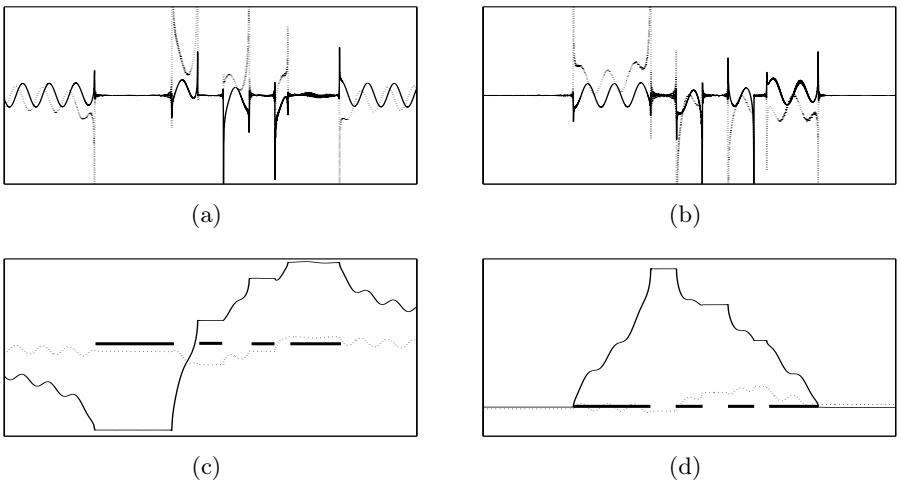

Figure 2.6. A planar finite system comprised of 4 conducting strips in external electric field: (a) the surface electric field $E_x(x)$, and (b) the normal induction $D_z(x)$. The surface spatial distributions of (c) the electric potential $\varphi(x)$ (note its constant values on strips) and (d) the charge $Q(x)$; equal values of $Q(x)$ on both sides of the structure indicates the structure electric neutrality. Solid and dot lines represent real and imaginary values, respectively. Vertical scales are arbitrary; thick lines in lower figures represent the strips (at the zero level of the corresponding integrals).

Moreover, the induced strip voltages and charges can be evaluated in the already presented manner, using Eq. (2.78), in the corresponding discrete form ($\xi = i\kappa$). These should be treated like originating from the negative external

voltage source. If, for example the i^{th} strip is assumed to be grounded but gets certain potential due to the 'incident' field, then a combination of template functions $\Phi^{(N,n)}$ must be added with proper coefficients evaluated in the Section 2.3.

3

Application in acoustic beamforming analysis

The methods developed in electrostatics for direct evaluation of the surface charge spatial spectrum in the case periodic and finite systems of conducting strips, can be successfully generalized for application in the analysis of acoustic beam-forming structures. In particular, in this Chapter the acoustic linear transducer array is considered. Generalization of electrostatic methods for the case of 2D planar transducer arrays will be considered in the Chapter 5.

Typical transducer array is an alternate set of acoustically different materials: piezoelectric, which responds to the incident waves by electric signal, and acoustically isolating material (like epoxy) between them [66, 67]. Piezoelectric materials are closer to hard, and epoxy is closer to soft acoustic materials. Hence, the Bragg scattering occurs when the incident wave illuminates the transducer. The idea of beam-forming is based on excitation of the wave-field by a system of acoustic sources distributed on certain, usually flat surface with their strength chosen such that the radiated wave into the body evolves into the required wave beam-shape. In the case of receiving transducers, the corresponding filtration of spatial signals is adopted by summing up of the transducer element signals with proper weights and phases [11]. In the simplest case the point-like acoustic sources are assumed, which is usually treated in the signal theory frame-work. In further approximation, the point-like sources are replaced by periodic vibrating strips of finite widths - a periodic baffle system [12].

A similar system is considered here, and the interaction between baffles is accounted for in the full-wave analysis of the wave excitation problem by rigorous formulation of the corresponding boundary-value problem. The analyzed structure consists of periodic acoustically hard baffles where the normal acoustic vibration vanishes [23], and between them there are acoustically soft domains where the acoustic pressure is given constant values (or vanishes in the wave-scattering problem) [68]. This is a mixed (Dirichlet-Neuman) boundary-value

problem that is studied here: the given pressure between baffles models the wave-beam generation, and the pressure exerted on the acoustically hard baffles by the incident and scattered waves, in the case of wave-scattering problem, models the response signal from the individual piezoelectric elements of the transducer. A wave-field excitation by a uniform harmonic pressure distribution is not novel and was earlier dealt with for instance in [68] where a model of a narrow strip transducer is presented. The electrostatic methods, presented in the previous Chapter will be generalized accordingly for solving the mixed-boundary problem for periodic and finite baffle systems.

In the next Section the boundary value problem for baffle array is formulated. A brief discussion concerning the surface harmonic impedance of acoustic half-space which is the acoustic counterpart of the planar Green's function introduced in electrostatic method of analysis (see Section 2.1.) is presented first. Then the boundary conditions for acoustic wave generation and scattering problems are stated. In the Section 3.2. a periodic baffle system is analyzed using the generalized BIS-expansion method (see the Section 2.2.1.). The case of wave generation and scattering are considered in the Sections 3.2.1. and 3.2.2., respectively. Finally, in the Section 3.3. a finite baffle system is analyzed using generalized 'template functions' electrostatic method (see Section 2.3.).

3.1. Boundary-value problem formulation

3.1.1. Surface harmonic impedance of an acoustic half-space

The concept of planar harmonic Green's function introduced in the Section 2.1. was of primary importance in developing the method of solution of electrostatic problem for planar system of strips in spatial spectrum domain (spectral theory). For acoustic wave generation and scattering problems by baffle arrays the corresponding counterpart - the surface harmonic impedance of an acoustic half-space, can be introduced . For this purpose consider a two-dimensional acoustic harmonic wave-field $e^{j(\omega t-\xi x-\eta z)}$ independent of y in the acoustic media governed by equations for acoustic potential φ, pressure p and particle velocity $\vec{v}$ (t -time, x, y, z - spatial coordinates oriented as in Fig. 3.1, ω, ξ, η - angular temporal and spatial frequencies):

$$\begin{aligned} \nabla^2\varphi + k^2\varphi = 0, \\ \vec{v} = -\nabla\varphi,\ p = j\omega\rho_a\varphi, \end{aligned} \tag{3.1}$$

where $k = \omega/c$ is the wave-number. Standard notations are applied: c is the sound velocity and ρ_a is mass density of the media. The special attention is paid to the wave-field at the plane $z = 0$ in the framework of the present method of analysis. Assuming known pressure of the form $pe^{-j\xi x}$, where p is its amplitude, the resulting z-component of the particle velocity $v_z|_{z=0+}$ on the upper side of this plane (denoted by v to shorten notations), can be easily evaluated. Thus, neglecting the exponential term $e^{j(\omega t-\xi x)}$ one obtains:

$$\begin{gathered} v = v_z = -\varphi_{,z} = \eta/(\omega\rho_a)p = Gp,\ G(\xi) = \eta/(\omega\rho_a), \\ \eta = \sqrt{k^2 - \xi^2} = -j\sqrt{\xi^2 - k^2}, \end{gathered} \tag{3.2}$$

where G is the surface harmonic admittance of the acoustic half-space; the relationship between φ and p resulting from Eq. (3.1) has been used. Note, that in Eq. (3.2), the value of η is chosen in order to satisfy the radiation condition of the acoustic field at $z \to \infty$. In the presented method of analysis the x-derivative of the pressure $p(x)$ at $z = 0$ will be exploited, which is denoted as $q = p_{,x} = -j\xi p$. Substituting q into Eq. (3.2) one obtains in spectral domain:

$$v = (jG/\xi)p_{,x} = g(\xi)q;\ g(\xi) = \frac{j}{\omega\rho_a}\frac{\eta}{\xi}. \tag{3.3}$$

The function $g(\xi)$ will be used in place of the Eq. (3.1) in all the analysis which follows concerning the pressure and velocity on the plane $z = 0+$. Note that for large values of its argument the following asymptotic equality holds:

$$g(\xi \to \pm\infty) = g_\infty S_\xi, \tag{3.4}$$

where $g_\infty = 1/(\omega\rho_a)$ is the acoustic admittance divided by k, and $S_\nu = 1$ for $\nu \geq 0$ and -1 otherwise, for arbitrary real ν. Inside the media, the acoustic potential φ generated by the given pressure distribution p at $z = 0$ is

$$\varphi(x, z) = -j\frac{p}{\omega\rho_a}e^{-j\xi x - j\eta z}. \tag{3.5}$$

3.1.2. Boundary conditions on the baffle plane

To formulate the boundary conditions on the plane $z = 0$, it is convenient to consider, without loss of generality, a periodic system of the acoustically hard baffles distributed along the x-axis with period Λ on the boundary $z = 0$ of the acoustic medium spanning for $z > 0$, as shown in Fig. 3.1.

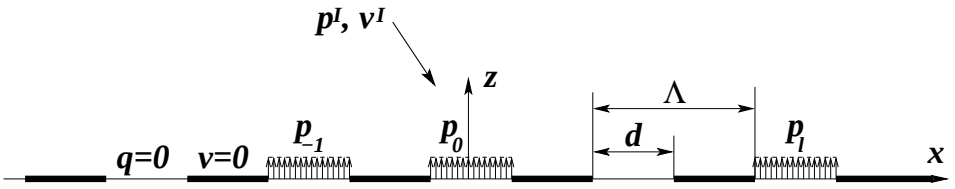

Figure 3.1. Periodic system of baffles: boundary conditions for wave generation problem (note different (arbitrary) pressure in different slots) for which $p^I, v^I = 0$, and for scattering problem, where all $p_l = 0$.

Apparently, a similar boundary conditions on the plane $z = 0$ will also hold in the case of a finite baffle system (see Section 3.3.) Namely, the z-component of the particle velocity on baffles vanishes, and in the slot between baffles, a harmonic pressure of amplitude p_l (constant over an entire slot) excites the wave-field in the medium; $l\Lambda$ describes the position of the given l^{th} slot center along the x-axis:

$$\begin{aligned} q = 0,\ x \in (-d/2, d/2) + l\Lambda \text{ between strips,} \\ v = 0,\ x \notin (-d/2, d/2) + l\Lambda \text{ on strips,} \\ p(l\Lambda) = p_l, \text{ in the middle between strips,} \end{aligned} \tag{3.6}$$

which p_l are given values. They are constant in given slots between baffles due to the condition $q = 0$ there (analogously as the tangential electric field $E_x(x)$ and electric potential $\varphi(x)$ on the plane of conducting strips in the corresponding electrostatic problem, see Section 2.1.). The solutions to the boundary-value problem of interest are the functions $p(x)$ and $v(x)$ at $z = 0$ plane. The field inside the medium, $z > 0$, can be evaluated using Eq. (3.5).

In the case of the wave-scattering problem, the plane incident wave of the form $e^{j(\omega t - \xi_I x + \eta_I z)}$ is assumed, yielding the following wave-field at $z = 0$: $(p^I, v^I)e^{-j\xi_I x}$, where p^I and v^I are the corresponding pressure and velocity (z-component) amplitudes, respectively. It is convenient for the further analysis to rewrite the wave-number component ξ_I as follows: $\xi_I = r + IK$, where $K = 2\pi/\Lambda$ is spatial wave-number of the baffle array, and $r \in (0, K)$ is the reduced wave-number from the first Brillouin zone, I is the corresponding integer. This yields at $z = 0$: $v^I(r)e^{-j(r+IK)x}$, $p^I(r)e^{-j(r+IK)x}$ (compare with electrostatic case discussed in the Section 2.4.). The relationship between p^I and v^I involves the harmonic admittance $-G$, Eq. (3.2), because the incident wave, although propagating in the upper half-space of the medium, satisfies the

radiation condition at $z \to -\infty$:

$$v^I = -G(r+IK)p^I,\ v^I = -g(r+IK)q^I,\ q^I = -j(r+IK)p^I. \tag{3.7}$$

In the case of any non-planar incident wave, its spatial Fourier expansion on the plane $z = 0$ should be applied instead, resulting in certain function $v^I(r)$; the whole domain of $r \in (0, K)$, as well as numerous values of I must be included in the analysis of such non-plane incident wave. In the analysis presented here however, and for the sake of presentation simplicity, the plane incident wave is considered, where r depends on the angle of incidence.

The boundary conditions for full acoustic wave-field are the same as in the previous case, Eq. (3.6), except that $p_l = 0$ should be applied (see Fig. 3.1). The total force exerted on a baffle by the incident and scattered waves models the response of the piezoelectric element of the transducer to the incident acoustic wave.

3.2. Periodic baffle system

Consider a periodic baffle system shown in Fig. 3.1. The BIS-expansion method discussed in the Sections 2.2. and 2.4. will be generalized and applied for analysis of the acoustic wave generation and scattering problems. In Λ-periodic baffle system, $\Lambda = 2\pi/K$ and K being the spatial wave-number of the array (see Fig. 3.1), the wave-field can be represented by the Bloch series like:

$$p(x) = \sum_{n=-\infty}^{\infty} p_n e^{-j(r+nK)x},\ v(x) = \sum_{n=-\infty}^{\infty} v_n e^{-j(r+nK)x}, \tag{3.8}$$

where $\xi_n = r + nK$ is the wave-number of n^{th} spatial harmonic (for convenience, a similar notation as in the Section 2.2.1. is adopted here); $r \in (0, K)$ is an arbitrary spatial wave-number constrained to one Brillouin zone (for uniqueness of the representation, see Section 2.2. and particularly Section 2.2.1.). The Bloch components p_n, v_n are expanded again (the BIS expansion) into the finite series of Legendre polynomials $P_k(\cdot) = P_k^{(0)}(\cdot)$, which expansion, possessing crucial property for the considered boundary-value problem (see Eqs. (2.15) and (2.17) in the Section 2.2.):

$$\begin{aligned} &\sum_{n=-\infty}^{\infty} S_n P_n(\cos\Delta) e^{-jnKx} = 0 \text{ for } |x| < d/2, \\ &\sum_{n=-\infty}^{\infty} P_n(\cos\Delta) e^{-jnKx} = 0 \text{ for } |x| > d/2, \end{aligned} \tag{3.9}$$

where $\Delta = \pi d/\Lambda$, which will be exploited in order to satisfy the boundary conditions on the plane of baffles. For $(\Lambda - d)$-wide strips centered at $x = l\Lambda + \Lambda/2$, the corresponding field expansions at $z = 0$ applied in the solution to the boundary-value both in wave generation and scattering cases problems formulated in the previous Section, Eq. (3.6) (compare with Eq. (2.48) in the Section 2.2.1.) are:

$$\begin{aligned} q &= \sum_{n=-\infty}^{\infty} q_n e^{-j\xi_n x},\ q_n = \sum_m \alpha_m S_{n-m} P_{n-m}(\cos\Delta), \\ v &= \sum_{n=-\infty}^{\infty} v_n e^{-j\xi_n x},\ v_n = \sum_m \beta_m P_{n-m}(\cos\Delta), \end{aligned} \tag{3.10}$$

Note, the summation over m in Eq. (3.10) can be done within some finite domain (see Section 2.2.1.), as is discussed further. The boundary conditions given by Eq. (3.6) are fulfilled directly on the strength of Eqs. (3.9). Now, it should be verified if the applied wave-field solutions satisfy the wave equation inside the media, which equation is represented at the plane $z = 0$ by the harmonic admittance $G(\xi)$, or more convenient, by its version $g(\xi)$, given by Eq. (3.3). Only the spatial harmonics (q_n, v_n) representing the wave-field (q, v) in Eq. (3.10) which satisfy the radiation condition at $z \to \infty$ are involved in Eq. (3.3). Therefore, the incident wave-field, which grows at $\to \infty$ and satisfies Eq. (3.7), must be excluded from the field expansion at $z = 0$. This yields the relation for the n^{th} Bloch component having the wave-number $\xi_n = r + nK$ (δ_{ij} is the Kronecker delta):

$$(v_n - v^I\delta_{nI}) = g(r + nK)(q_n - q^I\delta_{nI}),\ r \in (0, K), \tag{3.11}$$

which must be satisfied for all n. Particularly, for large $|n| \gg |I|$ where

$$g(r \pm NK) = \pm g_\infty. \tag{3.12}$$

Formally, $N \to \infty$, but in the applied approximation, N is assumed large but finite integer - similarly as in the case of electrostatic problem discussed in details in the Section 2.2.1. As it was shown earlier (see Sec. 2.2.1.) this is possible only if (compare with Eq. (2.52)):

$$\beta_m = g_\infty \alpha_m, \tag{3.13}$$

which substituted into Eq. (3.11) and accounting for the last of Eqs. (3.7) yields the following system of linear equations for unknown α_m:

$$\sum_m \alpha_m [g(r + nK)S_{n-m} - g_\infty] P_{n-m}(\cos\Delta) = 2g(r + nK)q^I\delta_{nI}. \tag{3.14}$$

Under condition given by Eq. (3.12), the equations for α_m outside the limits $n \in [-N, N]$ and $m \in [-N, N+1]$ (moreover it must be $N > |I|$) are satisfied directly, what can be checked by inspection (see discussion in the Section 2.2.1., Eqs. (2.52) through (2.57): here $N_{min} = -N$ and $N_{max} = N$). Therefore, Eq. (3.14) yields the system of $2N+1$ equations for $2N+2$ unknowns, which, appended by the equation resulting from the last boundary condition in Eqs. (3.6), can be easily solved. This last equation can be evaluated by integration of $q = p_{,x}$, Eq. (3.10), using the Dougall identity (see Eq. (2.26) and derivation of Eqs. (2.30), (2.32) in the Section 2.2.):

$$P_{-\nu}(-\cos\Delta) = -\frac{\sin\nu\pi}{\pi}\sum_{n=-\infty}^{\infty}, \frac{S_n P_n(\cos\Delta)}{\nu - n} \tag{3.15}$$

yielding (see derivation of Eq. (2.30) in the Section 2.2.):

$$\begin{aligned} p_r(l\Lambda) = j\sum_n \frac{q_n e^{-jrl\Lambda}}{r+nK} = \\ -j\sum_m \frac{\pi(-1)^m \alpha_m e^{-jrl\Lambda}}{K\sin\pi r/K} P_{-r/K-m}(-\cos\Delta), \end{aligned} \tag{3.16}$$

which, being constant between neighboring baffles, is evaluated at $x = l\Lambda$. Note the dependence on spatial spectrum variable is indicated by the subscript r. The solution that is sought, must satisfy certain constraints. Namely, the pressure distribution at the $z = 0$ plane at different slots between baffles takes different (given) values p_l, dependent on l. This requires integration of Eq. (3.16) over $r \in (0, K)$, which is the inverse Fourier transform of the discrete function $p_l = p_r(l\Lambda)$ defined by (note that the harmonic term $e^{-jrl\Lambda}$ is already included in the p_r evaluated above):

$$\frac{1}{K}\int_0^K p_r(l\Lambda)\, dr = p_l. \tag{3.17}$$

This finally yields the last condition for α_m dependent on r (p_l are given):

$$\sum_m (-1)^m \alpha_m P_{-r/K-m}(-\cos\Delta) = j\frac{K}{\pi}\, p_l\, e^{jrl\Lambda}\sin\pi r/K. \tag{3.18}$$

Direct substitution of Eq. (3.18) into Eq. (3.16) verifies that Eq. (3.17) is satisfied. This is the last equation that must be appended to the system given by

Eq. (3.14) in order to obtain a closed system for determining the unknown coefficients α_m. Solving it (numerically) for the unknown coefficients α_m dependent on given p^I (wave scattering) or p_l (wave generation) the wave-field at $z = 0$ and elsewhere in the media $z > 0$, can be found using the expansions given by Eqs. (3.10) and (3.5), respectively.

The main advantage of the the presented method over other methods applied in scattering theory for similar problems is that the boundary conditions are satisfied directly by the proposed solution, Eqs. (3.10). However, certain departure is assumed regarding the equation of motion which is represented here by the harmonic admittance $G(\xi)$ or $g(\xi)$, Eqs. (3.2), (3.3). This departure relies on the approximation that $g(r + nK) \equiv g_\infty$ for $r + nK$ greater that certain large but finite value (far above the domain of existence of propagating modes in the media). In fact, $g(\xi) \to g_\infty$ like $1/\xi^2$ and indeed this approximation can be applied in general in the considered boundary value problem. For instance, considering the finite spatial spectrum domain bounded by certain upper frequency ξ_u, where $\xi_u \approx (5 \div 10)k$ yields approximately $(2 \div 0.5)\%$ difference between $g(\xi_u)$ and g_∞, which accuracy is often acceptable in practical applications. In the consequence of it, the wave-field on the baffle plane is represented by a finite Fourier series multiplied by the square-root singular function at the baffle edges [34]. Accounting for more spatial harmonics in Eq. (3.10), that is applying the larger value of N in Eq. (3.12), the finer approximation is achieved. Actually, for $K \approx k$, N can be chosen quite small ($N \sim 10$).

3.2.1. Wave generation by periodic baffle system

The method of analysis presented here yields the spatial spectrum of the acoustic pressure at the baffle plane, in contrast to the earlier developed methods discussed in the literature [68–70]. To illustrate the advantages of the spectral approach the acoustic wave generation by given constant pressures in the slots between baffles, in accordance with the boundary conditions given by Eq. (3.6), is considered first. As shown above, the solution in this case is given by Eqs. (3.8), (3.10) and the corresponding coefficients α_m result from the system of linear equations, Eqs. (3.14), (3.18) (β_m in Eq. (3.10) can be computed using Eq. (3.13)). More specifically, in this Section evaluation of the far-field radiation pattern for given aperiodic excitation of the baffle array is illustrated. Taking the advantage of the known spatial spectrum of the pressure field distribution on the baffle plane, the radiation pattern can be simply evaluated from the inverse Fourier transform of $p(\xi)$, dependent on the wave-number $\xi = r + nK$ (as was already defined in Eq. (3.17)). The unified representation $p(\xi)$ includes all

Bloch orders and can be defined in the following manner:

$$p(\xi) = \frac{q_n(\xi - nK)}{-j\xi},\ n = \lfloor \xi \rfloor, \tag{3.19}$$

where n is the integer floor of ξ. At the axial distance z above the baffle plane $z = 0$, the acoustic pressure behaves according to Eq. (3.5), thus introducing spatial angular variables: $x = R\sin\theta, z = R\cos\theta$, the pressure dependent on θ at certain fixed spatial distance R is:

$$p_R(\theta) = \int_{-\infty}^{\infty} p(\xi) e^{-jR\xi\sin\theta} e^{-jR\eta\cos\theta} d\xi/K, \tag{3.20}$$

where η is given by Eq. (3.2). At large distance $R \to \infty$, the part of the integral representing the localized field at the baffle plane, which depends on imaginary valued η (see Eq. (3.2)) can be ignored. This is made by constraining ϑ to the domain $(-\pi/2, \pi/2)$ in the transformed integration where $\xi = k\sin\vartheta, \eta = k\cos\vartheta$:

$$p_R(\theta) = \int_{-\pi/2}^{\pi/2} (k/K) p(k\sin\vartheta)\cos\vartheta e^{-jkR\cos(\vartheta-\theta)}\, d\vartheta. \tag{3.21}$$

The integration in Eq. (3.21) can be easily done using the stationary phase method [71, 72] (the stationary point of interest here is $\theta = \vartheta$):

$$p_R(\theta) = p(k\sin\theta)\cos\theta \frac{k}{K}\sqrt{\frac{j2\pi}{kR}}\, e^{-jRk}. \tag{3.22}$$

This is an alternative method of evaluation of the angular radiation characteristics to the one presented in [68–70]. It can be however, evaluated in more efficient method explained below. Solving the system of equations defined by Eqs. (3.14), (3.18), the n^{th} Bloch order of the acoustic pressure $p_n = jq_n/(r+nK)$ is obtained for given r (see Eq. (3.10)). This is the pressure wave-field radiated into the half-space $z > 0$ in the direction described by the corresponding wave-numbers $(\xi_n = r + nK, \eta_n = \sqrt{k^2 - (r+nK)^2})$ provided that η_n is real. Therefore, only limited number of spatial harmonics p_n contribute to the angular radiation pattern at $\theta = \text{atan}(\xi_n/\eta_n)$ (there are multiple directions for small K). Repeating this for all allowed $r \in (0, K)$ in Eq. (3.8) (followed by evaluation of α_m from Eqs. (3.14) and (3.18) and q_n from Eq. (3.10) in the manner presented above), the angular radiation pattern can be fully reconstructed.

The angular radiation pattern concerns the acoustic amplitude a which is related to the acoustic power by $\Pi = |a|^2/2$. It is more convenient to evaluate

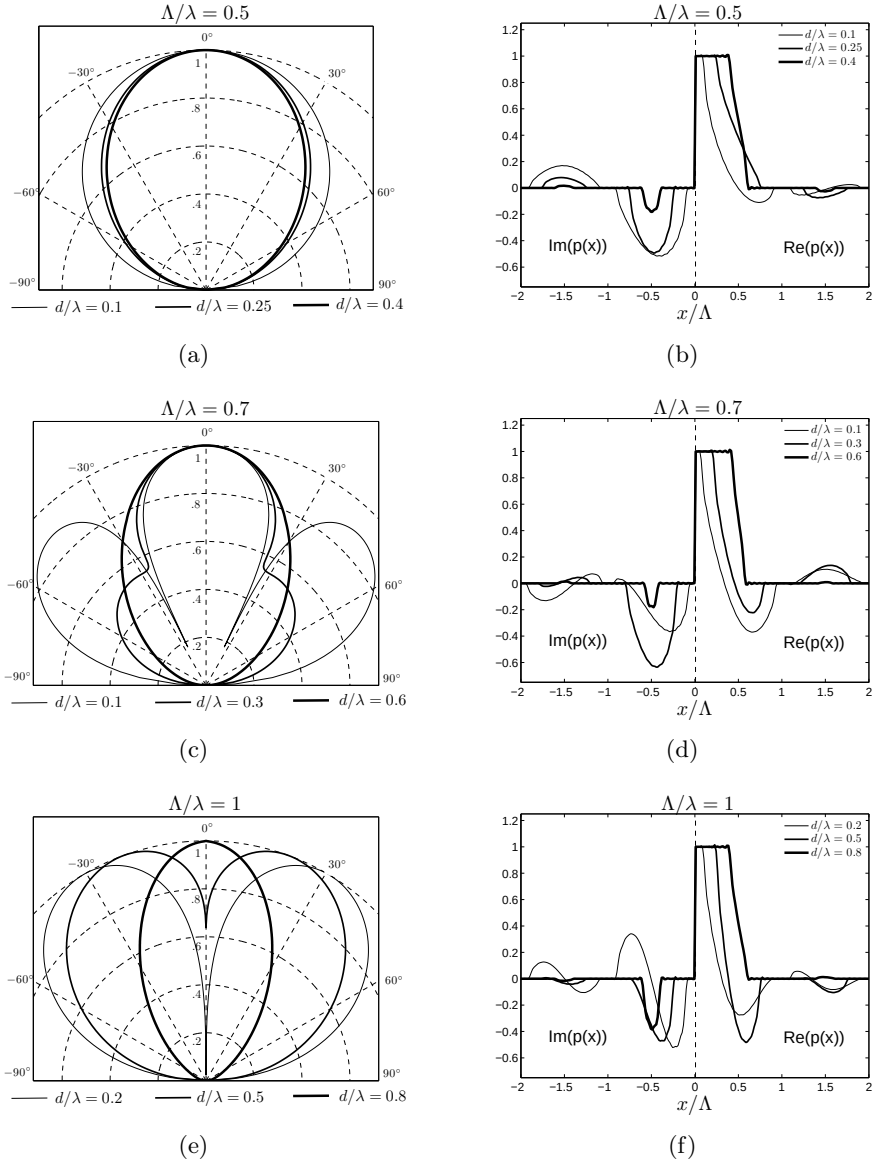

Figure 3.2. Radiation pattern $|p_R(\theta)|$ and pressure distribution on the baffle plane $p(x)$ for different Λ/λ and for slots of different width d.

first the normal component of the acoustic Poynting vector Π_z using the solutions for the acoustic pressure p and normal velocity v on the baffle plane $z = 0$.

For given r and Bloch order n for which η is real, it can be written as:

$$\Pi_z^{(n)} = \mathrm{Re}\{v_n p_n^*\}/2,\ \Pi_z = \sum_n \Pi_z^{(n)}, \tag{3.23}$$

where Π_z is the total power radiated from the baffle plane into the half-space $z > 0$. Having $\Pi_z^{(n)}$, it is easy to guess the absolute value of the Poynting vector $\Pi^{(n)}$ for given Bloch order by taking into account the wave propagation direction described by its wave-vector (ξ_n, η_n):

$$\Pi^{(n)} = \frac{k}{\eta_n}\Pi_z^{(n)},\ a(\theta_n) = \sqrt{2\Pi^{(n)}}, \tag{3.24}$$

where $\eta_n = \sqrt{k^2 - \xi_n^2}$ and $\theta_n = \mathrm{acos}((\eta_n/k)$. The radiation pattern $a(\theta)$ evaluated this way exploits the results already obtained in evaluation of the acoustic field at the baffle plane. Taking into account that $v = 0$ outside the domain of given constant pressure $p_l = p_0$ (the current discussion concerns the particular case when the given pressure takes non-zero value in a single slot, $l = 0$, as in the computed examples shown in Fig. 3.2. The generalization is straightforward), the delivered power is:

$$P = \mathrm{Re}\{vp^*\}/2 = \mathrm{Re}\int_{-w/2}^{w/2} p_l^* v(x)dx/2 \Rightarrow p_l^* \int_{-\Lambda/2}^{\Lambda/2} v(x)dx/2, \tag{3.25}$$

$w = \Lambda - d$ being baffle width. The last integral can be evaluated using the Dougall identity (see Eq. (2.26) and derivation of Eqs. (2.28), (2.31) in the Section 2.2.):

$$\frac{1}{2}\int_{-\Lambda/2}^{\Lambda/2} v(x)dx = g_\infty \frac{\pi}{K}\sum_m \alpha_m P_{-m-r/K}(-\cos\Delta). \tag{3.26}$$

Direct computations show that the evaluated delivered (P) and outgoing (Π_z) acoustic powers agree well in numerical analysis (up to ten digits in double-precision arithmetics (see also discussion in Conclusion); similar accuracy takes place in the scattering problem discussed further below).

In the computed numerical examples presented in Fig. 3.2 both the pressure on the baffle plane $p(x)$ and the radiation pattern $p(\theta)$ are presented, evaluated for several values of slot width d and for three different baffle periods: $\Lambda/\lambda = \{0.5, 0.7, 1.0\}$. For convenience, the real and imaginary parts of the pressure distribution in Figs. 3.2(b), 3.2(d) and 3.2(f) are shown for positive and negative values of x-coordinate respectively, since in the above examples the odd

number of active slots is considered, resulting in the symmetry of the graph of $p(x)$ with respect to the origin. The number of Bloch orders $N = 16$, accounted for in the solution (see Eq. (3.12)), was applied in all numerical examples concerning the periodic baffle system (the examples shown in this and in the next Section). Note that the pressure built-up on baffles can significantly modify the radiation pattern and it is even able to suppress the radiation in certain directions. In the above examples the given pressure takes non-zero value in one slot only: $p_l = \delta_{l0}$. This is further illustrated in Fig. 3.3, where the 2D view of the generated acoustic wave-field in the media above the baffle plane $z > 0$ is shown for chosen values of Λ/λ and d/λ. It is seen, that for $\Lambda/\lambda = 0.7$, $d/\lambda = 0.1$ in Fig. 3.3(b) and $\Lambda = \lambda$, $d/\lambda = \{0.2, 0.5\}$ in Figs. 3.3(c), 3.3(d) (corresponding to the examples of the radiation pattern shown in Fig. 3.2(c) and 3.2(e), respectively) the generated wave-field due to the pressure distribution on the plane $z = 0$ (see Figs. 3.2(b), 3.2(d) and 3.2(f)) for certain values of θ ($\approx 30^\circ$ for $\Lambda/\lambda = 0.7$ and 0° for $\Lambda = \lambda$) adds up destructively, yielding suppression of acoustic wave in these directions.

To illustrate the influence of the inter-element interaction in the periodic baffle system for non-periodic excitation, in the example shown in Fig. 3.4 the comparison of the far-field radiation pattern $p_R(\theta)$ computed for one active slot by the present method and using analytic expression [68]:

$$f(\theta) = \frac{\sin(\pi d/\lambda \sin\theta)}{\pi d/\lambda \sin\theta} \cos\theta, \tag{3.27}$$

is given. In Eq. (3.27) $f(\theta)$ is an angular directivity function of a strip transducer considered with time harmonic uniform pressure distribution along its width (it is in agreement with the results of the experimental studies of [68] and obey Rayleigh-Sommerfeld formula [73]).

An example of wave-beam steering by the baffle system is shown in Fig. 3.5. The radiation pattern is computed for the case of 15 active slots excited with the chosen phase shift $p_l = e^{jkl\Lambda \sin\vartheta}$, for $l = -7, ..., 7$ and $p_l = 0$ otherwise. The steering angle was chosen $\vartheta = 30^\circ$ and 0° for comparison. In Fig. 3.5(a) the case of $\Lambda/\lambda = 0.5$, $d/\Lambda = 0.5$ ($d/\lambda = 0.25$) is illustrated, whereas Fig. 3.5(c) corresponds to $\Lambda/\lambda = 0.7$ and $d/\Lambda = 0.8$ ($d/\lambda = 0.56$). As can be seen in Fig. 3.5(c) for $\Lambda/\lambda = 0.7$ and $d/\Lambda = 0.8$ the grating lobe appears for steering angle $\vartheta = 30^\circ$. This is due to violation of the spatial sampling theorem ($\Lambda \geq \lambda/2$).

In Figs. 3.5(b) and 3.5(d) the corresponding spatial distributions of the pressure $p(x)$ on the baffle plane are shown. And in Fig. 3.6 the 2D pressure field

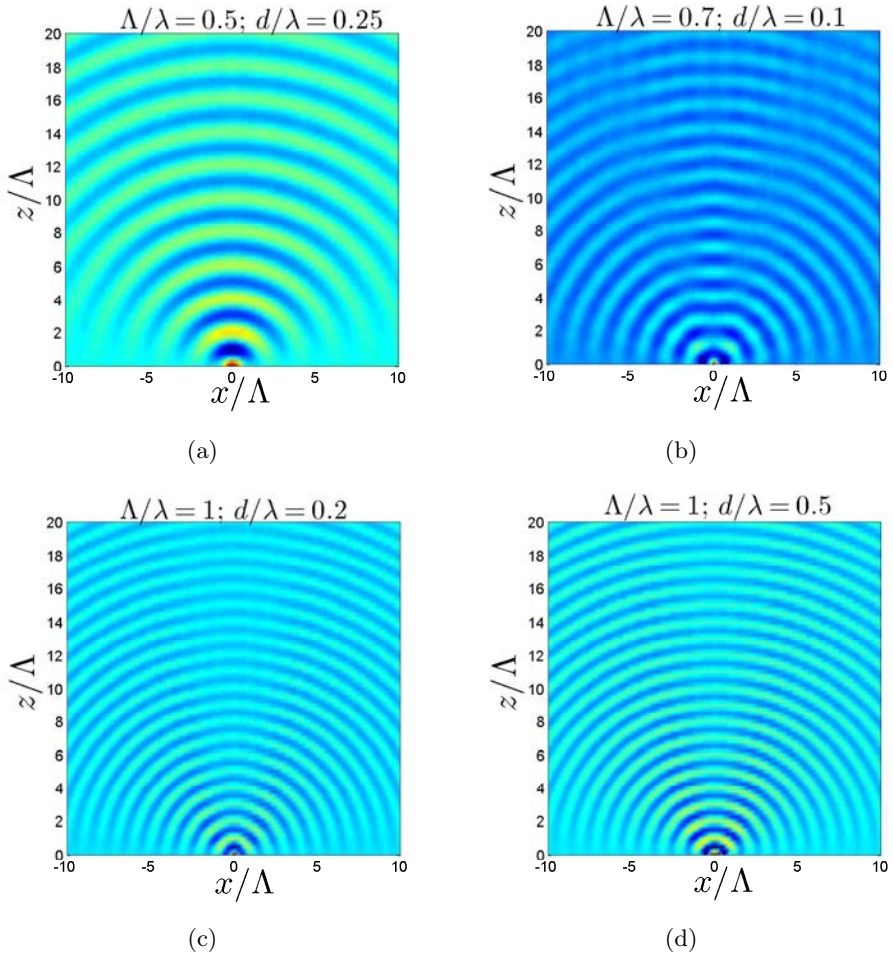

Figure 3.3. 2D view of the generated pressure wave-field in the medium above baffle plane $z > 0$ for different values of Λ/λ and d/λ.

distribution in the media $z > 0$ is shown for the considered system of 15 active slots and steering angles $\{0°, 30°\}$. The same system parameters were assumed: $\Lambda/\lambda = 0.5$, $d/\Lambda = 0.5$ (Figs. 3.6(a), 3.6(b)) and $\Lambda/\lambda = 0.7$, $d/\Lambda = 0.8$ (Figs. 3.6(c), 3.6(d)). Note in Fig. 3.6(c) the appearance of the wave-beam generation in the direction associated with the grating lobe (see Fig. 3.5(c)).

In the above examples the beam-steering is achieved by applying a linear phase shift for the excitation signals of active slots. Similarly, applying a quadratic phase shift [74] a beam-focusing capabilities can be accomplished as

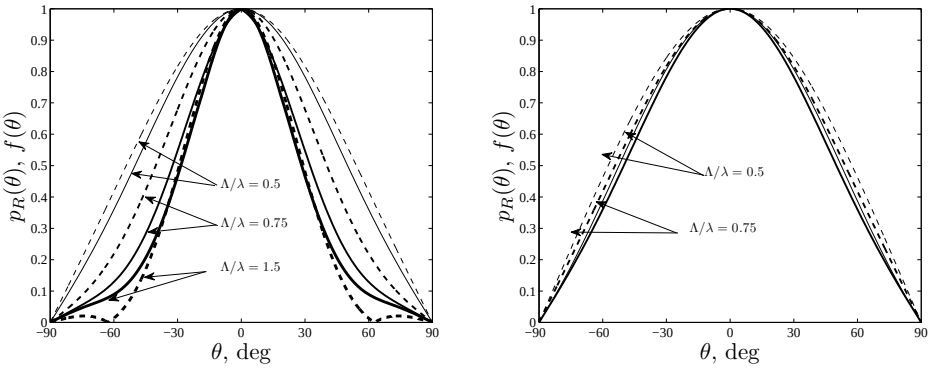

Figure 3.4. Comparison of the radiation pattern $p_R(\theta)$ computed by the present method (solid line) and by the method described in [68] (see Eq. (3) of the cited work): (a) for $d/\Lambda = 0.75$ and different values of Λ/λ, (b) for $\Lambda/\lambda = 0.5$ and different values of d/Λ.

well. In Fig. 3.7 the computed examples of 2D pressure field distribution in the media $z > 0$ is shown for the case of 15 active slots excited with the chosen quadratic phase shift $p_l = e^{jk(l\Lambda)^2\beta}$, for $l = -7, ..., 7$ and $p_l = 0$ otherwise; $\beta = 1/2F$ and $z = F$ - is the focal plane. The same values of $\Lambda/\lambda = 0.5$, $d/\Lambda = 0.5$ (Figs. 3.7(a), 3.7(b)) and $\Lambda/\lambda = 0.7$, $d/\Lambda = 0.8$ (Figs. 3.7(c), 3.7(d)) as in the beam-steering examples are considered here. The focusing at the two axial distance from the origin $F = 10\Lambda$ and $F = 20\Lambda$ were simulated.

Combining both the linear and quadratic phase shifts of the excitation signals applied to active slots in the baffle array, the beam-focusing and beam-steering can be achieved simultaneously. This is illustrated in Fig. 3.8 where the 2D pressure field distribution in the media $z > 0$ is shown for the same 15 active slots and parameters Λ/λ, d/Λ as in the above examples of beam-steering and beam-focusing (see Figs. 3.6, 3.7). Here the focused beam at the distances $F = 10\Lambda$ and $F = 20\Lambda$ is additionally steered at the angle $\vartheta = 30^\circ$ by applying the linear and quadratic phase shifts as in the examples shown in Figs. 3.6 and Figs. 3.7, respectively.

3.2.2. Plane wave scattering

The solution for the plane acoustic wave scattering problem obtained in the framework of the spectral theory presented in the Section 3.1. (see Eqs. (3.14), (3.18)) are exploited here to illustrate the receiver beam-forming capabilities

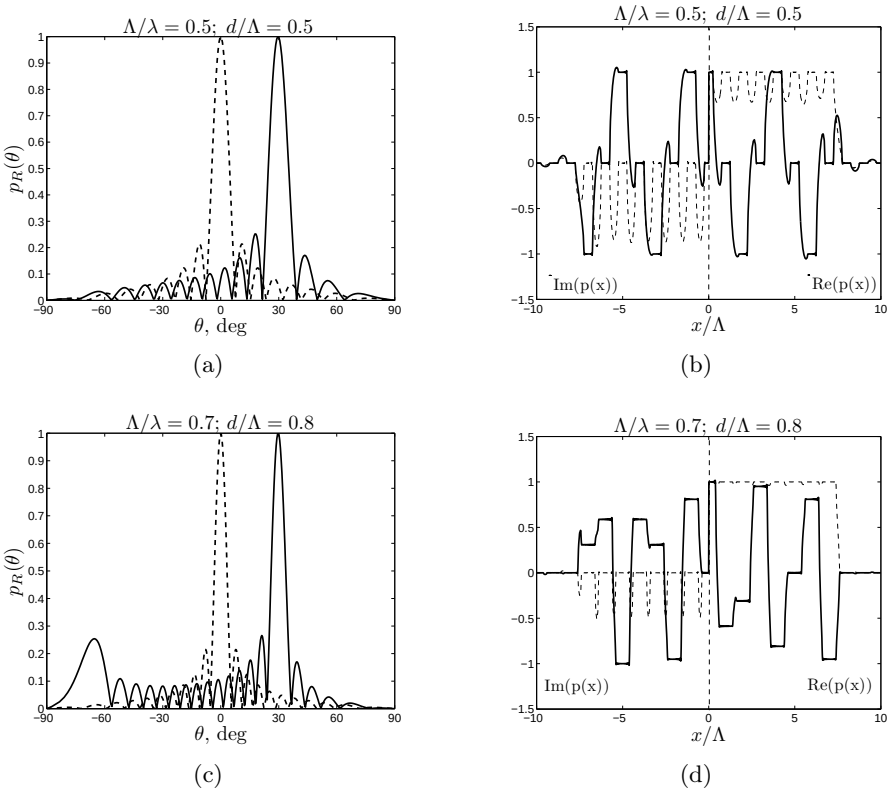

Figure 3.5. Radiation pattern $p(\theta)$ for (a) $\Lambda/\lambda = 0.5$, $d/\Lambda = 0.5$, (c) - $\Lambda/\lambda = 0.7$, $d/\Lambda = 0.8$ and 15 active slots excited with linear phase shift and steering angle $\vartheta = 30^\circ$ (solid line) and 0° (dashed line); (b), (d) - corresponding pressure filed distribution on baffles.

of the considered baffle array. The total force, exerted by the acoustic wavefield (incident and scattered waves) can be evaluated integrating the pressure distribution over the baffle width, given by Eq. (3.8):

$$\bar{p} = \int_{d/2}^{\Lambda - d/2} p(x)dx = \int_0^{\Lambda} \sum_n p_n e^{-jr_n x} dx, \tag{3.28}$$

where $p_n = \int q_n dx$ can be obtained from Eq. (3.10). In Eq. (3.28) the limits of integration can be extended to entire baffle period since $p(x) = 0$ between baffles is assumed. Evaluating the integral term by term, one obtains:

$$\bar{p} = 2j \sin(r\Lambda/2) e^{-jr\Lambda/2} \sum_m \alpha_m \sum_n \frac{S_{n-m} P_{n-m}}{(r + nK)^2}, \tag{3.29}$$

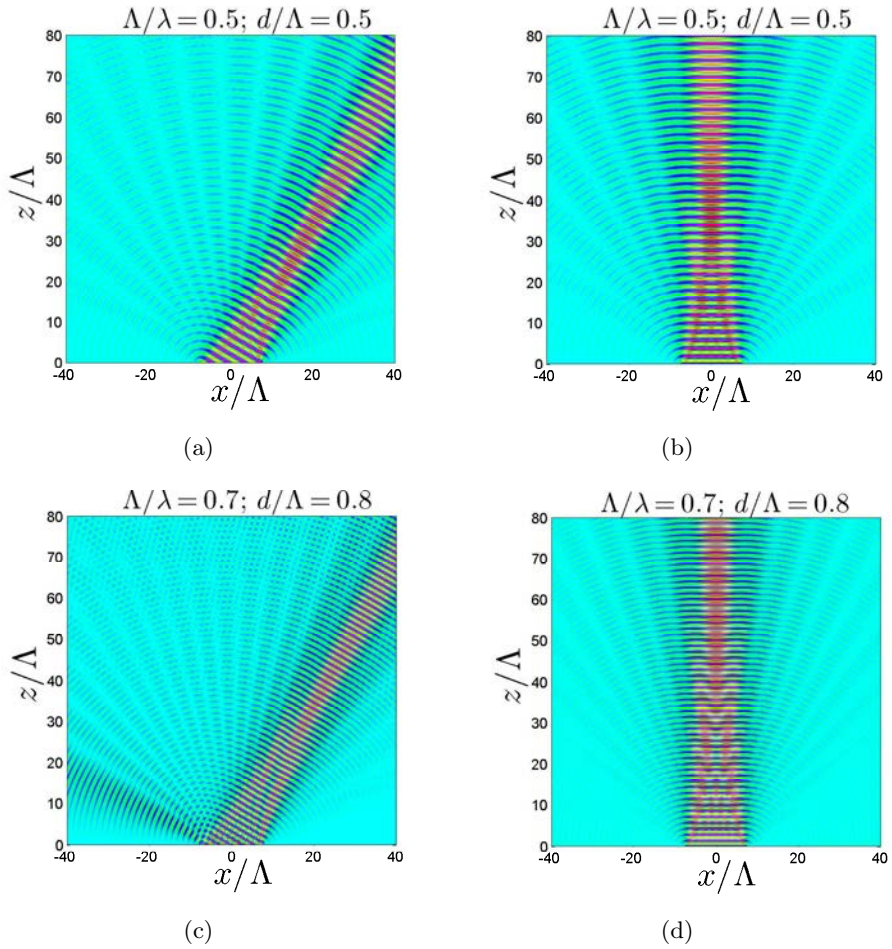

Figure 3.6. 2D view of the generated pressure wave-field in the medium above baffle plane $z > 0$ for different values of Λ/λ and d/λ and the steering angles 30° (a),(c) and 0° (b), (d).

which series converges fast and can be easily evaluated numerically. Fig. 3.9 presents Bragg orders of the scattered wave-field for the case of small value of $K/k = 0.6$ and the slot width $d = 0.85\Lambda$ for two different values of the incidence angle $\vartheta = \{10°, 30°\}$.

The directional characteristics of the wave detection by baffles for several values of normalized (with respect to the wave-length of the incident wave) slot width d/λ and the baffle period Λ/λ are shown in Fig. 3.10. Specifically, the Figs. 3.10(a), 3.10(c) and 3.10(e) present the magnitude of the total force $\bar{p}(\theta)$ exerted on baffle, and Figs. 3.10(b), 3.10(d) and 3.10(f) its real and imaginary

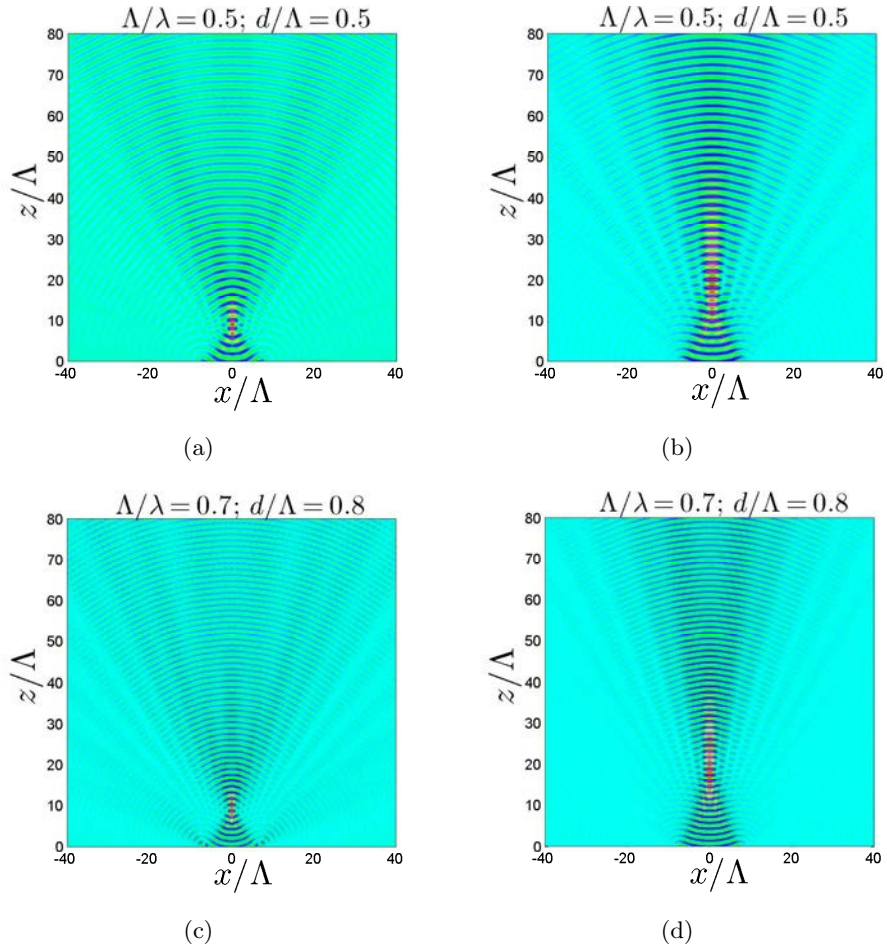

Figure 3.7. 2D view of the generated pressure wave-field in the medium above baffle plane $z > 0$ for different values of Λ/λ and d/λ focused at the distances of 10Λ (a),(c) and 20Λ (b), (d).

parts for $\Lambda/\lambda = 0.5$, $d/\lambda = \{0.1, 0.25, 0.4\}$, $\Lambda/\lambda = 0.7$, $d/\lambda = \{0.1, 0.3, 0.6\}$ and $\Lambda/\lambda = 1.5$, $d/\lambda = \{0.8, 1.0, 1.5\}$, respectively. The inflection points of the curves are easily noticed. The phenomenon takes place when, for instance, the -1st Bragg component of the scattered field (see Fig. 3.10(e)) approaches the tangential direction of propagation with respect to the baffle system, that is at $r - K \to -k$. In the above examples, the value $r = 10^{-4}k$ was used in the numerical computations instead of $r = 0$ in order to avoid evaluation of the corresponding limits $r \to 0$ [39]. In the example of receiver wave-beam synthesis,

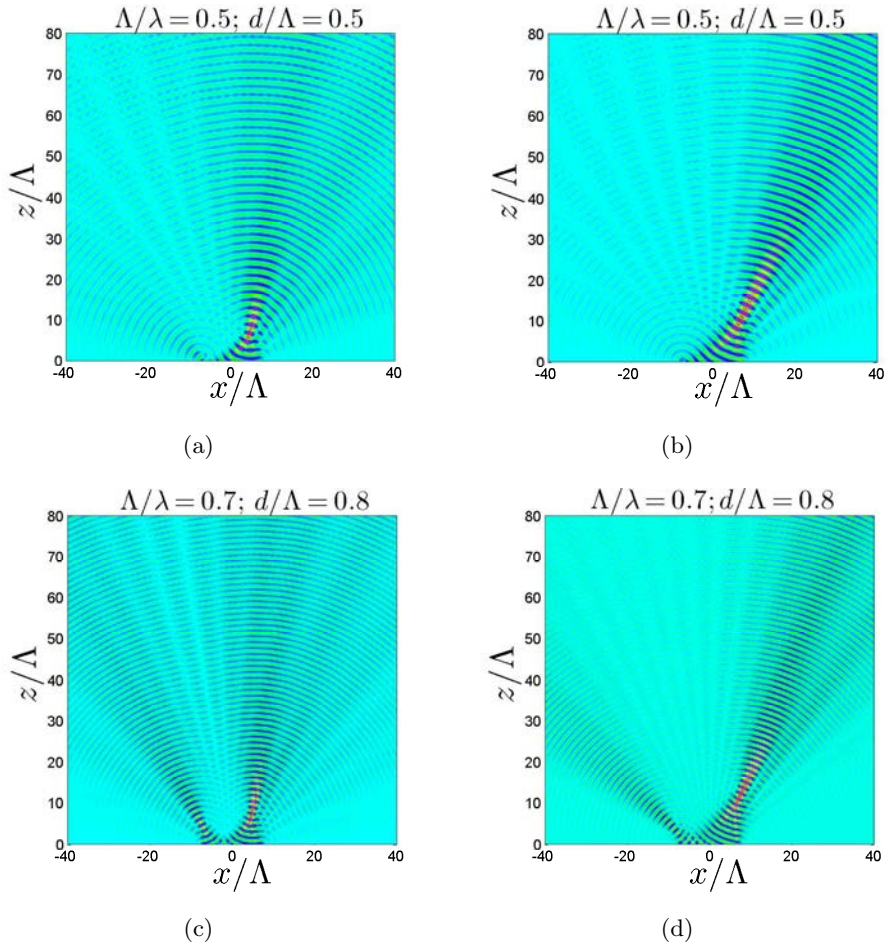

(a) (b) (c) (d)

Figure 3.8. 2D view of the generated pressure wave-field in the medium above baffle plane $z > 0$ for different values of Λ/λ and d/λ focused at the distances of 10Λ (a),(c) and 20Λ (b), (d) and additionally steered at the angle $\vartheta = 30°$.

the output signal was the Hamming-windowed [75] sum of signals $\bar{p}_l$ from 20 transducer elements:

$$S(\theta) = \sum_{n=1}^{20} \bar{p}_n W_n e^{jx_n k \cos\vartheta},\ x_n = (n - 10.5)\Lambda, \\ W_n = 0.08 + 0.92\cos^2(\pi(n - 10.5)/20), \tag{3.30}$$

where ϑ in this case denotes the chosen observation direction: 0° or 30° in the examples presented in Fig. 3.11, while the angle of incidence θ sweeps over an

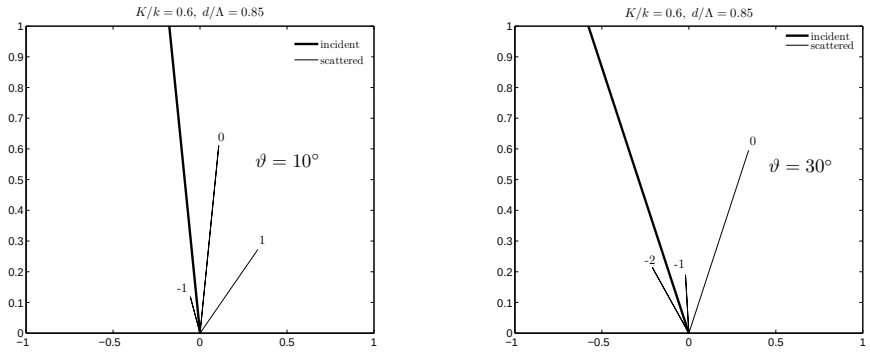

(a) (b)

Figure 3.9. Bragg orders of the scattered wave-field for the case of $K/k = 0.6$ and $w/\Lambda = 0.85$ and the incident angle (a) $\vartheta = 10°$, (b) $\vartheta = 30°$.

entire domain ($\bar{p}_n$ depends on $r = k \sin\theta$). The results are compared with ideal cases of point receivers responding to the incident wave by $\bar{p}_n = e^{-jrx_n}$. Since the baffle period $\Lambda = 0.7\lambda$ does not obey the spatial sampling theorem ($\Lambda \geq \lambda/2$), the grating lobe appears for $\vartheta = 30°$ in Fig. 3.11(d). The exact formula:

$$\theta_m = \operatorname{asin}\{\pm m\lambda/\Lambda - \sin\vartheta\} \tag{3.31}$$

yields for $\vartheta = 30°$ and $m = -1$ the value $\theta_{-1} = -68°$ which is in a good agreement with the numerical results shown in Fig. 3.11(d). For the case $\Lambda = 0.5\lambda$ illustrated in Fig. 3.11(b), there is no grating lobe for the considered angles of observation 0° and 30°, as expected.

In Fig. 3.12 dependence of the reflection coefficient $R_0 = p_0$ (see Eqs. (3.8)) versus the $kd/2$ is shown for different values of λ/Λ and different plane wave incidence angle. The choice of independent variable $kd/2$ corresponds to the analysis presented in [24] (see Eq. (6.1) of the cited paper). The graphs in Fig. 3.12 illustrate the normalized values $\bar{R}_0$ of the reflection coefficients with respect to its maximum value in the considered range of independent variable $kd/2$. The qualitative comparison of the results shown in Figs. 3.12(a) ($\vartheta = 0°$) and Figs. 3.12(c) ($\vartheta = 45°$) for the case of $d/\Lambda = 0.5$ reveals a good agreement with corresponding results obtained in [24] (compare with Figs. 3, 4 of the cited work).

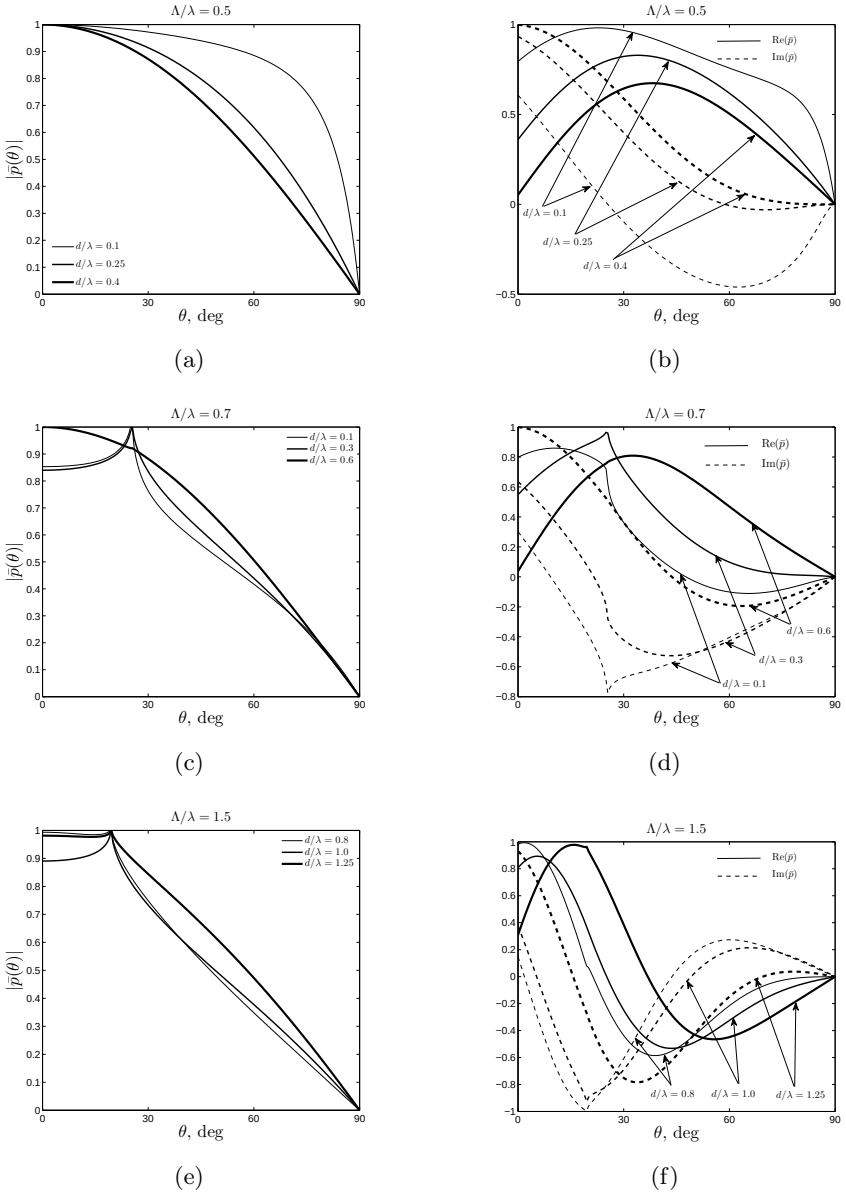

Figure 3.10. Directional characteristic of the wave detection by baffles $\bar{p}(\theta)$ for different values of system period Λ/λ and several values of slot width d/λ: (a), (c), (e) the magnitude of $\bar{p}(\theta)$, (b), (d), (f) its real and imaginary parts.

3.3. Finite baffle system

In the previous Section the full-wave analysis of the periodic baffle system was presented using the generalization of the BIS-expansion method of elec-

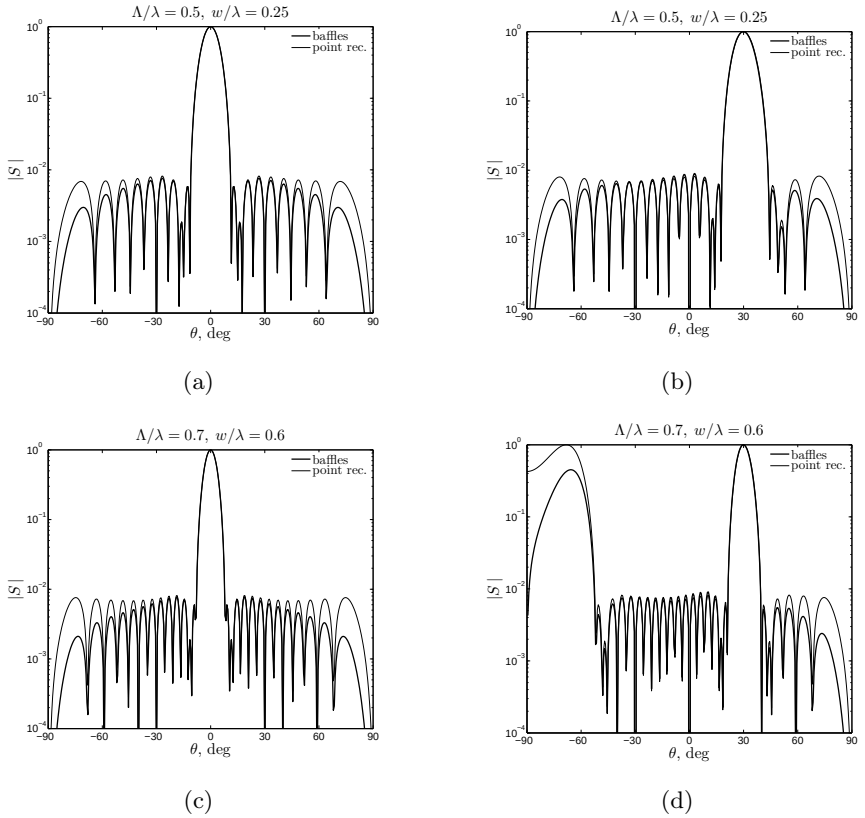

Figure 3.11. Directional characteristic of the wave detection by baffles computed from Eq. (3.30) for observation angles: (a), (c) $\vartheta = 0^\circ$ and (b), (d) $\vartheta = 30^\circ$; $\Lambda = 0.5\lambda$, $d = 0.25\lambda$ (a), (b) and $\Lambda = 0.7\lambda$, $d = 0.6\lambda$ (c), (d).

trostatic spectral approach. Specifically, the results of Section 2.2.1. were exploited to develop the corresponding extension of the method for application in the acoustic beam-forming analysis. In the current Section a similar mixed boundary-value problem is considered for the case of a finite system [76], illustrated in Fig. 3.13(a). To this end a generalization of the 'template functions' method (see Section 2.3.) combined with the BIS-expansion will be exploited in a similar manner as presented in the Section 2.4.2., where the electrostatics of strips in the external 'incident' (spatially harmonic) field was discussed. The detailed analysis concerning the boundary-value problem for the case of acoustic wave generation, formulated in the Section 3.1., will be presented here, particularly. Similarly, as in the case of periodic baffle array, the normal acoustic

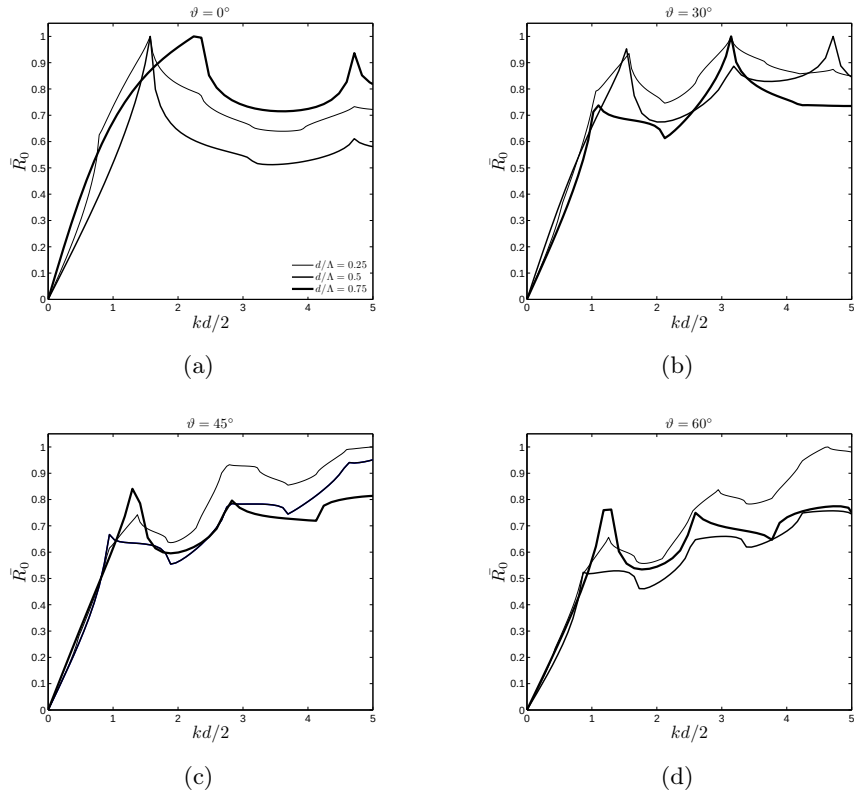

Figure 3.12. Normalized reflection coefficient $\bar{R}_0$ versus $kd/2$ for different values of d/Λ and several values of incident angle: (a) - normal incidence, (b) - incident angle $\vartheta = 30°$, (c) $\vartheta = 45°$ and $\vartheta = 60°$.

vibration vanishes on baffles and between them the acoustic pressure is given constant values (see Eq. (3.6)). Following the same approach as discussed in the Section 2.4.2., the initial finite baffle system of interest is approximated by some periodic one with certain large period Λ, comprised by the multiple replica of the analyzed structure (see Fig. 3.13(b)). This enables one to benefit from the BIS-expansion method.

Consider a finite system of N acoustically hard baffles distributed along the x-axis on the boundary plane $z = 0$ of the acoustic medium spanning for $z > 0$, as shown in Fig. 3.13(a). Their edges are defined by x-coordinates (a_i, b_i), $i = 1 \dots N$. The baffles are assumed to be infinitely long along the y-axis. Without loss of generality the baffles having the same width $2w$ (to facilitate the analogy with corresponding electrostatic methods it is convenient to adopt the $2w$ notion

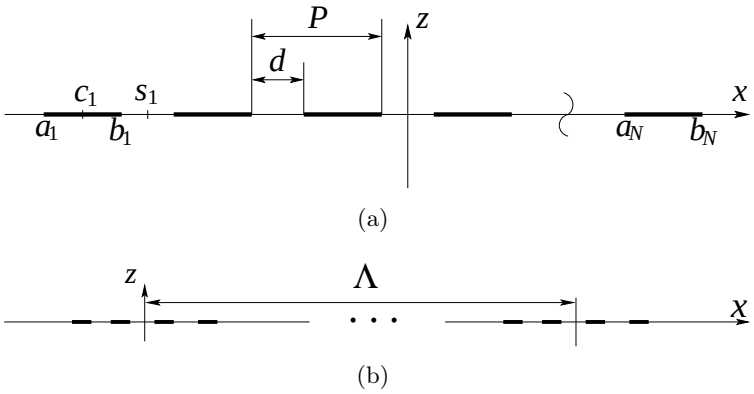

Figure 3.13. (a) A system of N rigid baffles (strips) on the boundary of acoustic media spanning for $z > 0$; (b) multi-periodic structure with certain large period Λ comprised by the replicas of the finite baffle system (a).

for the baffle width in contrast to w, applied in the case of periodic baffles) and equally spaced along the x-axis with the pitch P, which is usually the case in practical linear arrays. The slots between baffles are denoted by $d = P - 2w$ and the system spatial wave-number is $K' = 2\pi/P$. In this Section the notion of pitch is introduced to distinguish it from the period Λ as illustrated in Fig. 3.13 (in the acoustic literature usually the period of the transducer array is referred as the pitch, and the space between elements as the kerf). To find the solution fulfilling the boundary conditions given by Eq. (3.14), the 'template functions' which were defined in the Section 2.3., can be successfully exploited here. For convenience they are referred below in the fundamental form (see Eq. 2.68):

$$\begin{aligned} &\Phi^{(N)}(x) = j^{N-1} \prod_{m=1}^{N} \frac{1}{\sqrt{d_m^2 - (x - c_m)^2}}, \\ &\Phi^{(N,i)} \sim x^i \Phi^{(N)},\ i = 0...N-1, \end{aligned} \tag{3.32}$$

where w_m and c_m are the half-width and center coordinate of the m^{th} baffle. The function $\Phi^{(N)}$ is the basis 'template function' and the rest of them, $\Phi^{(N,i)}$, can be derived from $\Phi^{(N)}$, as shown in Eq. (3.32). The above functions have known spectral representations in the form of multiple convolutions of Bessel functions of the first kind $J_0(\xi d_m)$ and $J_1(\xi d_m)$. For the basis template function $\Phi^{(N)}$ the spatial-frequency counterpart is:

$$\Phi^{(N)}(\xi) = \Phi_1(\xi) * \Phi_2(\xi) * \cdots * \Phi_N(\xi), \tag{3.33}$$

where

$$\Phi_m(\xi) = \mathcal{F}\left\{\frac{1}{\sqrt{d_m^2-(x-c_m)^2}}\right\} = \left\{\begin{array}{l} J_0(\xi d_m)\, e^{jrc_m},\ \xi \geq 0, \\ 0,\ \xi < 0, \end{array}\right. \tag{3.34}$$

and $\mathcal{F}$ denotes the Fourier transform. The semi-finite support of the above functions, which is of great importance in the subsequent numerical analysis, must be emphasized here. The real and imaginary parts of $\Phi^{(N)}(x)$ vanish in subsequent domains of the x-axis, as required by the boundary conditions given by Eq. (3.14). For the acoustic boundary value problem considered here the following 'template functions' are introduced:

$$\begin{aligned} Q^{(N)}(\xi) &= \left\{\begin{array}{ll} \Phi^{(N)}(\xi), & \xi \geq 0 \\ \Phi^{*(N)}(-\xi), & \xi < 0 \end{array}\right\}, \\ V^{(N)}(\xi) &= S_\xi Q^{(N)}(\xi) = \left\{\begin{array}{ll} \Phi^{(N)}(\xi), & \xi \geq 0 \\ -\Phi^{*(N)}(-\xi), & \xi < 0 \end{array}\right\}. \end{aligned} \tag{3.35}$$

In the Section 2.3. it was shown, that the functions defined in Eq. (3.35) have their spatial counterparts vanishing on the x-axis in accordance with Eq. (3.14). Namely, $Q^{(N)}(x)$ vanishes between baffles as the $q(x)$ does (see Eq. 3.14) and $V^{(N)}(x)$ vanishes on baffles similarly as the $v(x)$. These functions, defined by Eq. 3.35, evaluated at discrete values of the spectral variable $\xi_n = n\Delta\xi$, are the discrete series in the numerical analysis and actually they represent, on the basis of the theory of FFT [65], the periodic functions in spatial domain with a certain large period $\Lambda = 2\pi/K,\ K = \Delta\xi$ (see Fig. 3.13(b)):

$$\begin{aligned} Q^{(N)}(x) &= \sum_n Q_n^{(N)} e^{-j\xi_n x},\ Q_n^{(N)} = Q^{(N)}(\xi_n), \\ V^{(N)}(x) &= \sum_n V_n^{(N)} e^{-j\xi_n x},\ V_n^{(N)} = V^{(N)}(\xi_n). \end{aligned} \tag{3.36}$$

The functions defined by Eq. (3.36) will be exploited further to satisfy the boundary conditions on the plane of baffles. Following the same considerations as in the Section 2.2.1. (see derivation of Eq. (2.46)), one first multiplies the functions in Eq. (3.36) by the term e^{-jmKx} and then takes a linear combinations of the resulting terms. After simple rearrangement of terms one readily obtains the following representation of the wave-fields $(q, v)(x)$ by their inverse Fourier transforms, written in the discrete form for the assumed large period Λ:

$$q(x) = \sum_{n=-\infty}^{\infty} q_n e^{-j\xi_n x}, \quad v(x) = \sum_{n=-\infty}^{\infty} v_n e^{-j\xi_n x}, \tag{3.37}$$

where

$$q_n = \sum_m \alpha_m Q^{(N)}_{n-m}, \;\; v_n = \sum_m \beta_m V^{(N)}_{n-m} = \sum_m \beta_m S_{n-m} Q^{(N)}_{n-m}. \tag{3.38}$$

Formally, in Eqs. (3.37) $\Lambda \to \infty$ should be applied ($K \to 0$), but in the approximation used here the Λ is large but finite (see discussion in Sec. 3.3.1. for more details).

The expansions given by Eq. (3.38) are the convolutions in spatial spectrum domain, written in discrete form, which in spatial domain correspond to the products of the 'template functions' $Q^{(N)}(x), V^{(N)}(x)$, defined in Eq. (3.35), with certain unknown functions $(\alpha, \beta)(x)$ represented by their Fourier transforms (in discrete form):

$$\alpha(x) = \sum_{n=-\infty}^{\infty} \alpha_n e^{-j\xi_n x}, \;\; \beta(x) = \sum_{n=-\infty}^{\infty} \beta_n e^{-j\xi_n x}. \tag{3.39}$$

The corresponding spectral samples $(\alpha, \beta)_n$ occur in Eq. (3.38) as unknown expansion coefficients that have to be determined. The functions in Eqs. (3.37), (3.38), being the solutions to the considered boundary-value problem for the finite system comprised of N baffles, satisfy the boundary conditions given by Eq. (3.14) due to the properties of the 'template functions' defined in Eqs. (3.35), (3.36). Now it has to be checked if the applied solutions, Eqs. (3.37), (3.38) satisfy the wave equation in the media $z > 0$, which equation is represented on the baffle plane $z = 0$ by the harmonic admittance $G(\xi)$, defined by Eq. (3.2) or, more conveniently, by its version $g(\xi)$ (see Eq. (3.3)). Only this part of the wave-field $(q, v)(x)$ which satisfies the radiation condition at $z \to \infty$ is involved in the solution, yielding the following relation for the n^{th} spectral line having wave-number ξ_n:

$$v_n = g(\xi_n) q_n. \tag{3.40}$$

Following the same considerations as for the case of infinite periodic baffle system a similar approximation can be applied for large $|n|$: $g(\xi_n) = \pm g_\infty$, $n > N_1$ (N_1 some large but finite integer). As was discussed earlier (see Section 2.2.1.) this is possible only if (compare with Eqs. (2.52) and (3.13)):

$$\beta_m = g_\infty \alpha_m. \tag{3.41}$$

Substituting Eq. (3.38) into Eq. (3.40) and taking into account Eq. (3.41), the following system of linear equations for unknown coefficients α_m is obtained:

$$g_\infty \sum_m \alpha_m [S_{n-m} - j(\eta_n/\xi_n)] Q^{(N)}_{n-m} = 0, \;\; m, n \in [-N_1, N_1]. \tag{3.42}$$

It can be easily checked by inspection, that outside the limits $m, n \in [-N_1, N_1]$ the above equations are satisfied directly.

To obey the last condition in Eq. (3.14), that the pressure takes given constant values in the slots between baffles, a similar technique as described in the Section 2.3. (see derivation of Eqs. (2.78) through (2.80)) is exploited. Specifically, given N baffles there are $N_s = N - 1$ slots and the same number of constraints which have to be satisfied. To this end the number of coefficients α_m in Eq. (3.42) should be increased to $2N_1+1+N_s$ and the above N_s constrains are added to the system of equations, Eq. (3.42):

$$p_i \equiv p(x = s_i) = \int q(x)dx \mid_{x=s_i},\ i \in [1, N_s]\,. \tag{3.43}$$

where s_i is the i^{th} slot center (see Fig. 3.13(a)). According to definition $q = p_{,x}$ (see Section 3.1.), the pressure at the slot centers can be evaluated by integration of $q(x)$, as in Eq. (3.43). This corresponds to the division by ξ of the $q(\xi)$ in spectral domain. Here the known spatial-frequency representation of the template solution $Q^{(N)}(\xi)$ given by Eq. (3.35) proves useful to find the pressure at the slot centers without performing the integration like in Eq. (3.43), in a similar manner as was presented in the Section 2.3. (see Eqs. (2.78)):

$$p(x) = \mathcal{F}^{-1}\{-jq(\xi)/\xi\} = \frac{1}{2\pi}\int_{-\infty}^{\infty} |\xi|^{-1} q(\xi) e^{-j\xi x} d\xi, \tag{3.44}$$

where $\mathcal{F}^{-1}$ denotes the inverse Fourier transformation. Consequently, substituting Eqs. (3.37), (3.38) into Eq. (3.44) one obtains immediately for the pressure p_i in the slot center between the i^{th} and $(i+1)^{\text{th}}$ baffles:

$$p_i = j\sum_m \alpha_m \mathcal{F}^{-1}\left\{\frac{Q^{(N)}_{l-m}}{\xi_l}\right\} \mid_{x=s_i},\ i \in [1, N_s]\,,\ l \in [-L, L-1]\,. \tag{3.45}$$

For numerical evaluation of the Fourier transformations usually the FFT algorithm is used. For this purpose the number of samples $2L$ in the above discrete series is usually integer power of 2. Similarly, as in the case of electrostatic problem for strips, here the discrete representation of the inverse Fourier transform is used for numerical evaluation of the pressure $p_i \equiv p(x = s_i)$. Since the pressure in the slot between baffles takes constant value, it can be determined in any point $\tilde{x}_i$ within the i^{th} slot. This considerably simplifies the analysis, because the inverse Fourier transform in Eq. (3.45) is evaluated in discrete points equally spaced on the x axis with the step $\Delta x = \pi/(L\Delta\xi)$ [65]:

$$p_i \equiv p(x = s_i) = p(\tilde{x}_i). \tag{3.46}$$

In this case, for instance, $\tilde{x}_i$ can be the closest point to the slot center $x = s_i$. Summarizing, the system of linear equations for unknown α_m for $m \in [-N_1 - M_l, N_1 + M_u]$, where $M_u = M_l = N_s/2$ for even N_s and $M_l = (N_s-1)/2$ and $M_u = (N_s + 1)/2$ for odd N_s, is:

$$[A_{nm}][\alpha_m] = [b_n]\,, n \in [-N_1, N_1 + N_s]\,. \tag{3.47}$$

The elements of matrix A_{nm} are given by Eq. (3.42) and $b_n = 0$ for $n \in [-N_1, N_1]$ and

$$\begin{aligned} &A_{nm} = \mathcal{F}^{-1}\left\{\frac{Q^{(N)}_{l-m}}{\xi_l}\right\}|_{x=s_i},\ b_n = p_i, \\ &n \in [N_1 + 1, N_1 + N_s]\,, i \in [1, N_s]\,,\ l \in [-L, L-1]\,. \end{aligned} \tag{3.48}$$

Solving the system of linear equations given by Eq. (3.47) for unknown coefficients $\alpha_m,\ m \in [-N_1 - M_l, N_1 + M_u]$ the solution to the considered boundary-value problem can be obtained from Eq. (3.37) using Eqs. (3.38) (note, $\beta_m = \alpha_m/(\omega\rho_a)$).

3.3.1. Beam-forming by finite baffle system

In this Section some numerical examples of the acoustic beam-forming by the finite baffle systems considered in the previous Section are given. As it was emphasized in the earlier Sections, the main advantage of the method of analysis, discussed in this work, is that it yields the spatial spectrum of the acoustic pressure field distribution on the baffle plane directly. Therefore, the radiation pattern can be evaluated as the inverse Fourier transform of the $p(\xi)$ which is related to $q(\xi) = -j\xi p$ (note, $p(\xi \to 0) = 0$) in a similar way as in the case periodic baffle array (see Sec. 3.2.1., Eq. (3.22)):

$$p_R(\theta) = p(k\sin\theta)\cos\theta\,\frac{k}{K}\sqrt{\frac{j2\pi}{kR}}\,e^{-jRk}, \tag{3.49}$$

where $K = 2\pi/P$, P - is the pitch. The angular dependence in the far-field region can also be written in terms of the $q(\xi)$ as follows:

$$p_R(\theta) \sim q(k\sin\theta)\cot\theta. \tag{3.50}$$

In the computed numerical example, shown in Fig. 3.14, the beam-steering by a finite system comprised of 8 baffles is shown. The far-field radiation pattern is evaluated using Eq. (3.49) for given pressure in the slots: $p_l = e^{jlPk\sin\vartheta}$, $l = 1 \ldots 7$, and different values of the steering angle: $\vartheta = 0°$ and $20°$. Two cases

of the system pitch are considered: $P = 0.7\lambda$ in Fig. 3.14(a) and $P/\lambda = 1$ in Fig. 3.14(a). For convenience, the pressure distribution (its real part is depicted by the solid and imaginary part - by the dashed line) on the baffle plane are shown in Figs. 3.14(b) and 3.14(d).

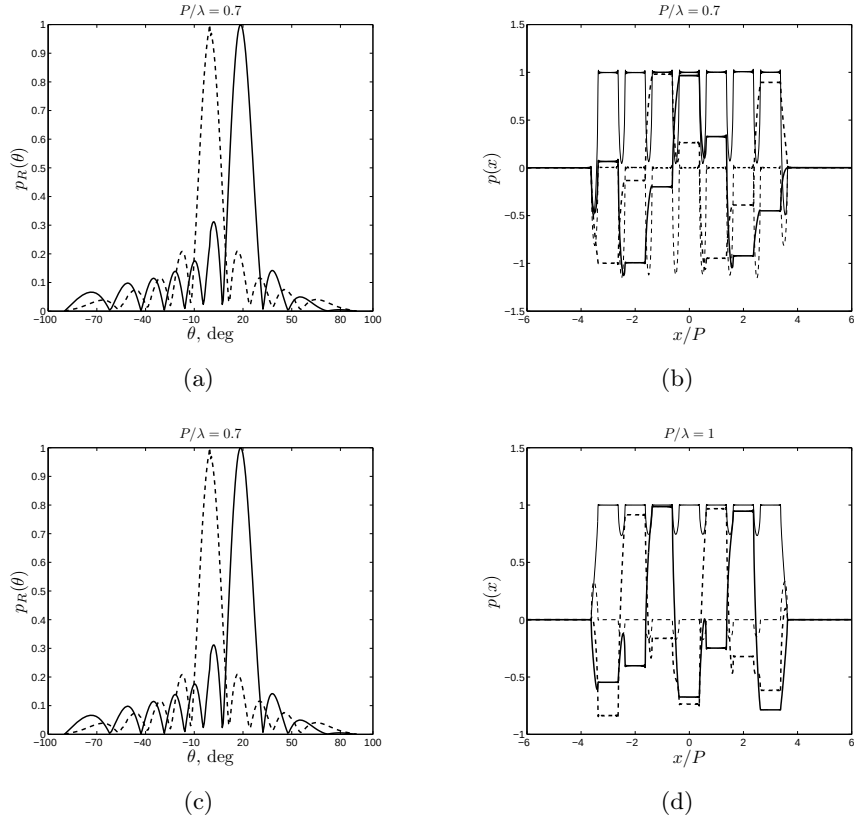

Figure 3.14. Radiation pattern $p(\theta)$ for (a) $P/\lambda = 0.7$, (c) - $P/\lambda = 1$ and 8 active slots excited with linear phase shift and steering angle $\vartheta = 20^\circ$ (solid line) and 0° (dashed line); (b), (d) - corresponding pressure (solid line - its real part and dashed line - its imaginary part) filed distribution on baffles: thick line - $\vartheta = 20^\circ$ and thin line - $\vartheta = 0^\circ$; $d/P = 0.75$.

As can be seen in Fig. 3.14(c) for $P/\lambda = 1$ the grating lobe appears for steering angle $\vartheta = 20^\circ$ due to violation of the spatial sampling theorem. The corresponding 2D pressure field distribution in the media $z > 0$ evaluated from Eq. 3.5 is shown in Fig. 3.15 for the considered baffle system and the steering angles $\{0^\circ, 20^\circ\}$; the system parameters are similar as above: $P/\lambda = 0.7$ in Figs. 3.15(a), 3.15(b) and $P/\lambda = 1$ in Figs. 3.15(c), 3.15(d), respectively.

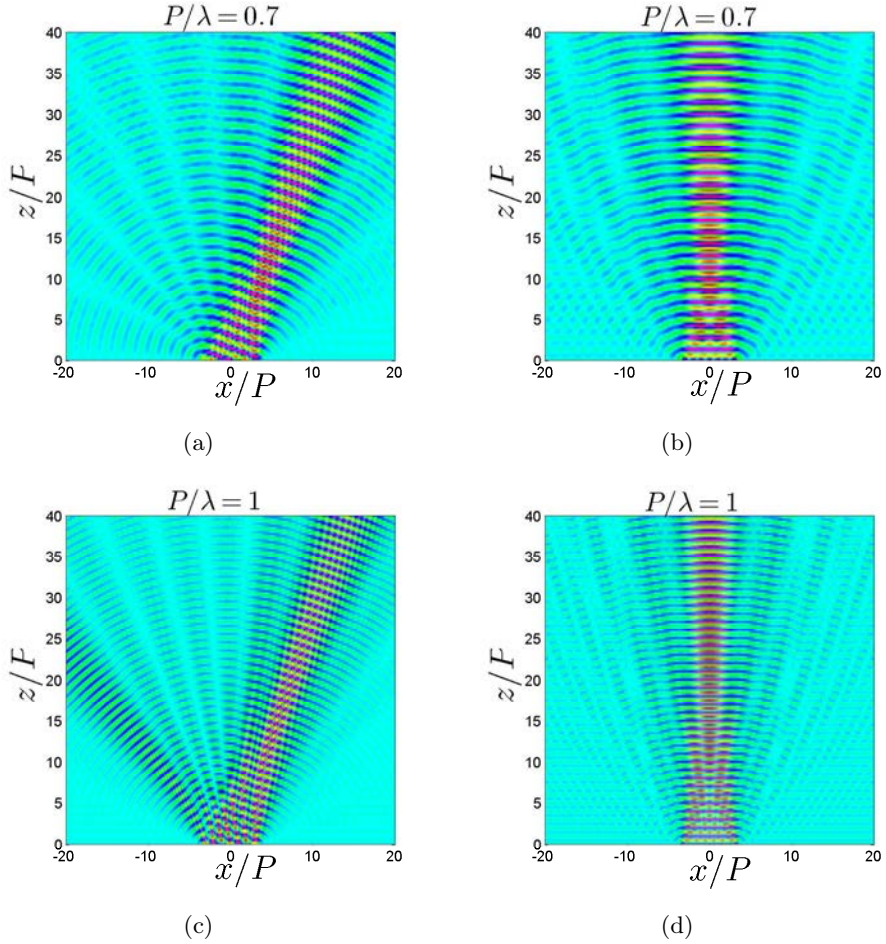

Figure 3.15. 2D view of the generated pressure wave-field in the medium above baffle plane $z > 0$ for different values of P/λ and the steering angles 20° (a),(c) and 0° (b), (d); $d/P = 0.75$.

In Fig. 3.16 the examples of the wave-beam focusing achieved by the proper quadratic phase shift for the active slots excitations: $p_l = e^{jk(lP)^2\beta}$, $l = -3, ..., 3$, where $\beta = 1/2F$ and $z = F$ - is the focal plane (see discussion in Sec. 3.2., Fig. 3.7), are illustrated for the same baffle system as in the examples shown above in Fig. 3.15. The wave-beam is focused at the depths of $F = 5P$ and $F = 10P$ for the considered values of $P/\lambda = 0.7$ and 1.

Combining the linear and quadratic phase shifts between active slots in the baffle array the focusing and steering of the generated wave-beam can be accomplished (see discussion in the Section 3.2., Fig. 3.8). The corresponding

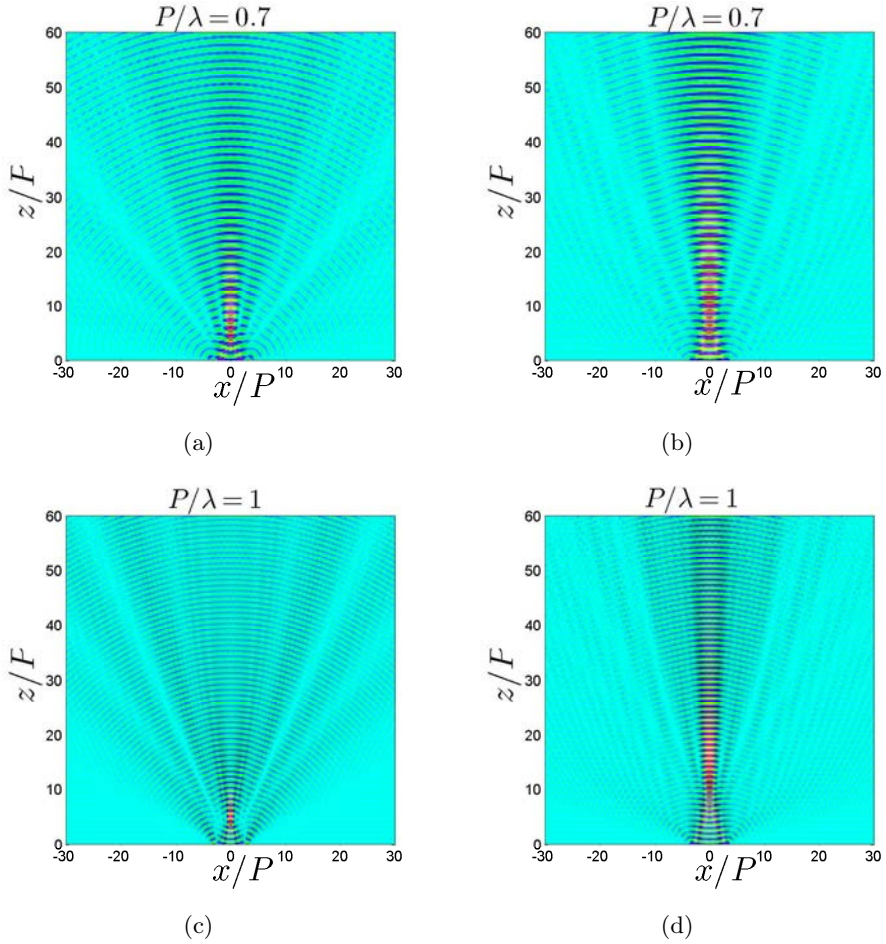

Figure 3.16. 2D view of the generated pressure wave-field in the medium above baffle plane $z > 0$ for different values of Λ/λ focused at the distances of $5P$ (a),(c) and $10P$ (b), (d); $d/P = 0.75$.

computed examples are shown in Fig. 3.17 where the 2D pressure field distribution in the media $z > 0$ is shown for the same baffle system (see Fig. 3.16). Here the focused beam at the distances $F = 5P$ and $F = 10P$ is additionally steered at the angle $\vartheta = 20°$ by combining the linear and quadratic phase shifts as in the examples shown in Figs. 3.15 and 3.16, respectively.

As it was stated in the Section 2.3. in the 'template functions' method the care should be taken when evaluating the convolutions using Eqs. (3.33) and (3.34). To this end in the case of electrostatic problem for finite system of

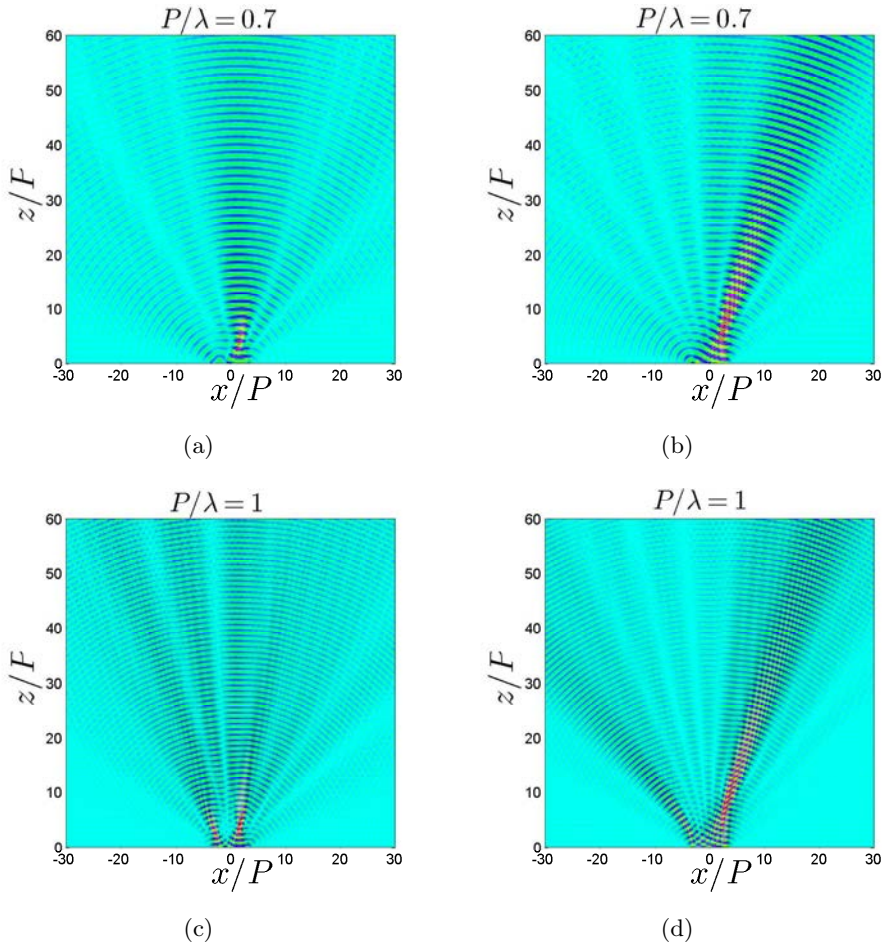

Figure 3.17. 2D view of the generated pressure wave-field in the medium above baffle plane $z > 0$ for different values of P/λ focused at the distances of $5P$ (a),(c) and $10P$ (b), (d) and additionally steered at the angle $\vartheta = 20°$.

conducting strips the advanced numerical algorithms were developed [63]. These can also be adopted in the case of the acoustic beam-forming by finite baffle system discussed here.

It should be noted, that the 'template functions' have to be evaluated at discrete points in spatial spectrum domain with sampling interval $\Delta\xi = 2\pi/\Lambda$. In order to make the multi-periodic system approximation finer, $\Lambda \to \infty$ should be applied (see Fig. 3.13), yielding $\Delta\xi \to 0$. In fact, Λ can be applied large but finite. For instance, in the numerical calculations, presented above, $\Lambda \approx 10^2 P$

(see Fig. 3.13(b)) was assumed, which is sufficient for considering the finite baffle array as an isolated cell of the multi-periodic system [76]. Similarly, as in the case of periodic baffle array, to obey the approximation which yields the Eq. (3.41) (see Eq. (3.12) in the Section 3.2.), it is sufficient to consider the spatial spectrum components bounded by certain upper frequency ξ_u, where $\xi_u \approx (5 \div 10)k$. For $k \sim K'$, where $K' = 2\pi/P$ is the spatial wave-number of the finite baffle system (not to be confused with $K = 2\pi/\Lambda$ - the multi-periodic system spatial wave-number), this yields $N_1 \sim 10^3$ in Eq. (3.42) and approximately $2N_1$ unknown coefficients α_m to be determined from Eq. (3.47).

It should be noted, however, that for the purpose of accurate evaluation of the integrals in Eq. (3.43) by means of the inverse Fourier transform (see Eq. 3.45), yielding the pressure distribution on the plane $z = 0$, the 'template functions' have to be evaluated over a wider spatial spectrum domain [38]. The aspects of numerical evaluation of the 'template functions' given by Eqs. (3.33) and (3.34) (in application to electrostatic analysis of finite systems of conducting strips) were studied thoroughly in [63]. More specifically, it was shown that for the number of baffles $N = 10 \div 20$ they should be evaluated within the spatial spectrum domain $(0, \xi'_u)$, where $\xi'_u \approx 50k$. Note, that the semi-finite support of the 'template function' $\Phi^{(N)}(\xi)$, given by Eqs. (3.42) and (3.34), is exploited here. This property simplifies considerably evaluation of multiple convolutions in Eqs. (3.42) [38, 63] (see also discussion in Section 2.3.). Therefore, it is sufficient to evaluate the 'template functions' for the purpose of evaluation of integrals in Eq. (3.45) within the domain $(0, \xi'_u)$, which yields $L \sim 2^{13}$ samples in the corresponding data-sets for FFT algorithm, provided $\xi'_u = 50k$ is assumed. For larger number of baffles, in order to maintain the accuracy of integration in Eq. (3.45) the sampling step $\Delta\xi$ should be decreased [63]. Specifically, for $N = 30 \div 40$ baffle system at least $L \sim 2^{15}$ samples of the 'template functions' within the domain $(0, \xi'_u)$ should be evaluated. In this case the $\Delta\xi$ should be decreased at least by a factor of 4 yielding the corresponding increase of N_1 in Eq. (3.42) to approximately $5 \cdot 10^3$. Moreover, the system of equations given by Eq. (3.48) tends to be bad-conditioned for growing N (see also discussion in Conclusion), which restricts the application of the method described in this Section to small systems, comprising approximately $10 \div 20$ baffles. This is vastly insufficient for modeling of modern practical transducer arrays used in ultrasound applications having at least 128 elements. Nevertheless, the method presents original and uncommon theoretical approach to solving the acoustic beam-forming problem by finite baffle system. In the case of practical acoustic transducer arrays having large number of elements the method of analysis developed for periodic structures which was discussed in details in the Section 3.2. can be successfully

applied with sufficient accuracy for practical applications. This is illustrated in the next Chapter where the developed method is used to improve performance of the ultrasound imaging technique based on synthetic aperture principles.

4

Application in ultrasound imaging

In this Chapter practical application of the results of acoustic beam-forming analysis presented in the Chapter 3 will be shown. Specifically, the synthetic aperture method in medical ultrasound imaging will be discussed here. As evidenced below the results obtained for periodic baffle array in the Section 3.2. can be successfully exploited to improve its performance. Ultrasound imaging has become one of the primary techniques for medical imaging mainly due to its accessibility, non-ionizing radiation, and real-time display. Similar techniques are also employed in the non-destructive testing and evaluation of materials and constructions [5, 6, 8]. The phased arrays, widely exploited in these applications for wave generation and detection, enable high speed inspection with increased sensitivity and coverage compared with conventional ultrasonic techniques. The most popular ultrasound medical scanning is provided by the pulse-echo modality, in which the piezoelectric transducers act as both the transmitters of the acoustic pulse and the detectors of reflected and scattered waves. In the modern medical ultrasound B-mode (brightness mode) scanners e.g. a linear (1D) array of transducers simultaneously scans a plane through the body that can be viewed as a two-dimensional image on the screen. It represents the magnitude of the back-scattered ultrasound wave-field (the pressure measured by the transducer) and relates to the impedance mismatch of tissues in the body.

High resolution ultrasound images are usually obtained by using phased array transducers and delay-and-sum beamforming techniques. However, proper focusing at the whole image space is done at a large cost of slowing the frame rate. Synthetic aperture imaging methods offer a solution to this problem. Initially implemented in remote sensing/imaging by radars [77, 78] and in sonar imaging [79, 80] later they found their application in the ultrasound imaging [81] where they are also known as synthetic aperture focusing techniques (SAFT). In SAFT imaging, at each time a single array element transmits a pulse and receives the echo signal [82]. The drawbacks of this method are the low signal-to-noise ratio (SNR) due to the low energy of the transmitted pulse and inferior contrast resolution due to the higher side-lobe level as compared to the conventional

phased arrays, resulting in poor image quality. To overcome these difficulties a multi-element synthetic aperture focusing (M-SAF), as an alternate to the SAFT, was proposed [83]. A group of elements transmits and receives signals simultaneously. The transmit beam is unfocused to emulate a single element response. The acoustic power and the SNR are increased as compared to SAFT. Further significant improvement of the ultrasound image quality was due to the synthetic transmit aperture method (STA) [84, 85]. At each time a single array element transmits an ultrasound pulse and all elements receive the echo signals. The advantage of this approach is that a full dynamic focusing can be applied in transmit and receive modes, giving the high imaging quality comparable to the conventional phased arrays beam-forming. To improve the SNR and the visualization depth of the resulting synthesized images the multi-element synthetic transmit aperture (MSTA) [40] was proposed. MSTA is done by splitting the transmit aperture into several sub-apertures. At each time a single sub-aperture comprised of several elements transmits an ultrasound pulse and all the elements receive the echo signals. This allows to increase the transmit power, which, in turn, leads to improvement of the SNR and penetration depth. Moreover, a data acquisition cycle can be reduced to several firings which results in considerable improvement of the frame rate at the cost of minor decrease of the final synthesized image quality.

A 'common' approach to the synthetic aperture methods in ultrasound imaging considers a single element of a multi-element probe as a point source transmitting a spherical wave-front [86] This approach is reasonable for elements having their size much smaller than the wavelength of the probing or interrogating signal. Yet, when the element size is comparable to the wavelength of the probing wave the influence of the element's directivity on the wave field generation and reception can no longer be neglected. Hence, an application of the simple point source model to reconstruct the image might lead to errors and artifacts worsening the quality of the resulting image. To alleviate this problem a proper modification of the MSTA algorithm taking into account the transmit/receive sub-aperture directivity when the element's lateral width is comparable with the operating frequency wavelength can be developed. This is introduced by applying predefined apodization weights evaluated for every focal point in the image in both transmit and receive modes. To this ends the results of the beamforming analysis of the periodic baffle array discussed in the Section 3.2. will be exploited.

Modification and control of the beam patterns by applying the aperture apodization in the ultrasonic imaging systems was reported in several works [1, 87, 88]. Frequently, fixed weights corresponding to Hamming-, Hann-, Blackman

etc. window functions [89, 90] are applied to echo signals recorded from different channels during dynamic focusing of the received beam. To obtain a more flexible control over transmitted and received wave-fields, the specific, optimal sets of weights generated for each focus point in the image are determined. This enables synthetization of the desirable beam patterns [91]. The sets can also be used to obtain the required field distribution at a given, user controlled, depth [92].

As evidenced in the following in this Chapter the application of proposed apodization weights considerably improves the penetration depth and diminishes the hazy, blurring artifacts observable in the case of the conventional MSTA algorithm. This improvement in imaging quality is particularly visible in the immediate vicinity (near -field distance) of the transducer surface, which is critical in such applications as breast and skin imaging. The image optimization in the immediate vicinity of the scanhead surface using the MSTA (and STA) approach with individual weighting functions was not explored previously.

4.1. Multi-element synthetic aperture method

Before proceeding further it is expedient to give a brief introductory discussion concerning the fundamentals of the MSTA method. In the MSTA approach at each emission a transmit aperture comprised of several elements is used as it is illustrated in Fig. 4.1. The back-scattered waves are received by each element

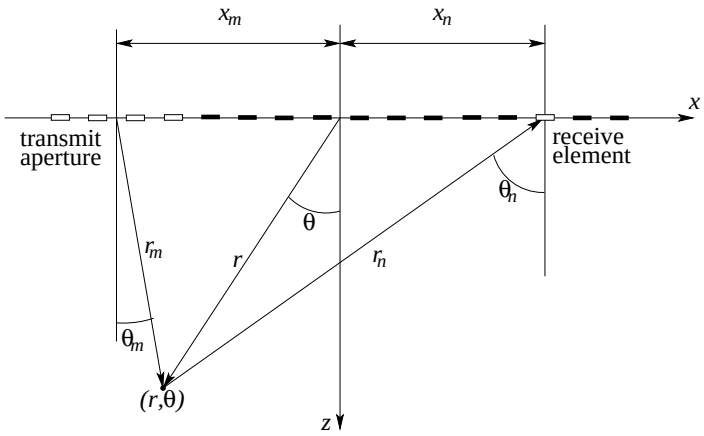

Figure 4.1. Transmit and receive elements combination and the focal point in MSTA method.

independently and the resulting RF echo signals are digitized and stored in memory for further processing. For an N-element array, N_t - element transmit

aperture and N_{sh}-element shift of the transmit aperture between subsequent emissions, there are $M = \lceil (N - N_t)/N_{sh} \rceil$ emissions in each cycle altogether, where $\lceil x \rceil$ denotes the integer ceiling of x. Assuming $N_t = 1$ results in conventional synthetic transmit aperture (STA) method. In the case of MSTA the frame rate is increased by N/M as compared to the STA method due to decrease of the total number of emissions, which speeds up the data acquisition process. Thus, for N-element aperture upon completion of the data acquisition cycle $M \times N$ RF echo signals are recorded for further image synthetization. To this end the coherent summation of all received RF echoes is performed. For the N-element array for each point in the image, the final focused signal can be expressed as follows [93]:

$$S_{MSTA}(r, \theta) = \sum_{m=1}^{M} \sum_{n=1}^{N} s_{m,n} \left(\frac{2r}{c} - \tau_{m,n} \right), \tag{4.1}$$

where $s_{m,n}(t)$ is the RF echo signal and $\tau_{m,n}$ is the round-trip delay defined for the (m, n) transmit/receive pair by expression:

$$\tau_{m_n} = \tau_m + \tau_n, \; 1 \leq n \leq N, \; 1 \leq m \leq M. \tag{4.2}$$

The corresponding delays for m^{th} transmit and n^{th} receive elements relative to the imaging point (r, θ) can be easily evaluated by tracing the path of the ultrasound wave as follows:

$$\tau_i = \frac{1}{c} \left(r - \sqrt{r^2 + x_i^2 - 2 x_i r \sin \theta} \right), \; i = m, n, \tag{4.3}$$

where x_m, x_n are the positions of the m^{th} transmit and n^{th} receive elements, respectively, and r, θ, are the polar coordinates of the focal point with respect to the origin, placed in the center of the transducer's aperture (see Fig. 4.1). The first and second summations correspond to the transmit and receive focusing, respectively. It should be noted that the angular dependence is not taken into account in the applied point-like source model. However, when the width of the array element is comparable to the wavelength, corresponding to the nominal frequency of the emitted signal, the point-like source model becomes inaccurate. The directivities of the individual transmit and receive elements influence the partial contributions of the resulting focused signal $S(r, \theta)$ in Eq. (4.1) depending on the mutual positions of the focal point and transmit/receive pair, determined by the angles θ_m, θ_n (see Fig. 4.1).

4.2. Modified multi-element synthetic aperture method

In this Section a modified STA imaging algorithm which accounts for the element directivity function and its influence on the total focused signal $S(r, \theta)$ is presented. The underlying idea can be conveniently introduced by assuming two similar reflectors that are located at the points with polar coordinates (r_i, θ_i); $i = 1, 2$, and considering the m^{th} element of the transducer array, which acts as transmitter (see Fig. 4.2). For simplicity a single-element transmit aperture is assumed without loss of generality (thus referring to the STA algorithm - a particular case of the MSTA method).

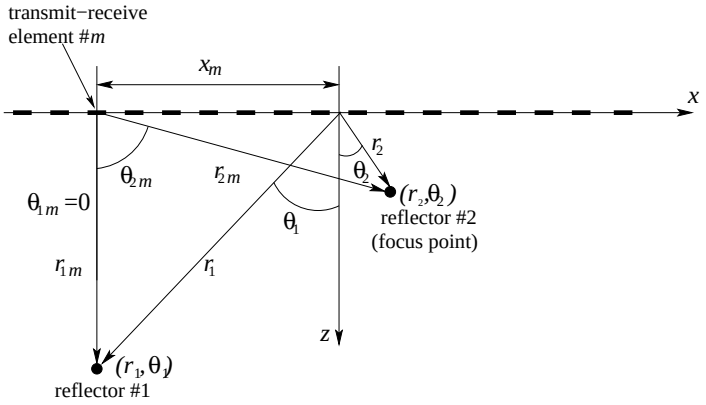

Figure 4.2. Transmit and receive elements combination and the focal point in MSTA method.

The corresponding RF echo signal received by this element is denoted as $s_{m,m}(t)$. Since $r_{1m} = r_{2m}$, both reflectors contribute to the corresponding echo signal $s_{m,m}(t)$ simultaneously due to the equal round-trip propagation time: $2r_{im}/c$; $i = 1, 2$. The scattering amplitude of the reflector #1 located at the point (r_1, θ_1) is dominant, since the angle θ_{1m} coincides with the m^{th} element's normal direction (direction of its maximum radiation), whereas the reflector's transmit-receive efficiency at the angle θ_{2m}, corresponding to the reflector #2, is lower. If the focus point coincides with the location of the reflector #2, the partial contribution from $s_{m,m}(t)$ to $S(r_2, \theta_2)$ evaluated from Eq. (4.1) introduces the spurious echo from the reflector #1. This is in addition to the signal scattered from the reflector #2 (which is relatively small due to the large observation angle θ_{2m}). Due to its location (the normal direction with respect to the considered m^{th} element), the corresponding 'false' contribution is relatively large, which results in an excessive signal amplitude increase at the point (r_2, θ_2) of the final image. In other words, the scattered signals from distant reflectors

(scatterers) are spuriously "transferred" into the region adjacent to the transducer aperture, where the large observation angles exist, and produce an image distortion there. To alleviate this problem, a proper spatial filtering, accounting for the observation angle in accordance with the transmit/receive element directivity function, is needed. Assume that the angular directivity function of the considered element is known and denoted by $f(\theta_m)$, where θ_m is measured from the m^{th} element normal direction (see Fig. 4.2). To suppress the influence from the reflector #1 on the imaging signal $S(r_2, \theta_2)$ at the focal point (r_2, θ_2), coinciding with location of the reflector #2, the partial contribution of the echo $s_{m,m}(t)$ is weighted by the corresponding value of $f(\theta_{2m})$. This corresponds to the spatial filtering of the superposed signal in accordance with the positions of the focal point and transmit/receive elements, accounting for their angular directivity functions. The above considerations lead to the following modification of the MSTA imaging algorithm using arbitrary number of elements in transmit mode:

$$\begin{aligned} S^{mod}_{MSTA}(r,\theta) &= \sum_{m=1}^{M}\sum_{n=1}^{N} w_{mn} s_{m,n}\left(\frac{2r}{c} - \tau_{m,n}\right), \\ w_{mn} &= f_T(\theta_m) f_R(\theta_n),\ \theta_i = \theta_i(r,\theta),\ i = m,n, \end{aligned} \tag{4.4}$$

where $\theta_i(r,\theta)$, $i = m,n$ are the corresponding observation angles for the transmit and receive elements and $f_T(\theta_m)$, $f_R(\theta_n)$ are their directivity functions, respectively. Note, that the angles θ_m and θ_n depend on the spatial position of the focal point (r,θ). In the case of STA algorithm [94] the corresponding directivity function of single-element transmit and receive apertures, which is used for evaluation of weights w_{mn}, can be calculated in the far-field approximation using analytical expression [68]:

$$f(\theta) = \frac{\sin\left(\pi d/\lambda \sin\theta\right)}{\pi d/\lambda \sin\theta}\cos\theta, \tag{4.5}$$

where d is the element width, and λ is the wavelength. A few representative examples of the directivity patterns determined for a single transducer element having width of $d = 0.28$ mm, and operating at frequencies of $4, 5$, and 7.2 MHz are shown in Fig. 4.3. These patterns correspond to the ratios $d/\lambda = 0.75, 0.94$ and 1.35, respectively.

The results shown in Fig. 4.3 are in agreement with the experimental results reported in [68]. The above Eq. (4.5) applies to a strip transducer with a time harmonic uniform pressure distribution along its width and is obtained by means of the Rayleigh-Sommerfeld formula in the far-field region [95]. The value of λ in Eq. (4.5) corresponds to the working frequency of the probing wave. In

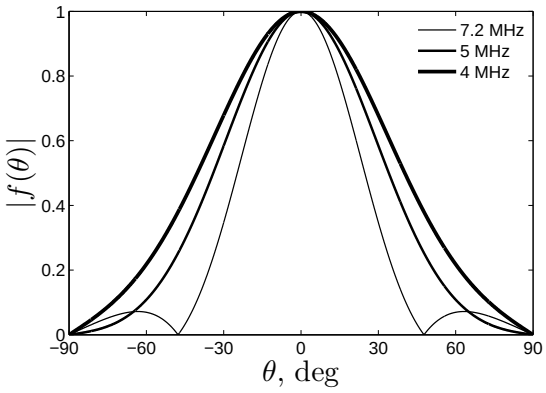

Figure 4.3. Directivity functions for transducer array element with $d = 0.28$ mm for different frequencies $4, 5, 7.2$ MHz corresponding to $d/\lambda = 0.75, 0.94, 1.35$.

the case of MSTA method discussed here, however, the analytic formula given by Eq. (4.5) cannot be used for evaluation of the directivity function of the multi-element transmit aperture (it can be applied, however, to compute the weights for the single-element receive aperture, for instance). Here, instead, the results of the solution of a mixed boundary-value problem for periodic baffle array discussed in the Section 3.2. can be successfully used in order to evaluate the corresponding directivity functions. Specifically, the expression given by Eq. (3.22) is used to this end, which is rewritten here in slightly modified form:

$$f(\theta) = p(k \sin\theta)\cos(\theta), \tag{4.6}$$

where $f(\theta)$ is a normalized value of p_R in Eq. (3.22) representing the angular dependent term in the far field region. In Eq. (4.6) $k = 2\pi/\lambda$ is the wave-number, and p - is the spatial spectrum of the pressure distribution on the plane of strips (see Eq. (3.8) in the Section 3.2.) modeling the transducer array illustrated in Fig. 4.1:

$$p(\xi) = p_n(\xi - nK) \equiv p_n(r);\ \xi = r + nK;\ n = \lfloor \xi \rfloor\ ;\ K = 2\pi/P, \tag{4.7}$$

ξ is the spatial spectrum variable related to the x spatial coordinate; $\lfloor \xi \rfloor$ - is the integer floor of ξ; P - is the transducer pitch; $r \in (0, K)$ is an arbitrary spatial wave-number constrained to one Brillouin zone (see Section 3.2., Eq. 3.8):

$$p(x) = \sum_n p_n e^{-j(r+nK)x},\ p_n(r) = \sum_m \alpha_m(r) S_{n-m} P_{n-m}(\cos\Delta), \tag{4.8}$$

where $\Delta = \cos(\pi d/P)$, d - the width of array element; P_n are the Legendre polynomials; $S_n = 1$ for $n \geq 0$ and 0 otherwise. The coefficients α_m (dependent on r) representing the corresponding Bloch components are evaluated from the system of linear equations (see Section 3.2., Eqs. (3.14) and (3.18)):

$$\begin{aligned} &\sum_m \alpha_m \left[j\frac{\eta}{\xi} S_{n-m} - 1 \right] P_{n-m}(\cos\Delta) = 0, \\ &\sum_m (-1)^m \alpha_m P_{-r/K-m}(-\cos\Delta) = j\frac{K}{\pi}\, p_l\, e^{jrlP} \sin \pi r/K, \end{aligned} \tag{4.9}$$

where $p_l = 1$ for $l = 0 \ldots N_t - 1$, and $p_l = 0$ otherwise are given constant pressures of the corresponding active elements (slots in the considered boundary-value problem formulation) which model the N_t-element transmit aperture. In Eq. (4.9) the summation over a finite domain $m \in [-M, M]$ is assumed, M being determined by the BIS-expansion approximation discussed in the Section 3.2. (see Eqs. (3.12) and (3.13), which states in context of Eq. 4.9 that $\eta/\xi = jS_\xi$ for $m > M$ (compare with Eq. (3.3), (3.4)), where η is the spatial spectrum variable related to the z spatial coordinate and is defined as follows (see also Eq. (3.2)):

$$\eta = \sqrt{k^2 - \xi^2} = -j\sqrt{\xi^2 - k^2}. \tag{4.10}$$

Typically, for $k \sim K$ it is sufficient to take several Bloch components p_n into account in the solution for the pressure filed (in the numerical examples shown further $M = 16$ is applied). In the case of a single-element receive aperture to evaluate its directivity function and corresponding apodization weights (see Eq. (4.4)) instead of Eq. (4.5) the above method, Eq. (4.6), can also be exploited in the modified MSTA algorithm, provided $p_l = \delta_{l0}$ is applied in Eq. (4.9), where δ - is the Kronecker delta.

Some computed examples of the directivity function evaluated for different number of active elements and different parameters d/λ and λ/P are shown in Fig. 4.4. Specifically, in Fig. 4.4(a) the case of a single-element aperture is considered for the same operating frequencies as in the example shown in Fig. 4.3. Both methods, Eq. 4.5 and Eq. 4.6, yields similar results. In Fig. 4.4(b) the case of $N_t = 2$ is illustrated.

4.3. Numerical examples

In this Section the developed modified MSTA algorithm is tested using the data obtained by the Field II [69, 96] program for Matlab® and from experimental measurements. To verify the performance of the modified MSTA algorithm

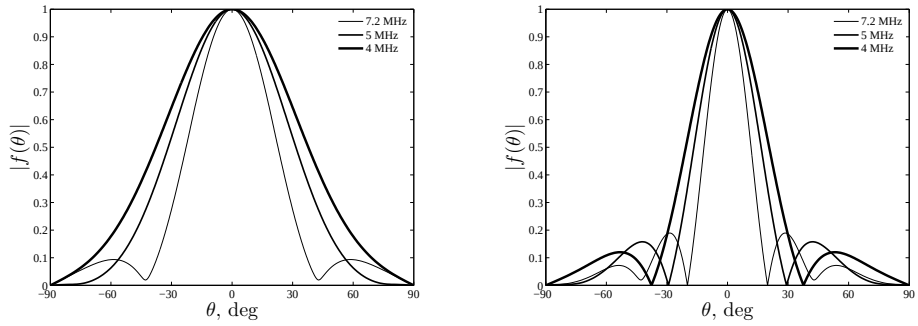

Figure 4.4. Directivity functions for transducer array element with $d = 0.28$ mm for different frequencies $4, 5, 7.2$ MHz corresponding to $d/\lambda = 0.75, 0.94, 1.35$ evaluated using Eq. (4.6); (a) $N_t = 1$, (b) $N_t = 2$

and estimate the lateral resolution and penetration depth as compared to the conventional MSTA method, the synthetic aperture data of a system of point reflectors were simulated for the case of 4 MHz 128-element transducer array with the 0.3 mm pitch and 0.02 mm kerf. The point reflectors were placed in 7 columns, each spaced 4.9 mm apart laterally (this corresponds to 16 transducer pitches). The columns were centered with respect to the transducer middle point for convenience. In each column reflectors were spaced 5 mm axially. Such arrangement of point reflectors, covering entire imaging region, was considered to be convenient for visual assessment of the imaging quality in the whole area. The resulting 2D visualization of point reflectors is shown in Fig. 4.5 over a 60 dB dynamic range.

Considerable improvement of the image quality in the region adjacent to the transducer's aperture can be observed. The blurring artefacts clearly visible in the case of the conventional MSTA algorithm (left subplots in Fig. 4.5(a), and Fig. 4.5(b)) in the vicinity of the first row of point reflectors, are substantially reduced in the case of the modified MSTA algorithm (right subplots). This is clearly observable in Fig. 4.6 and Fig. 4.7 where the lateral cross-section (in logarithmic scale) of the first row of point reflectors and the axial section of the central column are shown, respectively (only 4 first reflectors are visualized for convenience). As seen in Fig. 4.6, the 'noise'-like spatial variations of the scattered signal from the reflectors positioned near the transducer surface are substantially suppressed from approximately -20 dB (MSTA, $N_t = 2$) to -37 dB (modified MSTA, $N_t = 2$), see Fig. 4.6(a), and from -25 dB (MSTA, $N_t = 4$) to -

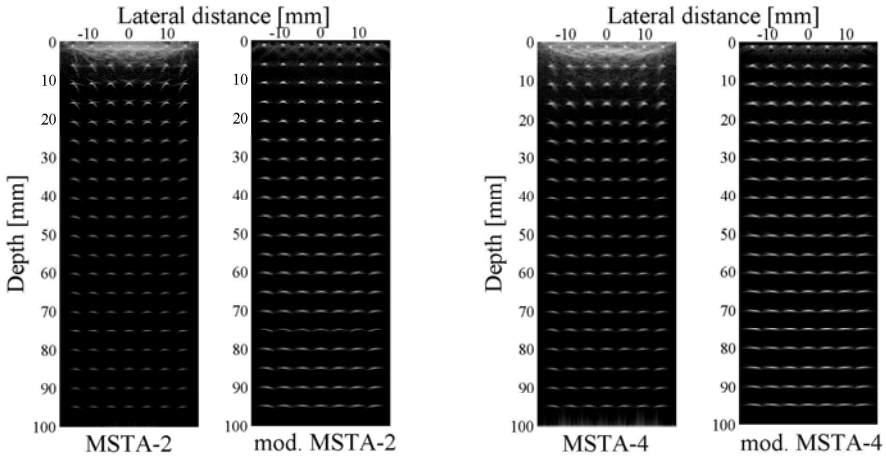

(a) (b)

Figure 4.5. Comparison of the image reconstruction by the conventional (left subplot) and modified (right subplot) MSTA algorithms of the Field II simulated synthetic aperture data for point reflectors and 4 MHz 128-element transducer array with 0.3 mm pitch and 0.02 mm kerf; (a) $N_t = 2$, (b) $N_t = 4$. All images are displayed over 60 dB dynamic range.

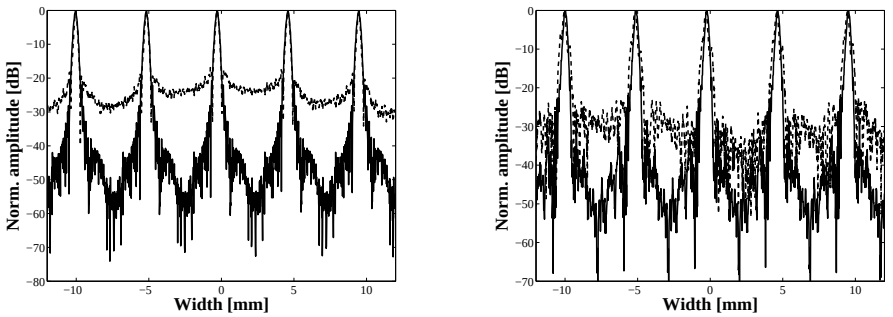

(a) (b)

Figure 4.6. Lateral cross-section of the first row (depth 1 mm) of point reflectors in logarithmic scale; (a) $N_t = 2$, (b) $N_t = 4$; solid lines - modified MSTA algorithm, this work; dashed lines - regular MSTA algorithm.

35 dB (modified MSTA, $N_t = 4$), see Fig. 4.6(b). Also, an increase in penetration depth can be observed in Fig. 4.7 which is further illustrated in Fig. 4.8, where a detailed view of the axial section (central column) showing the maxima of the scattered echo signals as a function of depth is presented. As shown in

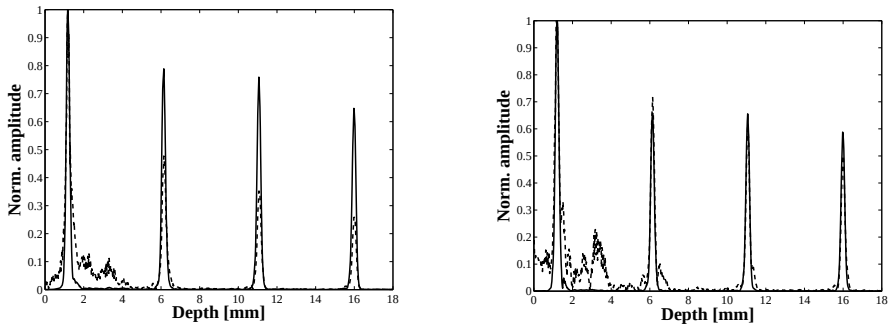

(a) (b)

Figure 4.7. Axial section of the central column of point reflectors: (a) $N_t = 2$, (b) $N_t = 4$; solid lines - modified MSTA algorithm, this work; dashed lines - regular MSTA algorithm.

Fig. 4.8(a) and Fig. 4.8(b) for $N_t = 2$, the scattered echo amplitude obtained using the modified MSTA algorithm is 3.67 and 3.74 times larger than that obtained by means of the conventional one at the depths of 50 and 90 mm, respectively. Similarly, from Fig. 4.8(c) and Fig. 4.8(d) for $N_t = 4$ it is seen that the scattered echo amplitude increases by 1.52 and 1.75 at the same depths if the modified algorithm is used.

In Fig. 4.9 the results related to the lateral resolution are summarized. The lateral cross-sections corresponding to the scattered echo signals of the point reflectors positioned in the central column at the depths of 50 and 90 mm are shown. The cases of $N_t = 2$ and $N_t = 4$ were considered again. As shown in Fig. 4.9(a) through Fig. 4.9(d) for the modified MSTA algorithm the lateral resolution is slightly decreased as compared to the conventional one. It is quantified here by the full width at half maximum (FWHM). Accordingly, at the axial distance of 50 and 90 mm for the conventional MSTA the lateral resolution is 0.88 and 1.06 mm in the case of $N_t = 2$. For $N_t = 4$ the corresponding data are 0.93 and 1.12. In the case of the modified MSTA algorithm at the depths of 50 and 90 mm the lateral resolution is 0.91 and 1.07 mm if the 2-element transmit aperture is used ($N_t = 2$). For $N_t = 4$ the corresponding data are 1.01 and 1.16 mm. These represent 4.16 and 1.21% for $N_t = 2$ along with 8.08 and 3.16 % for $N_t = 4$ decrease in the lateral resolution at the above identified depths. It is worth noting that the decrease in the lateral resolution diminishes with depth.

In Fig. 4.10 the improvements in the image contrast offered by the modified MSTA algorithm are demonstrated. For this purpose the performance of the modified MSTA algorithm was tested using the experimentally obtained syn-

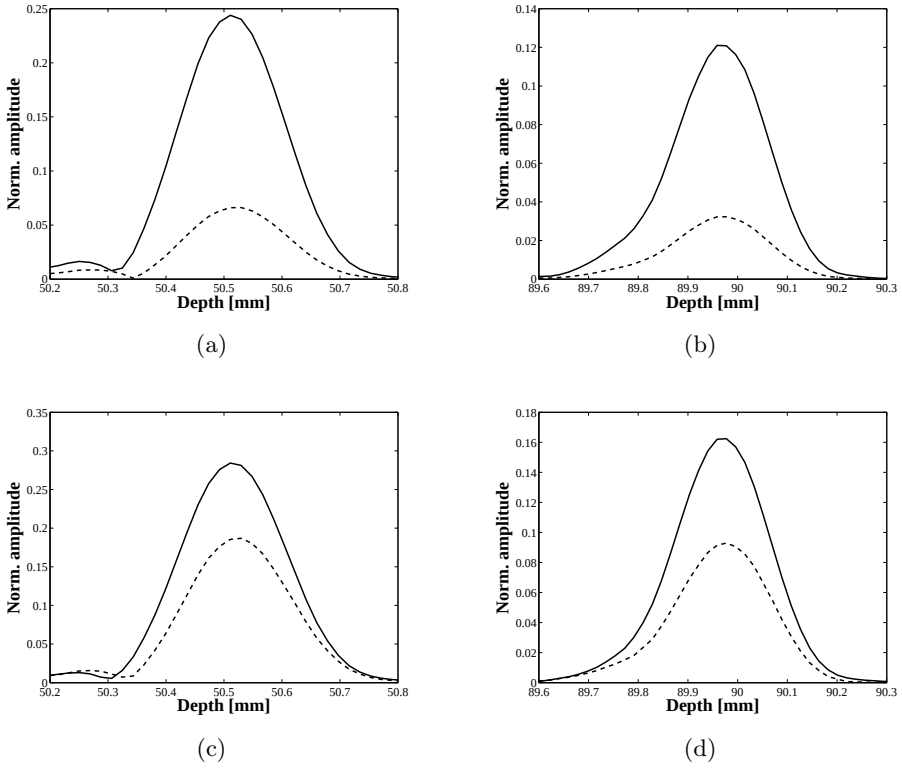

Figure 4.8. Normalized axial section of the image line coinciding with the central column of point reflectors at different depths: (a) 50 mm, $N_t = 2$; (b) 90 mm, $N_t = 2$; (c) 50 mm, $N_t = 4$; (d) 90 mm, $N_t = 4$. Solid lines - modified MSTA algorithm, this work; dashed lines - conventional MSTA algorithm.

thetic aperture data of a cyst phantom (an extra large scan- and elevation-plane tissue mimicking phantom model 57119 Dansk Fantom Service). The measurements were done using the Sonix-TOUCH Research system (Ultrasonix Medical Corporation). The scanner was equipped with a linear transducer model L14-5/38: a 128-element transducer with 0.3 mm element pitch, 0.02 mm kerf and 70% fractional bandwidth was excited by 3 cycles of transducer's center frequency equal 4 MHz. As anticipated (see Section 4.2.), the images presented in Fig. 4.10 show that the modified MSTA algorithm provides a considerable improvement of the image quality in the immediate vicinity of the array's aperture (see Fig. 4.6), as compared to the conventional MSTA. Also, the results shown in Fig. 4.10, demonstrate that the image contrast of the cysts located at the

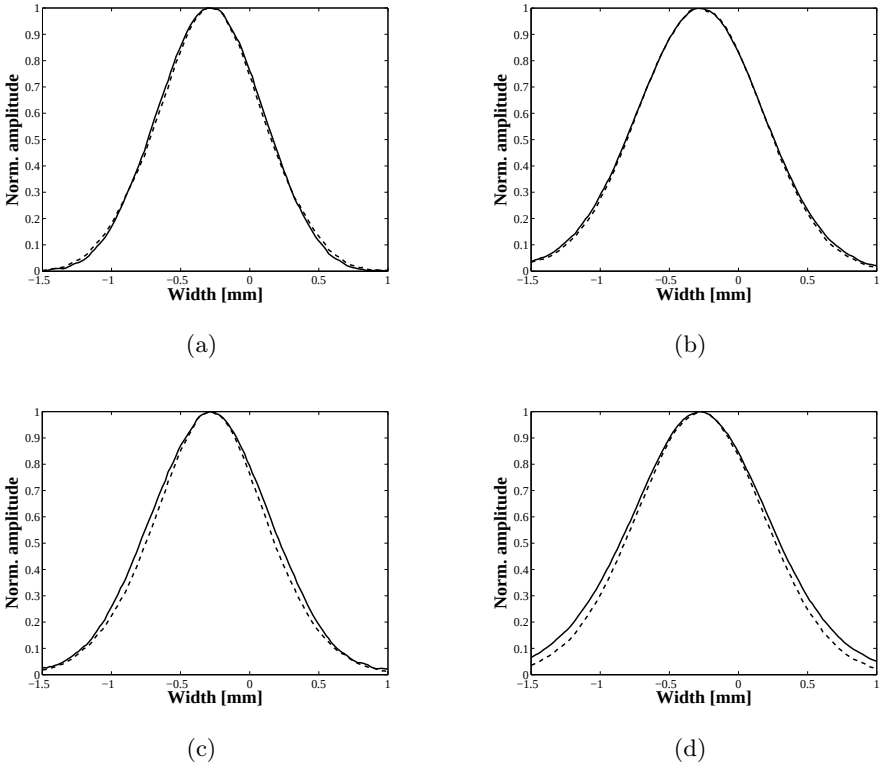

Figure 4.9. Normalized lateral cross-section of the scattered signal corresponding to the point reflectors placed in central column at different depths: (a) 50 mm, $N_t = 2$; (b) 90 mm, $N_t = 2$; (c) 50 mm, $N_t = 4$; (d) 90 mm, $N_t = 4$. Solid lines - modified MSTA algorithm, this work; dashed lines - conventional MSTA algorithm.

axial distance exceeding 40 mm is also slightly improved (visual assessment).

The examples illustrated above confirm that the modified MSTA method presented in this Section allows to achieve considerable improvement of the in the image quality in the region lying in the immediate vicinity of the transducer surface. Also, the hazy blurring artifacts obtained using the conventional MSTA algorithm were substantially suppressed due to the directivity weights applied in the modified MSTA. In addition, an increase in the visualization depth was demonstrated. Concurrently, however, a slight degradation of the lateral resolution was observed, on the other hand this decrease in the lateral resolution decreased with increasing penetration depth. The proposed modification is based on implementation of the apodization weights accounting for the finite trans-

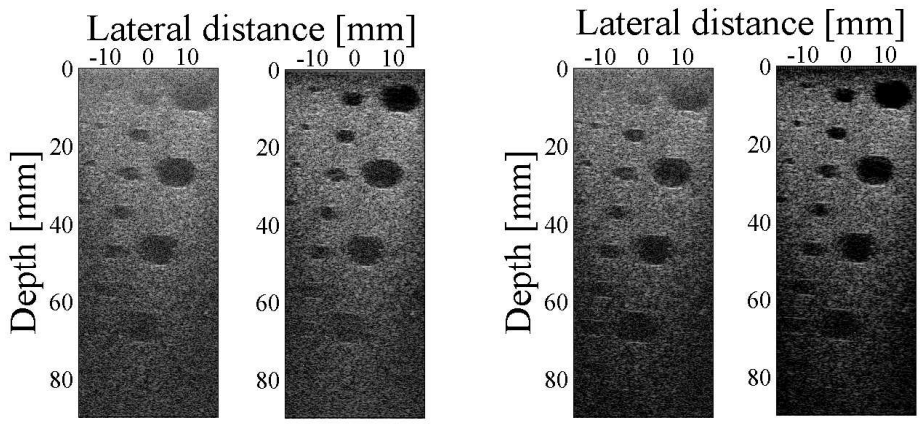

(a) (b)

Figure 4.10. Image reconstruction of the measurement synthetic aperture data for cyst phantom (Dansk Fantom Service, model 571 [97]) and 4 MHz 128-element transducer array with 0.3 mm pitch and 0.02 mm kerf (a) $N_t = 2$, (a) $N_t = 4$. All images are displayed over 40 dB dynamic range. Left subplot - conventional MSTA algorithm; right subplot - modified MSTA algorithm, this work.

mit and receive apertures dimensions. To this end the results of beam-forming analysis presented in the Section 3.2. were successfully exploited.

It should be noted, that the proposed algorithm can be applied to improve the imaging quality in both transmit and receive modes for transmit aperture comprised of up to $16 \div 20$ elements. For larger apertures the increased angular directivity of the transmit aperture leads to stronger spatial filtering in wider range of angles. But, in such cases the apodization weights can be applied in receive mode only, which still yields considerable improvement of the imaging quality as compared to the conventional MSTA algorithm. This is illustrated in Fig. 4.11, where the modified MSTA algorithm is compared both with the conventional one and with the MSTA, having the apodization weights applied only in receiving [93]. Fortunately, in practical realization of the MSTA method not large number of elements in transmit mode is used [83], since there exists a trade-off between penetration depth and the lateral resolution: the former increases and the latter decreases as the number of elements in transmit aperture increases [98].

The inherent advantage of the MSTA method, using several elements in transmit mode, over the STA, using a single element, is that it allows to increase

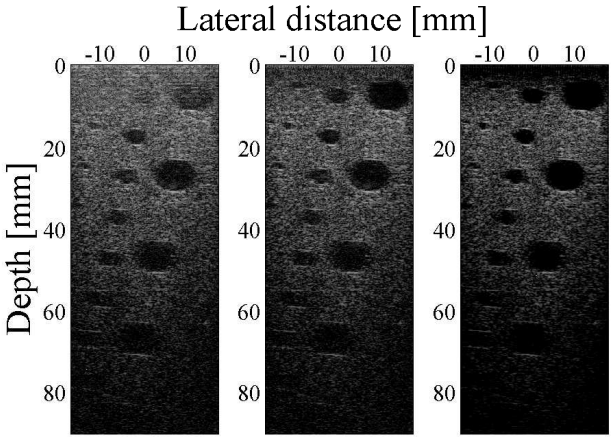

Figure 4.11. Image reconstruction of the measurement synthetic aperture data for cyst phantom (Dansk Fantom Service, model 571 [97]) and 4 MHz 128-element transducer array with 0.3 mm pitch and 0.02 mm kerf; $N_t = 8$. All images are displayed over 40 dB dynamic range. Left subplot - conventional MSTA algorithm; right subplot - modified MSTA algorithm, this work. Left subplot - conventional MSTA algorithm; right subplot - modified MSTA algorithm, this work; central subplot - modified MSTA algorithm with apodization weights applied in receive mode only.

the frame rate, as discussed in the Section 4.2., which means that the processing time can be reduced so it can be performed in such a way that the image is updated at each launching of the probing wave. This promises the modified MSTA method will be well suited to being employed in clinical examinations, especially in the applications where the quality of the "near-field" image, that is the image in the immediate vicinity of the scanhead is of critical importance such as for instance in skin- and breast-examinations.

5

Modeling of 2D periodic structures

In the Chapters 3 and 4 the acoustic beam-forming analysis of the linear transducer arrays was discussed using the methods which are generalized from corresponding spectral approach developed in the electrostatics of planar systems of conducting strips. It appears that the method can be also equally well suited for treatment of 2D acoustic beam-forming structures. This subject is briefly discussed in the current Chapter.

Up-to-date ultrasound probes comprised of hundreds of the elementary transducers can be approximated as a periodic plane arrays and successfully modeled using the method of analysis based on the BIS-expansion (see Section 2.2.1. and 3.2.). In the case of ultrasound imaging (e.g. B-mode) using a linear transducer array the 2D cross-section slices are obtained. Mechanical steering in the elevation direction can be used to combine these cross-sectional slices to achieve volumetric imaging. To accomplish completely electronic focusing and high-speed volumetric scanning the 2D matrix of piezoelectric transducers were developed and implemented recently. Introducing the second dimension in the array of transducers allows to perform electronic steering in elevation (in contrast to the mechanical steering mentioned above in the case of 1D arrays) and reduce the slice thickness, resulting in better volumetric imaging quality and resolution [99, 100]. This offers potentialities for developing of the 3D ultrasound imaging. This new modality overcomes limitations of 2D viewing of 3D anatomy, using conventional ultrasound techniques. In contrast to 2D case, where the sequence of 2D images is transformed by the operator in his mind to obtain the impression of 3D viewing, in 3D ultrasound imaging this activity is performed by the computer. This leads to more efficient and faster examination, diagnostic and monitoring of therapeutic procedures free of potential inaccuracies related to subjective operator dependent treatment. To achieve high imaging quality and faultless work of medical 3D scanners, the corresponding 2D matrix of transducers must be carefully designed including the array fabrication, the electronic integration and the device packaging. And a matter of great importance is developing corresponding analytical and numerical models of 2D array transducers

in order to perform its accurate analysis and performance verification prior to fabrication. Several 2D planar phase-array transducer configurations have been proposed for medical diagnostics [101, 102]. Among them the classical design is the square or matrix architecture [103] (see Fig. 5.1), which is mainly dealt with in this Chapter. The typical geometry of a 2D transducer array is illustrated in Fig. 5.1.

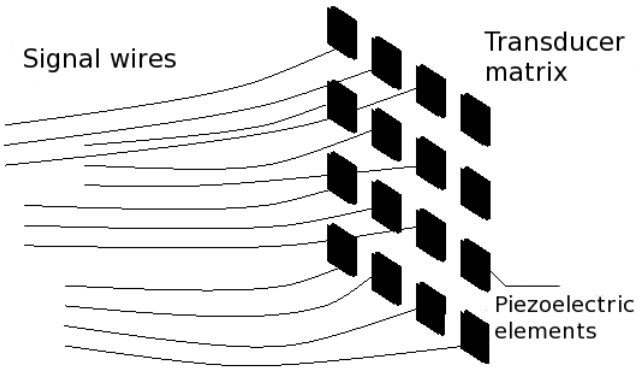

Figure 5.1. Typical 2D square array of piezoelectric transducers with signal wires.

As seen from Fig. 5.1 fabrication of a typical square 2D array transducer requires a large number of signal wires to be connected to individual piezoelectric elements which introduces considerable technological difficulties, such as increased costs and complexity of electronic drive circuits wiring, especially at higher operating frequencies [104]. For instance given 256×256 matrix there are above $65e3$ signal channels with typical dimensions $\sim \lambda/2$ in water so that each 5 MHz array element is 0.15×0.15 mm. To alleviate these problems recently in the literature a novel 2D transducer array architecture has been considered. Namely, a 2D structure of an edge-connected, crossed-electrode array was first considered in [105]. The proposed transducer is capable of control $N \times M$ elements with $N + M$ signal channels. It, however, does not allow to generate arbitrary wave fronts and perform beam-steering in both azimuth and elevation. This problem was partially solved in [106] where a novel approach to generate a 2D ultrasound field using an edge-connected crossed electrode array containing nonlinear transducers such as electrostrictive or electrostatic transducers was proposed. The problem was superficially approached in the signal processing framework without thorough research. However no profound theoretical analysis of the considered crossed-electrode array has been carried out so far.

In this study a generalization of the earlier discussed electrostatic methods

to the problem of 2D periodic structures beam-forming analysis is presented. To this end a 2D ultrasound transducer array comprising crossed periodic metal electrodes placed on both sides of thin dielectric layer exhibiting electrostrictive properties (see Fig. 5.2) is treated in details. The arrangement of strips corresponds to the 2D matrix rows and columns and represents a novel 2D beam-forming and beam-steering approach.

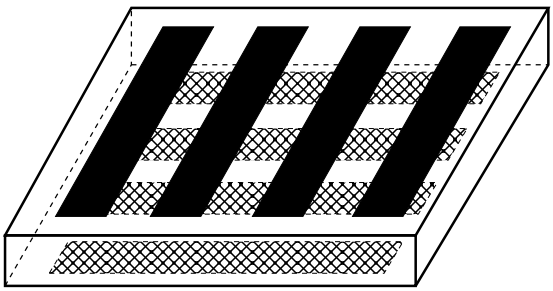

Figure 5.2. System of crossed planar arrays of strips located at the opposite faces of thin electrostrictive dielectric layer.

The system, shown in Fig. 5.2 is capable of electronic beam steering of generated wave both in elevation and azimuth. Perspective application of such a device may be in 3D ultrasound imaging systems. The wave beam control is achieved by addressable driving of the 2D matrix transducer through proper voltage supply of electrodes on opposite surfaces of the electrostrictive layer. Recently electrostrictive materials have been receiving growing attention due to their application as sensors, actuators [107] or transducers [108]. They belong to the class of electroelastic materials exhibiting a quadratic dependence of stress fields upon electric fields. Typically, uniform electric field is applied to entire device, being a plate or membrane made of electroactive polymers and placed between two compliant electrodes, causing its uniform deformation [109]. In this study, however, the case of arbitrary nonuniform electric field distribution yielding nonuniform stress in the plate and its nonuniform vibrations is considered. To evaluated the stress in the layer excited by potentials (voltage) applied to electrodes the formulation of nontrivial electrostatic problem is required. Its solution is based on application of the BIS expansion method (see the Section 2.2.1.) which was used for solving of electrostatic problems discussed in the Section 2.2. and for acoustic beam-forming analysis discussed in the Section 3.2.

Consider a structure containing an electrostrictive dielectric layer with dielectric permittivity ϵ and the systems of parallel conducting strips placed on the opposite surfaces and oriented perpendicularly to each other, as shown in

Fig. 5.3. Let's denote the driving signal applied to the upper and bottom strips

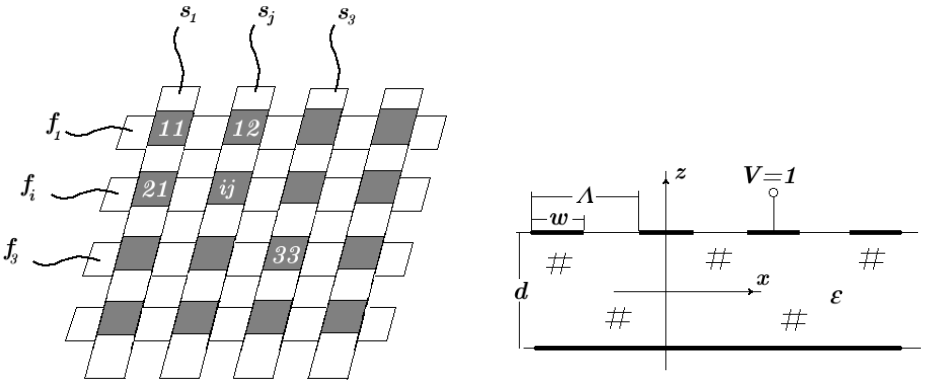

Figure 5.3. Periodic metal strips (electrodes) arranged perpendicularly on both faces of the electrostrictive layer and connected to external voltage sources. (a) Unitary voltage is applied to the upper l^{th} strip residing on a d-thick dielectric layer; other strips are grounded.

as f_i and s_j, respectively, where the i, j are the row and column numbers of the (i, j) matrix cell, located at an intersection of i^{th} upper and j^{th} bottom side strips. For the case of time-harmonic signals:

$$f_i = \cos\omega_i t,\ s_j = \cos(\omega_i + \Omega)t;\ \ \Omega << \omega_l,\ l = i, j, \tag{5.1}$$

the resulting stress in the (i, j)-cell can be approximated as follows [58]:

$$\sigma^{(ij)} = \epsilon \left(\frac{f_i - s_j}{d} \right)^2 \approx 1 - \cos(\omega_i - \omega_j)t - \cos(\omega_i + \omega_j)t + \cdots \tag{5.2}$$

In most applications the high frequency vibrations of the cells can be neglected. This yields the tool for selective (addressable) excitation of given cells: only this cell will vibrate with low frequency Ω, which resides between strips driven by the signals f_i and s_j with frequencies differing by Ω. Thus, applying different amplitudes and phase-shifts to f_i, s_j or frequencies difference Ω, one obtains quite flexible tool for controlling vibrations of cells and the induced stress distribution over entire electrostrictive transducer matrix. The shape of vibrations require detailed analysis of electric field distribution in the layer.

5.1. Generalization of BIS-expansion method

To carry out the theoretical analysis the known results from the theory of surface acoustic waves interdigital transducers or electrostatics of planar periodic system of conducting strips, discussed in details in the Sections 2.2. and 2.2.1. will be used. Namely, the BIS-expansion method will be generalized and applied to the case of the considered 2D periodic array modeling [110, 111]. The electric field defined as $E = -\nabla\varphi$, where φ is electrostatic potential (as in the Section 2.1.), on the plane of strips can be expanded into the Bloch series as follows [110]:

$$\begin{aligned} &\vec{E} = \{E_x, E_y\} = \sum_{n,m} E_{nm} \left\{ \frac{r_n}{k_{nm}}, \frac{s_m}{k_{nm}} \right\} e^{-j(r_n x + s_m y)}, \\ &r_n = r + nK,\ s_m = s + mK,\ k_{nm} = \sqrt{r_n^2 + s_m^2}, \end{aligned} \tag{5.3}$$

where $\Lambda = 2\pi/K$ is strip period; K - is a wavenumber of the strip array; w - is the strip's width; $r \in (0, K)$ and $s \in (0, K)$ are arbitrary spatial spectrum variables reduced to one Brillouin zone for the uniqueness of representation. In Eq. (5.3) E_{nm} can be viewed as the amplitude of the plane harmonic field varying along the axis u, rotated by the angle ϑ with respect to the x axis in the xy-plane:

$$E(u) = E_x \cos\vartheta + E_y \sin\vartheta = E_{nm} e^{-jk_{nm}u},\ \tan\vartheta = s_m/r_n. \tag{5.4}$$

In the above equation E_x and E_y denote the components of the electric field corresponding to (n, m) spatial harmonic. The electrostatic potential appropriate to the Eq. (5.3) can be represented by the following expansion on the plane of strips:

$$\varphi = \sum_{n,m} \frac{E_{nm}}{k_{nm}} e^{-j(r_n x + s_m y)}. \tag{5.5}$$

It should be noted that generally, the tangential component of the electric field on the plane of strips depends on both the x and y spatial coordinates. This is achieved by using a strip model assuming that each strip is a stack of lateral sub-strips, so that the strip potential can vary between sub-strips (but it is constant on the sub-strips). The more detailed discussion can be found for instance in [112]. The normal component of electric induction $D \equiv D_z$ (whose jump discontinuity on the strips plane defines a surface electric charge) can be expanded into a similar series of spatial harmonics as in Eq. (5.3) but with corresponding amplitudes D_{nm}. The boundary conditions on the upper (superscript

u) and bottom (superscript b) surfaces of the dielectric layer imposed on the field components are:

$$\begin{aligned} &E_x^u = 0, \;\; E_y^b = 0, \;\; \text{on strips,} \\ &D^u = 0, \;\; D^b = 0, \;\; \text{between strips.} \end{aligned} \tag{5.6}$$

Applying the BIS-expansion (see Sec. 2.2.1.) the surface fields components satisfying the boundary conditions given by Eq. (5.6) can be expressed in the following manner (compare with Eq. (3.9) and Eqs. (2.15), (2.17)):

$$\begin{aligned} E_x^u &= \sum_{n',n,m} \alpha_{n'}^m S_{n-n'} P_{n-n'}(\cos\Delta) e^{-j(r_n x + s_m y)}, \\ D^u &= \sum_{n',n,m} \tilde{\alpha}_{n'}^m P_{n-n'}(\cos\Delta) e^{-j(r_n x + s_m y)}, \\ E_y^b &= \sum_{m',n,m} \beta_{m'}^n S_{m-m'} P_{m-m'}(\cos\Delta) e^{-j(r_n x + s_m y)}, \\ D^b &= \sum_{m',n,m} \tilde{\beta}_{m'}^n P_{m-m'}(\cos\Delta) e^{-j(r_n x + s_m y)}, \end{aligned} \tag{5.7}$$

where $\Delta = Kw/2$; $P_k(\cdot)$ - is the Legendre polynomials; $S_\nu = 0$ for $\nu < 0$ and $S_\nu = 1$ otherwise. The unknown coefficients $\alpha_{n'}^m$, $\tilde{\alpha}_{n'}^m$ and $\beta_{m'}^n$, $\tilde{\beta}_{m'}^n$ can be evaluated using the relation between spatial spectra of the tangential electric field $E^{u,b}$ and normal electric induction $D^{u,b}$ on the upper and bottom surfaces of the dielectric layer, which governs the field inside the layer [110]:

$$\begin{bmatrix} E^u \\ E^b \end{bmatrix} = \frac{S_k}{j\epsilon} \begin{bmatrix} \coth|k|d & -1/\sinh|k|d \\ 1/\sinh|k|d & -\coth|k|d \end{bmatrix} \begin{bmatrix} D^u \\ D^b \end{bmatrix}. \tag{5.8}$$

The above relation directly results from the solution of the Laplace equation $\Delta\varphi = 0$ inside the dielectric layer, where the electric potential $\varphi(z)$ can be expressed in the following form:

$$\varphi(u,z) = \left[Ae^{-|k|z} + Be^{|k|z} \right] e^{-jku}, \;\; |z| < d/2. \tag{5.9}$$

In the above equation u is defined for the (n,m) component in Eq. (5.4). Evaluating the field components E_u, D_z:

$$\begin{aligned} E_u(u,z) &= jk \left[Ae^{-|k|z} + Be^{|k|z} \right] e^{-jku}, \\ D_z(u,z) &= \epsilon|k| \left[Ae^{-|k|z} - Be^{|k|z} \right] e^{-jku}, \end{aligned} \tag{5.10}$$

and eliminating the constants A, B from the above using the surface field $E^{u,b} = E_u \pm d/2$, $D^{u,b} = D_z \pm d/2$ one readily obtains Eq. (5.8). It plays here a similar role as the plane harmonic Green's function defined for a half-plane by Eq. (2.3) in the Section 2.1. or the surface harmonic admittance of acoustic half-space, defined by Eq. (3.3) in the Section 3.1. Namely, the field expansion given by Eqs. (5.7) must obey Eq. (5.8) for any Bloch component having wave-numbers $k = k_{nm}$ included in the expansion. It is worth noting, that the higher Bloch orders vanish fast inside the layer and are negligible on its opposite surface due to the term $1/(\sinh k_{nm}d)$. Thus, for large k_{nm} the corresponding spatial harmonics are well-localized at a given dielectric surface. This significantly simplifies the analysis due to the equations separation for large k_{nm}. The Bloch components from Eq. (5.7) must obey Eq. (5.10) for any numbers (n, m). Particularly, for (n, m) sufficiently large, such that $\coth|k_{NM}|d = 1$, $1/\sinh|k_{NM}|d = 0$ and $r_N/k_{NM} = 1$ for the upper and $s_M/k_{NM} = 1$ for the bottom surface field representations, where N, M some large but finite integers (see Sec. 3.2. and discussion further in this Section), a similar approximation as in Eq. (3.13) can be applied:

$$\tilde{\alpha}^m_{n'} = j\epsilon\alpha^m_{n'}; \quad \tilde{\beta}^n_{m'} = -j\epsilon\beta^n_{m'}. \tag{5.11}$$

Substituting the above equation into Eq. (5.7) yields:

$$\begin{aligned}
E^u_x &= \sum_{n',n,m} \alpha^m_{n'} S_{n-n'} P_{n-n'}(\cos\Delta) e^{-j(r_n x + s_m y)}, \\
D^u &= j\epsilon \sum_{n',n,m} \alpha^m_{n'} P_{n-n'}(\cos\Delta) e^{-j(r_n x + s_m y)}, \\
E^b_y &= \sum_{m',n,m} \beta^n_{m'} S_{m-m'} P_{m-m'}(\cos\Delta) e^{-j(r_n x + s_m y)}, \\
D^b &= -j\epsilon \sum_{m',n,m} \beta^n_{m'} P_{m-m'}(\cos\Delta) e^{-j(r_n x + s_m y)},
\end{aligned} \tag{5.12}$$

Substitution of the Bloch components having the same wave-number k_{nm} from Eqs. (5.12) into Eqs. (5.8) for $n \in [-N, N]$, $m \in [-M, M]$ yields the system of linear equations for the unknown coefficients $\alpha^m_{n'}$ and $\beta^n_{m'}$, $m' \in [-M, M]$ and $n' \in [-N, N]$:

$$\begin{aligned}
&\alpha^m_{n'} \left[S_{n-n'} \tanh k_{nm}d - \frac{r_n}{k_{nm}} \right] P_{n-n'} - \beta^n_{m'} \frac{r_n}{k_{nm}} \frac{P_{m-m'}}{\cosh k_{nm}d} = 0, \\
&-\alpha^m_{n'} \frac{s_m}{k_{nm}} \frac{P_{n-n'}}{\cosh k_{nm}d} + \beta^n_{m'} \left[S_{m-m'} \tanh k_{nm}d - \frac{s_m}{k_{nm}} \right] P_{m-m'} = 0.
\end{aligned} \tag{5.13}$$

In Eq. (5.13) $P_l = P_l(\cos\Delta)$ is applied to shorten notation. Due to the conditions leading to the approximation in Eq. (5.11) the equations for $\alpha^m_{n'}$ and $\beta^n_{m'}$ given by Eq. (5.13) outside the limits $n \in [-N, N]$, $m \in [-M, M]$ are satisfied directly, what can be checked by inspection (see discussion in Sec. 2.2.1., Eqs. (2.52–2.57) and in Sec. 3.2., Eq. (3.14)). The number of equations in Eq. 5.13 can be further reduced for the considered case of $s = 0$ exploiting the symmetry properties of the unknown coefficients $\beta^n_{m'}$. Namely, substituting the identities involving the Legendre polynomials [64]:

$$P_{-1-\nu}(\cos\Delta) = P_\nu(\cos\Delta); \quad P_l(-\cos\Delta) = (-1)^l S_l P_l(\cos\Delta), \tag{5.14}$$

into Eq. 5.13 yields:

$$\beta^n_{m'}(r) = \beta^n_{1-m'}(r), \tag{5.15}$$

where the dependence of the coefficients on r is shown explicitly. Taking into account Eq. (5.15) the equations in Eq. (5.13) can be transform for $0 \le m, m' \le M$, with $-N \le n, n' \le N$ as follows:

$$\begin{aligned}
&\alpha^m_{n'}\left[S_{n-n'}\tanh k_{nm}d - \frac{r_n}{k_{nm}}\right]P_{n-n'} - \beta^n_{m'}\frac{r_n}{k_{nm}}\frac{P_{m-m'} - P_{-m-m'}}{\cosh k_{nm}d} = 0,\\
&\alpha^m_{n'}\frac{s_m}{k_{nm}}\frac{P_{n-n'}}{\cosh k_{nm}d} - \beta^n_{m'}\sum_{l=-m,m}\left[S_{l-m'}\tanh k_{nm}d - \frac{s_m}{k_{nm}}\right]P_{l-m'} = 0.
\end{aligned} \tag{5.16}$$

In Eq. (5.16) the last equation for $m = 0$ should be replaced with the following:

$$\frac{P_{n-n'}}{\cosh k_d}\alpha^0_{n'} - 2\left[(-1)^{m'}\frac{k}{K}\tanh kd\frac{d}{d\xi}\,P_{-m'+\xi}\big|_{\xi=0} - P_{-m'}\right]\beta^n_{m'} = 0, \tag{5.17}$$

where $k = k_{n0}$. The truncation numbers M, N involved in the system of linear equations, Eq. (5.16) and Eq. (5.17), generally, should be infinite, but practically it is sufficient to apply N, M not very large finite integers. Let N', M' be such that

$$\tanh N'Kd \approx \tanh N'Kd \approx 1, \tag{5.18}$$

then $N > N'$ and $M > M'$ should be chosen such that $r_N/k_{NM'} \approx 1$ and $s_M/k_{N'M} \approx 1$, respectively (see Eq. (5.11) and the foregoing discussion).

Integrating corresponding tangential components of the electric field (see Eq. (2.58) in Sec. 2.2.1.) one obtains the potential distribution on the plane of strips on the upper and bottom sides (which assumed to be given in the considered boundary-value problem as additional constrains to determine unknown expansion coefficients uniquely). Following the same considerations as in the

Section 2.2.1. when deriving Eq. (2.62) (see Eqs. (2.58) through (2.62)), for the case, shown in Fig. 5.3(b), where the unitary voltage is applied to l^{th} upper strip and all the bottom strips assumed to be grounded ($s = 0,\ s_m = mK$ in this case) this condition results in (see also derivation of Eq. (3.18) in Sec. 3.2.):

$$(-1)^{n'}\alpha_{n'}^{m}P_{-n'-r/K}(-\cos\Delta) = \delta_{m0}\frac{K}{\pi}e^{jrl\Lambda}\sin\pi r/K, \tag{5.19}$$

where δ_{ij} - is the Kronecker delta. Solving Eqs. (5.16), (5.17) and Eq. (5.19) for $\alpha_{n'}^{m}$ and $\beta_{m'}^{n}$ the planar electric field can be determined on both surfaces of dielectric layer from Eq. (5.12).

5.2. Induced electrostrictive stress in the dielectric layer

According to Eq. (5.2), the electrostrictive stress in the layer $\sigma^{(ij)}$ or, more exactly, its z-component, considered here, is proportional to the product of normal component $E_z(x, y)$ of the electric field vector, resulting from the applied potential to the upper i^{th} electrode and $E_z(x, y)$ excited by the bottom j^{th} electrode. In the considered case of the same strip periodicity and width on both upper and bottom sides of the layer, the latter equals to the $E_z(y, x)$ on the upper face of the layer. It is known [113, 114] that the electric field is singular at the strip edges. In order to avoid the corresponding difficulty, the E_z components of electric field at the layer middle plane $z = 0$ are evaluated. It can be reconstructed from the surface normal induction D_z on both surfaces of the layer given by Eq. (5.12). In general case the electric field representation on both surfaces of the dielectric layer, Eq. (5.12), are defined for any $\varrho = r + nK$ and $\tau = s + mK$, being the spectral variables corresponding to the x and y spatial coordinates. Therefore, Eqs. (5.12) can be considered as the 2D Fourier transforms of the corresponding spatial distributions of the electric field components on the planes of strips. Thus, using the spatial spectra of the normal induction on the upper D^u and bottom D^b faces of the dielectric layer, Eq. (5.12), the normal induction on the plane $z = 0$, resulting directly from Eq. (5.10) (the constants A, B being expressed in terms of D^u, D^b), is:

$$D_z = \frac{D^u + D^b}{2\cosh|k|d/2},\quad k = k_{mn} = \sqrt{\varrho^2 + \tau^2}. \tag{5.20}$$

In the particular case considered here ($s = 0$) the function in Eq. (5.20) is defined in the spectral domain of continuous variable $\varrho = r + nK$ and discrete

$\tau = mK$ and the corresponding spatial counterpart can be found by the inverse 2D Fourier transform. Using the relation $E_z = D_z/\epsilon$ one finally obtains:

$$E_z(x,y) = \frac{2j}{K}\int_{-\infty}^{\infty} e^{-j\varrho x}d\varrho \times \sum_{m=-\infty}^{\infty} \frac{\alpha_{n'}^m P_{n-n'}(\cos\Delta) - \beta_{m'}^n P_{m-m'}(\cos\Delta)}{\cosh(k_{nm}d/2)} e^{-jmKy}. \tag{5.21}$$

Fast growing term $1/(\cosh k_{nm}d/2)$ makes the above equation suitable for numerical evaluation.

In Fig. 5.4 the numerical example of the σ_z component of the electrostrictive stress in the layer middle plane $z = 0$ is shown in relative scale for $w/\Lambda = 0.6$ and different thickness of the dielectric layer. As is seen from Fig. 5.4, the stress distribution at the middle plane of the dielectric layer significantly departs from uniform and spans somewhat outside the cell covered by the supplied strips.

Summarizing, the extension of the BIS-expansion method, originally developed for electrostatic analysis of 1D periodic planar systems of strips, was presented in this Section for modeling of 2D periodic structure comprised of crossed arrays of strips placed on the opposite surfaces of the thin dielectric electrostrictive layer. It is an example of novel architecture of 2D transducer with potential application in 3D ultrasound imaging. Numerical examples show the resulting nonuniform electrostrictive stress induced in the area of the excited matrix cell for one upper strip excited by a uniform voltage and all bottom strips grounded. The method is of great importance for analysis of more general cases, like, double periodic structures comprised of crossed arrays of strips placed on piezoelectric plate and arbitrary voltage supply. This case is being developed and the promising results are being expected.

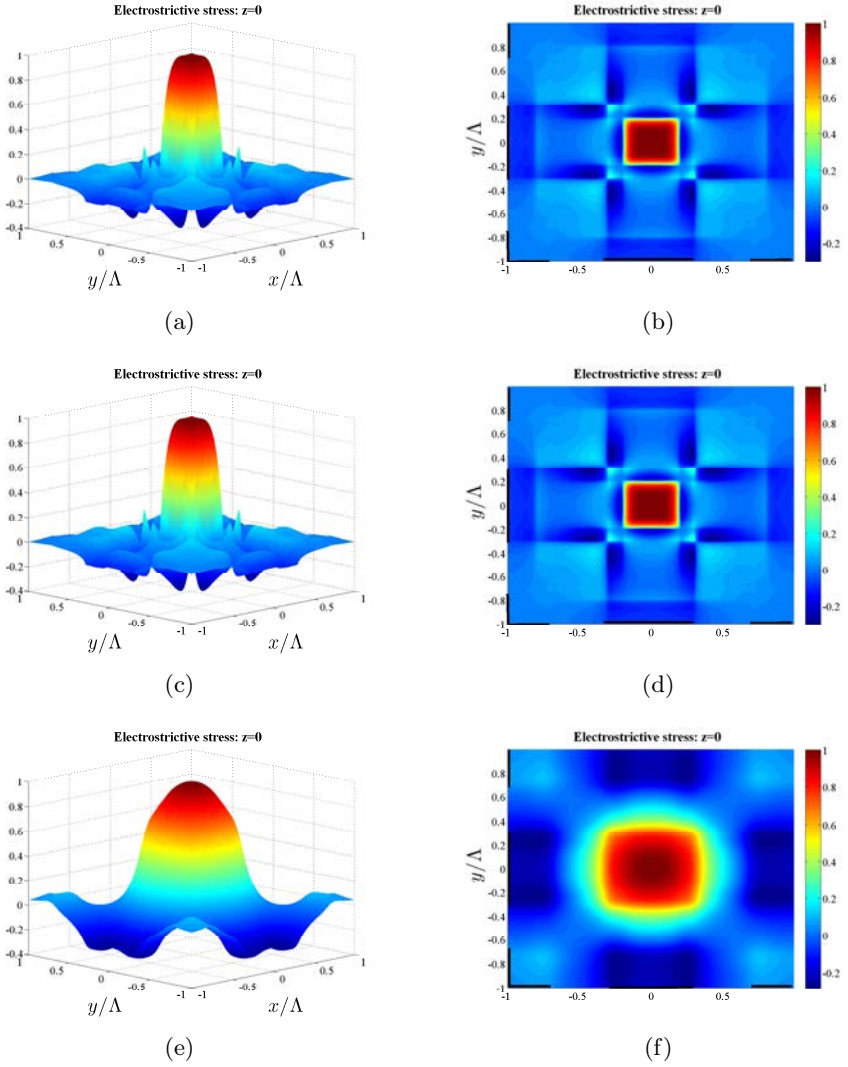

Figure 5.4. The electrostrictive stress generated in the $2\Lambda \times 2\Lambda$ domain of the dielectric layer at the plane $z = 0$ for $w/\Lambda = 0.6$ and different plate thickness: (a), (b) - $d/\Lambda = 0.15$; (c), (d) - $d/\Lambda = 0.5$; (e), (f) - $d/\Lambda = 1$.

6

Other applications

In the previous Chapters of this study the electrostatic methods of analysis of planar system of conducting strips (see Chapter 2) were generalized for acoustic beam-forming applications using the linear phased-array transducers (see Chapters 3, 4). Both the BIS-expansion and the template function approaches (see Sections 2.2.1. and 2.3., respectively) were exploited for the solution of the corresponding boundary-value problem for baffle array, discussed in details in the Chapter 3. Also an extension for the case of 2D acoustic beam-forming structures was presented in the Chapter 5, where the novel geometry of matrix transducer composed of the crossed arrays of strips was considered. To this end a generalization of the BIS-expansion method to the analysis of 2D periodic structures was discussed. As already mentioned in the Chapter 1, the range of physical problems which can be analyzed by the methods of electrostatic spectral theory, discussed in details in the Chapter 2, is not restricted to the acoustic waves only. In particular, the problems of elastic wave scattering by periodic cracks [36] and electromagnetic wave scattering by a planar periodic system of perfectly conducting strips [35] were successfully approached by the BIS-expansion method. Recently, it was further generalized for analysis of non-planar periodic structures [42–44] in the theory of electromagnetic wave scattering. Also a theoretical study of the planar system of strips with broken periodicity (to be defined in Sec. 6.2.) in electrostatic applications was conducted. In this Chapter the above extensions of the electrostatic method based on the BIS-expansion will be discussed to show its flexibility and versatility. In the Section 6.1. the scattering of electromagnetic waves by periodic thick-walled parallel-plate waveguide array and by the system of thick conducting electrodes will be considered following [43] and [44], respectively. And, finally, in the Section 6.2. electrostatic analysis for the planar system of strips with broken periodicity (quasi-periodic system) will be presented [57].

6.1. Electromagnetic wave scattering by non-planar periodic structures

Electromagnetic scattering and radiation by periodic systems is a significant and important problem of the diffraction theory which is still of current importance from the theoretical and practical points of view. Different systems and methods are described in the literature. In the practical aspect the perfectly electric conducting (PEC) periodic structures can simulate the phased arrays in micro an millimeter wave applications, such as filters [45, 46], frequency selective structures [47, 48], splitters and antennas [49, 50], widely used in today's communication and radar systems [51, 52]. From the theoretical point of view it gives a deeper insight into the study of periodic structures. Recently, periodic systems with a particular arrangement of scatterers including conductors and dielectrics has received growing attention, because such the systems may behave like negative refractive index materials [53, 54, 115] within a certain frequency range. Many approaches [55, 56, 116, 117] have been proposed to analyze them, such as the mode-matching method, finite difference time domain (FDTD) technique, finite element method (FEM), and Fourier series method. In this Section the problems of plane wave scattering by a periodic array of thick-walled parallel-plate waveguides and by a periodic system of conducting electrodes of finite thickness will be considered.

6.1.1. Plane wave scattering by a thick-walled parallel-plate waveguide array

The scattering of electromagnetic waves by a parallel-plate waveguide array is a classical problem of diffraction theory and has been investigated by many authors [118–123]. Exact closed-form solutions has been obtained only in few cases of waveguides with infinitesimally thin walls [124], [61]. In the case of thick waveguide walls different methods from Wiener-Hopf [118] and variational technique [119] to purely numerical treatment of integral equation [120] and finite-element time-domain method [121] were used to obtain an approximate solution.

Here the problem of plane wave scattering by an array of parallel-plate waveguides with thick walls for oblique incidence will be approached using a method discussed earlier in the Sections 2.2.1. and 3.2. which exploits a similar field representation as in the case of the BIS-expansion method and, therefore, can be referred as its generalization to the case of analysis of non-planar structures. Specifically, the scattered field is sought in the form of spatial harmonics in the space above the array and in the form of parallel plate waveguide modes

in the waveguide regions. The presented method is based on application of a Fourier series expansion for representation of the spatial harmonics amplitudes in free space above the waveguides. The corresponding coefficients are properly chosen Legendre functions, similarly as in the BIS-expansion method studied in earlier Sections. This helps one to satisfy the boundary and edge conditions directly by field representation. Similarly as in [42] a problem is reduced to numerical solving of certain system of linear equations with coefficients given by explicit formula.

Consider an infinite system of perfectly conducting thick-walled parallel-plate waveguides shown in Fig. 6.1. The period of the structure is Λ and the

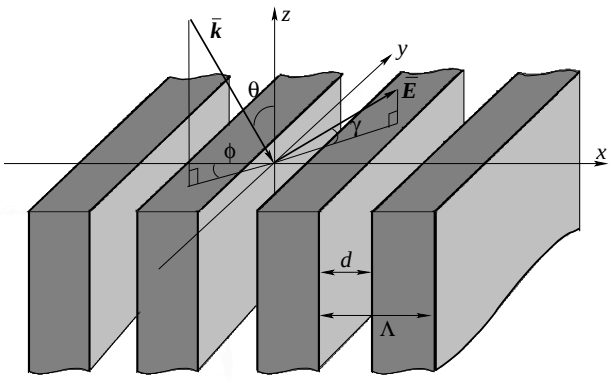

Figure 6.1. Thick-walled parallel-plate waveguide array

waveguide aperture is d. The system is homogeneous in the direction of the y-axis, and direction of periodicity is along the x-axis. Waveguides occupy the lower half-plane $z < 0$. An incident plane harmonic wave of angular frequency ω impinges on the system at the angle θ counted from the z-axis in the plane rotated with respect to the plane $y = 0$ by the angle ϕ, counted from the x-axis as shown in Fig. 6.1. In what follows, the term $e^{j\omega t}$ will be omitted. The total field can be represented in the form:

$$\begin{aligned} \{\vec{E}^+, \vec{H}^+\} &= \{\vec{E}^{s+}, \vec{H}^{s+}\} + \{\vec{E}^I, \vec{H}^I\}, \quad z > 0, \\ \{\vec{E}^-, \vec{H}^-\} &= \{\vec{E}^{s-}, \vec{H}^{s-}\}, \quad z < 0, \end{aligned} \tag{6.1}$$

where the superscripts $+,-$ denote the field components above the waveguides ($z > 0$) and in the waveguides ($z < 0$), respectively. The superscripts s and I

denote the scattered field and given field of the incident wave, respectively. The components of the electric and magnetic field vectors can be written in terms of the Hertz electric and magnetic potentials $\vec{n}_z\Phi$ and $\vec{n}_z\Psi$ [29] (except for the case of normal incidence along the z-axis which is not considered here) as follows:

$$\begin{aligned}\vec{E} &= -j\omega\mu_0\nabla\times\vec{n}_z\Psi + \nabla\nabla\cdot\vec{n}_z\Phi + k_0^2\vec{n}_z\Phi,\\ \vec{H} &= \nabla\nabla\cdot\vec{n}_z\Psi + k_0^2\vec{n}_z\Psi + j\omega\epsilon_0\nabla\times\vec{n}_z\Phi,\end{aligned} \tag{6.2}$$

where ϵ_0 and μ_0 are dielectric permittivity and magnetic permeability of free space, respectively; $k=\omega(\epsilon_0\mu_0)^{1/2}$ is the wave number of plane incident wave; $\vec{n}_z$ is a unity vector along the z-axis. The Hertz potentials of the incident wave field are assumed in the form:

$$\begin{aligned}&\Phi^I e^{-j(k_x x+k_y y-k_z z)},\ \Psi^I e^{-j(k_x x+k_y y-k_z z)},\ k^2=k_x^2+k_y^2+k_z^2,\\ &k_x=k\sin\theta\cos\varphi,\ k_y=k\sin\theta\sin\varphi,\ k_z=k\cos\theta,\end{aligned} \tag{6.3}$$

with corresponding amplitudes Φ^I and Ψ^I. According to the Floquet's theorem in the upper half-space $z>0$ the solution for Φ and Ψ is tried in the form of a linear combination of spatial harmonics:

$$\psi_n = e^{-j(k_{xn}^+ x+k_y y+k_{zn}^+ z)},\ k^2=k_{xn}^{+2}+k_y^2+k_{zn}^{+2},\ k_{xn}^+=k_x+nK,$$

$$k_{zn}^+ = \begin{cases}(k^2-k_{xn}^{+2}-k_y^2)^{1/2}, & k^2\geq k_{xn}^{+2}+k_y^2,\\ -j(k_{xn}^{+2}+k_y^2-k^2)^{1/2}, & k^2<k_{xn}^{+2}+k_y^2,\end{cases} \tag{6.4}$$

$$K=2\pi/\Lambda$$

with amplitudes Φ_n^+ and Ψ_n^+. Substituting Eq. (6.3) and Eq. (6.4) into Eq. (6.2) the expressions for the spatial harmonics of the total electric and magnetic field components in the upper half-space can be deduced:

$$\begin{aligned}E_{xn}^+ &= \left(\omega\mu_0 k_y\tilde{\Psi}_n^+ + k_{xn}^+ k_{zn}^+\tilde{\Phi}_n^-\right)\psi_n,\\ E_{yn}^+ &= \left(-\omega\mu_0 k_{xn}^+\tilde{\Psi}_n^+ + k_{zn}^+ k_y\tilde{\Phi}_n^-\right)\psi_n,\\ E_{zn}^+ &= (k^2-k_{zn}^{+2})\tilde{\Phi}_n^+\psi_n,\\ H_{xn}^+ &= \left(-\omega\epsilon_0 k_y\tilde{\Phi}_n^+ + k_{xn}^+ k_{zn}^+\tilde{\Psi}_n^-\right)\psi_n,\\ H_{yn}^+ &= \left(\omega\epsilon_0 k_{xn}^+\tilde{\Phi}_n^+ + k_{zn}^+ k_y\tilde{\Psi}_n^-\right)\psi_n,\\ H_{zn}^+ &= (k^2-k_{zn}^{+2})\tilde{\Psi}_n^+\psi_n,\end{aligned} \tag{6.5}$$

with new amplitudes $\tilde{\Phi}_n^{\pm}$, $\tilde{\Psi}_n^{\pm}$ defined as follows:

$$\begin{aligned}
&\tilde{\Phi}_n^{+} = \delta_{n0}\Phi^I + \Phi_n^{+},\ \tilde{\Phi}_n^{-} = \delta_{n0}\Phi^I - \Phi_n^{+},\\
&\tilde{\Psi}_n^{+} = \delta_{n0}\Psi^I + \Psi_n^{+},\ \tilde{\Psi}_n^{-} = \delta_{n0}\Psi^I - \Psi_n^{+}.
\end{aligned} \tag{6.6}$$

In Eq. (6.6) δ_{n0} is Kronecker delta; $n \in \mathbb{Z}$. In the lower half-space $z < 0$ the solution for the electric and magnetic Hertz potentials is sought in the form of linear combination of parallel plate waveguide modes given below for one period of the structure $-d/2 \le x \le d/2$:

$$\begin{aligned}
&\Phi_p^{-}\psi_p^{\mathrm{s}}:\ \psi_p^{\mathrm{s}} = \sin\big(k_{xp}^{-}\,(x+d/2)\big)\,e^{-j(k_y y - k_{zp}^{-} z)},\ p\in\mathbb{N},\\
&\Psi_p^{-}\psi_p^{\mathrm{c}}:\ \psi_p^{\mathrm{c}} = \cos\big(k_{xp}^{-}\,(x+d/2)\big)\,e^{-j(k_y y - k_{zp}^{-} z)},\ p\in\mathbb{N}\cup 0,\\
&k^2 = k_{xp}^{-\,2} + k_y^2 + k_{zp}^{-\,2},\ k_{xp}^{-} = p\pi/d,\\
&k_{zp}^{-} = \begin{cases} (k^2 - k_{xp}^{-\,2} - k_y^2)^{1/2}, & k^2 \ge k_{xp}^{-\,2} + k_y^2,\\ -j(k_{xp}^{-\,2} + k_y^2 - k^2)^{1/2}, & k^2 < k_{xp}^{-\,2} + k_y^2, \end{cases}
\end{aligned} \tag{6.7}$$

with amplitudes Φ_p^{-}, Ψ_p^{-}. The partial wave amplitudes in the l^{th} period, $-d/2+l\Lambda < x < d/2+l\Lambda$, are as follows:

$$\begin{aligned}
&\Phi_p^{(l)-} = \Phi_p^{-}\exp(-jk_x l\Lambda),\ l\in\mathbb{Z},\ p\in\mathbb{N},\\
&\Psi_p^{(l)-} = \Psi_p^{-}\exp(-jk_x l\Lambda),\ l\in\mathbb{Z},\ p\in\mathbb{N}\cup 0.
\end{aligned} \tag{6.8}$$

Substituting Eq. (6.7) into Eq. (6.2) the following expressions for the partial waves representing the total electric and magnetic field components in the waveguides can be written:

$$\begin{aligned}
E_{xp}^{-} &= \big(jk_{xp}^{-}k_{zp}^{-}\Phi_p^{-}(1-\delta_{p0}) + \omega\mu_0 k_z\Psi_p^{-}\big)\,\psi_p^{\mathrm{c}},\\
E_{yp}^{-} &= \big(k_y k_{zp}^{-}\Phi_p^{-} + j\omega\mu_0 k_{xp}^{-}\Psi_p^{-}\big)\,(1-\delta_{p0})\psi_p^{\mathrm{s}},\\
E_{zp}^{-} &= \big(k^2 - k_{zp}^{-\,2}\big)\,\Phi_p^{-}(1-\delta_{p0})\psi_p^{\mathrm{s}},\\
H_{xp}^{-} &= -\big(jk_{xp}^{-}k_{zp}^{-}\Psi_p^{-} + \omega\epsilon_0 k_y\Phi_p^{-}\big)\,(1-\delta_{p0})\psi_p^{\mathrm{s}},\\
H_{yp}^{-} &= \big(k_y k_{zp}^{-}\Psi_p^{-} + j\omega\epsilon_0 k_{xp}^{-}\Phi_p^{-}(1-\delta_{p0})\big)\,\psi_p^{\mathrm{c}},\\
H_{zp}^{-} &= \big(k^2 - k_{zp}^{-\,2}\big)\,\Psi_p^{-}\psi_p^{\mathrm{c}},
\end{aligned} \tag{6.9}$$

where $p \in \mathbb{N} \cup 0$ and the arguments of ψ_p^{s} and ψ_p^{c} has been dropped to shorten notation. The tangential electric field must vanish on the surface of perfectly conducting waveguide walls yielding the following boundary conditions:

$$\begin{aligned} &E_x = 0;\ E_y = 0;\ d/2 < |x| < \Lambda/2,\ z = +0 \\ &E_y = 0;\ E_z = 0;\ x = \pm d/2,\ z < 0. \end{aligned} \tag{6.10}$$

Besides, near the edges of the waveguides walls the tangential field components exhibit singular behavior [61]:

$$\begin{aligned} &E_i = O(\rho^{-1/3}),\ H_i = O(\rho^{-1/3}),\ i = x, z, \\ &\rho \to 0, \rho = \left((x \pm d/2)^2 + z^2\right)^{1/2}. \end{aligned} \tag{6.11}$$

The tangential field components must obey a continuity condition across the apertures of the waveguides on the plane $z = 0$:

$$E_i^+ = E_i^-,\ H_i^+ = H_i^-,\ -d/2 < x < d/2,\ z = 0,\ i = x, z. \tag{6.12}$$

Next, the mode matching technique is applied to deduce a system of equations for unknown amplitudes $\tilde{\Phi}_n^{\pm}$, $\tilde{\Psi}_n^{\pm}$ defined in Eq. (6.6). Namely, the expressions for the field components in the upper and lower half-spaces given by Eq. (6.5) and Eq. (6.9) are substituted into Eq. (6.12) first. Then, multiplying by $\cos(k_{xl}^-(x + d/2))$ and $\sin(k_{xl}^-(x + d/2))$ ($l \in \mathbb{Z}$) of the continuity conditions, Eq. (6.12), for E_x, H_y and E_y, H_x, respectively, and integrating with respect to x from $-d/2$ to $d/2$ one obtains for E_x, H_y:

$$\begin{aligned} &\left(jk_{xp}^- k_{zp}^- \Phi_p^- (1 - \delta_{p0}) + \omega\mu_0 k_y \Psi_p^-\right)(1 + \delta_{p0}) = \\ &\qquad \sum_n k_{xn}^+ \left(k_{xn}^+ k_{zn}^+ \tilde{\Phi}_n^- + \omega\mu_0 k_y \tilde{\Psi}_n^+\right) F_{pn}, \\ &\left(j\omega\epsilon_0 k_{xp}^- \Phi_p^- (1 - \delta_{p0}) + k_y k_{zp}^- \Psi_p^-\right)(1 + \delta_{p0}) = \\ &\qquad \sum_n k_{xn}^+ \left(\omega\epsilon_0 k_{xn}^+ \tilde{\Phi}_n^+ + k_y k_{zn}^+ \tilde{\Psi}_n^-\right) F_{pn}, \end{aligned} \tag{6.13}$$

where $p \in \mathbb{N} \cup 0$. Similarly, for E_y, H_x, one obtains:

$$\begin{aligned}
&\left(k_y k_{zp}^- \Phi_p^- + j\omega\mu_0 k_{xp}^- \Psi_p^-\right) = \\
&\qquad -jk_{xp}^- \sum_n \left(k_y k_{zn}^+ \tilde{\Phi}_n^- - \omega\mu_0 k_{xn}^+ \tilde{\Psi}_n^+\right) F_{pn}, \\
&\left(\omega\epsilon_0 k_y \Phi_p^- + jk_{xp}^- k_{zyp}^- \Psi_p^-\right) = \\
&\qquad -jk_{xp}^- \sum_n \left(\omega\epsilon_0 k_y \tilde{\Phi}_n^+ - k_{xn}^+ k_{zn}^+ \tilde{\Psi}_n^-\right) F_{pn},
\end{aligned} \tag{6.14}$$

where $p \in \mathbb{N}$ and the term F_{pn}, defined as follows:

$$F_{pn} = \frac{4e^{jp\pi/2}}{d} \frac{\sin\left(\left[k_{xn}^+ - k_{xp}^-\right] d/2\right)}{k_{xn}^{+2} - k_{xp}^{-2}} \tag{6.15}$$

was introduced to shorten notation. To eliminate Ψ_p^- and Φ_p^- from Eq. (6.13) and Eq. (6.14) the first equation in Eq. (6.13) is multiplied by the $\omega\epsilon_0$ and then the second equation multiplied by the k_{zp}^- is subtracted. Similarly, multiplying the first equation in Eq. (6.14) by the $\omega\epsilon_0$ and subtracting the second equation multiplied by the k_{zp}^- allows one to eliminate Φ_p^-. Consequently, the following system of linear equations for the unknown amplitudes Ψ_p^- ($p \in \mathbb{N} \cup 0$) is obtained:

$$\begin{aligned}
&k_y \left(k^2 - k_{zp}^{-2}\right)(1 + \delta_{p0}) \Psi_p^- = \sum_n \Big[k_y \left(k^2 \tilde{\Psi}_n^+ - k_{zn}^+ k_{zp}^- \tilde{\Psi}_n^-\right) + \\
&\qquad \omega\epsilon_0 k_{xn}^+ \left(k_{zn}^+ \tilde{\Phi}_n^- - k_{zp}^- \tilde{\Phi}_n^+\right)\Big] k_{xn}^+ F_{pn}, \\
&\left(k^2 - k_{zp}^{-2}\right) \Psi_p^- = \sum_n \Big[\omega\epsilon_0 k_y \left(k_{zp}^- \tilde{\Phi}_n^+ - k_{zn}^+ \tilde{\Phi}_n^-\right) + \\
&\qquad k_{xn}^+ \left(k^2 \tilde{\Psi}_n^+ - k_{zn}^+ k_{zp}^- \tilde{\Psi}_n^-\right)\Big] F_{pn}.
\end{aligned} \tag{6.16}$$

In a similar manner the first equation in Eq. (6.13) is multiplied by the k_{zp}^- and then the second equation multiplied by the $\omega\mu_0$ is subtracted. Next, multiplying the first equation in Eq. (6.14) by the k_{zp}^- and subtracting the second equation multiplied by the $\omega\mu_0$ yields the system of linear equations

for the unknown amplitudes Φ_p^- $(p \in \mathbb{N})$:

$$\begin{aligned} k_{xp}^- \left(k^2 - k_{zp}^{-2}\right) \Phi_p^- = j \sum_n \Big[\omega\mu_0 k_y \left(k_{zp}^- \tilde{\Psi}_n^+ - k_{zn}^+ \tilde{\Psi}_n^- \right) - \\ k_{xn}^+ \left(k^2 \tilde{\Phi}_n^+ - k_{zn}^+ k_{zp}^- \tilde{\Phi}_n^- \right) \Big] k_{xn}^+ F_{pn}, \end{aligned} \tag{6.17}$$

$$\begin{aligned} k_y \left(k^2 - k_{zp}^{-2}\right) \Phi_p^- = -j k_{xp}^- \sum_n \Big[k_y \left(k^2 \tilde{\Phi}_n^+ - k_{zn}^+ k_{zp}^- \tilde{\Phi}_n^- \right) + \\ \omega\mu_0 k_{xn}^+ \left(k_{zp}^- \tilde{\Psi}_n^+ - k_{zn}^+ \tilde{\Psi}_n^- \right) \Big] F_{pn}. \end{aligned}$$

From Eq. (6.16) and Eq. (6.17) the unknown partial wave amplitudes in the waveguides Ψ_p^- and Φ_p^-can be easily eliminated. After some straightforward algebra one obtains for $p \in \mathbb{N}$:

$$\begin{aligned} &\sum_n \left(k_y^2 + k_{xn}^{+2}\right) \left[k_{zn}^+ \tilde{\Phi}_n^- - k_{zp}^- \tilde{\Phi}_n^+ \right] F_{pn} = 0, \\ &\sum_n \Big[\omega\mu_0 k_{xn}^+ \left(k^2 - k_{zp}^{-2}\right) \left(k_{zp}^- \tilde{\Psi}_n^+ - k_{zn}^+ \tilde{\Psi}_n^- \right) + \\ &\qquad k_y \left(k_{zn}^{+2} - k_{zp}^{-2}\right) \left(k^2 \tilde{\Phi}_n^+ - k_{zn}^+ k_{zp}^- \tilde{\Phi}_n^- \right) \Big] F_{pn} = 0, \end{aligned} \tag{6.18}$$

and for $p = 0$:

$$\sum_n k_{xn}^+ \left[\omega\mu_0 k_y \left(k_{zn}^+ \tilde{\Psi}_n^- - k_{z0}^- \tilde{\Psi}_n^+ \right) + k_{xn}^+ \left(k^2 \tilde{\Phi}_n^+ - k_{zn}^+ k_{z0}^- \tilde{\Phi}_n^- \right) \right] = 0. \tag{6.19}$$

It should be noted that the boundary conditions given by Eq. (6.10) in the waveguides ($z < 0$) are satisfied directly by the corresponding field representation (see Eq. (6.7) and Eq. (6.9)). To obey the conditions on the rest of the boundary, that is for the tangential components of the electric field vector in the plane $z = +0$ (upper equation in Eq. (6.10)) and the edge conditions, Eq. (6.11) the following expansion is used [62] (compare with Eq. (2.12) and Eq. (2.15) in the Section 2.2.):

$$\sum_n P_n^\mu(\cos\Delta) e^{-jnKx} = \begin{cases} \dfrac{C e^{jKx/2}}{(\cos(Kx) - \cos\Delta)^{\mu+1/2}}, |x| < d/2, \\ 0,\ d/2 < |x| < \Lambda/2, \end{cases} \tag{6.20}$$

where the constant terms:

$$C = (\pi/2)^{1/2}(\sin\Delta)^{\mu}/\Gamma(1/2-\mu),\ \Delta = \pi d/\Lambda$$

were introduced to shorten notation; P_n^{μ} are the Legendre functions; Γ is the gamma-function.

Multiplying Eq. (6.20) by the e^{-jmKx}, where m is some integer, and taking a linear combination of the resulting equations, after straightforward algebraic manipulations, we obtain (compare with Eq. (2.46) and Eq. (2.47) in the Section 2.2.1.):

$$\sum_{m,n}\alpha_m P^{\mu}_{n-m}(\vartheta)e^{-jnKx} = \begin{cases} \dfrac{Ce^{jKx/2}}{(\cos(Kx)-\vartheta)^{\mu+1/2}}\displaystyle\sum_m \alpha_m e^{-jmKx}, |x| < d/2, \\ 0,\ d/2 < |x| < \Lambda/2. \end{cases} \tag{6.21}$$

$$\vartheta = \cos\Delta,\ \Delta = \pi d/\Lambda,\ C = (\pi/2)^{1/2}(\sin\Delta)^{\mu}/\Gamma(1/2-\mu),$$

where $m, n \in \mathbb{Z} \cup 0$ hereinafter, unless otherwise stated. Apparently, Eq. (6.21) represents the Fourier series of certain Λ-periodic function, vanishing in certain domains and having singular behavior at the bounds of the above domains (at the edges of the waveguide walls) in accordance with Eq. (6.11), if $\mu = -1/6$ is applied. In what follows, the argument of the Legendre functions P^{μ}_{n-m} will be omitted to shorten notations. The expression for the $E_x(x, +0, 0)$ can be rewritten in the following form which allows application of the Eq. (6.21):

$$E_x(x) = \sum_n E^+_{xn}e^{-jk^+_{xn}x} = e^{-jk_x x}\sum_{n,m}\alpha_m P^{\mu}_{n-m}e^{-jnKx}, \tag{6.22}$$

where $\mu = -1/6$ hereinafter. It is easy to see, that the x-component of the electric field written given by Eq. (6.22) satisfies Eq. (6.10) and Eq. (6.11). A similar expansion is then applied to the x-derivative of the $E_y(x, +0, 0)$ (since this function is singular at the edges of the waveguide walls):

$$\frac{\partial E_y(x)}{\partial x} = -j\sum_n k^+_{nx}E^+_{yn}e^{-jk^+_{xn}x} = e^{-jk_x x}\sum_{n,m}\beta_m P^{\mu}_{n-m}e^{-jnKx}. \tag{6.23}$$

Besides, to obey Eq. (6.10) the following supplementary constraint should be added:

$$E_y(x, 0, +0) = 0,\ \ x = (m+1/2)\Lambda. \tag{6.24}$$

Substituting the corresponding expressions for E^+_{xn} and E^+_{yn} from Eq. (6.5) into Eq. (6.22) and Eq. (6.23) the system of linear equations relating $\tilde{\Phi}^+_n$ and $\tilde{\Psi}^+_n$ with α_m and β_m can be obtained:

$$\begin{aligned} &k^+_{xn}k^+_{zn}\tilde{\Phi}^-_n + \omega\mu_0 k_y \tilde{\Psi}^+_n = \sum_m \alpha_m P^\mu_{n-m}, \\ &k^+_{xn}\left(-k_y k^+_{zn}\tilde{\Phi}^-_n + \omega\mu_0 k^+_{xn}\tilde{\Psi}^+_n\right) = \sum_m \beta_m P^\mu_{n-m}. \end{aligned} \tag{6.25}$$

which yields the expressions for $\tilde{\Phi}^+_n$ and $\tilde{\Psi}^+_n$:

$$\begin{aligned} \tilde{\Phi}^-_n &= \frac{k^+_{xn}}{k^+_{zn}\left(k^{+2}_{xn}+k^2_y\right)}\sum_m\left(\alpha_m - \frac{k_y}{k^{+2}_{xn}}\beta_m\right)P^\mu_{n-m}, \\ \tilde{\Psi}^+_n &= \frac{1}{\omega\mu_0\left(k^{+2}_{xn}+k^2_y\right)}\sum_m\left(k_y\alpha_m+\beta_m\right)P^\mu_{n-m}. \end{aligned} \tag{6.26}$$

Substituting Eq. (6.26) into Eq. (6.18) and Eq. (6.19) and taking into account that:

$$\tilde{\Phi}^+_n = 2\delta_{n0}\Phi^I - \tilde{\Phi}^-_n,\ \tilde{\Psi}^-_n = 2\delta_{n0}\Psi^I - \tilde{\Psi}^+_n, \tag{6.27}$$

after some algebra one obtains a system of linear equations for unknown coefficients α_m and β_m for $p > 0$:

$$\begin{aligned} &\sum_{n,m}P^\mu_{n-m}\left[k_y k^+_{xn}k^-_{zp}\alpha_m + \left(\frac{k^+_{zn}(k^2_y+k^{-2}_{xp})-k^2_y k^-_{zp}}{k^+_{xn}}\right)\beta_m\right]\left(\frac{k^+_{zn}+k^-_{zp}}{k^+_{zn}}\right)F_{pn} = \\ &\qquad 2F_{p0}\left(\omega\mu_0 k_x k_z(k^{-2}_{xp}+k^2_y)\Psi^I - k^2 k_y(k^2_z - k^{-2}_{zp})\Phi^I\right), \end{aligned} \tag{6.28}$$

$$\sum_{n,m}P^\mu_{n-m}\left[k^+_{xn}\alpha_m - \frac{k_y}{k^+_{xn}}\beta_m\right]\left(\frac{k^+_{zn}+k^-_{zp}}{k^+_{zn}}\right)F_{pn} = 2F_{p0}k^-_{zp}(k^2_x+k^2_y)\Phi^I,$$

and for $p = 0$:

$$\begin{aligned} &\sum_{n,m}P^\mu_{n-m}\left[\left(k^+_{zn}(k^+_{zn}+k^-_{z0})+k^{+2}_{xn}\right)\alpha_m - k_y\beta_m\right]\frac{k^+_{xn}}{k^+_{zn}}F_{0n} = \\ &\qquad 2F_{00}k_x\left(\omega\mu_0 k_y k_z\Psi^I + k^2 k_x\Phi^I\right). \end{aligned} \tag{6.29}$$

Additionally, the constraint given by Eq. (6.24) yields:

$$\sum_{n,m} \frac{(-1)^n}{k_{xn}^+} P_{n-m}^{\mu} \beta_m = 0. \tag{6.30}$$

The system of equations, given by Eqs. (6.28), (6.29) together with Eq. (6.30) should be solved numerically. To this end it should be properly truncated (this is discussed briefly below). Once the coefficients α_m and β_m are known, the field components in both regions can be found. Namely, for $z > 0$ the Eq. (6.26) and Eq. (6.6) are used to find the field amplitudes from Eq. (6.5). The amplitudes of partial waves Φ_p^- and Ψ_p^- for $z < 0$ can be evaluated using the following expressions:

$$\begin{aligned} \Psi_p^- = \frac{C_p}{(1+\delta_{p0})k_y} \sum_n \Big[k_y \left(k^2 \tilde{\Psi}_n^+ - k_{zn}^+ k_{zp}^- \tilde{\Psi}_n^- \right) - \\ \omega \epsilon_0 k_{xn}^+ \left(k_{zp}^- \tilde{\Phi}_n^+ - k_{zn}^+ \tilde{\Phi}_n^- \right) \Big] k_{xn}^+ F_{pn}, \; p \geq 0, \\ \Phi_p^- = \frac{jC_p}{k_{xp}^-} \sum_n \Big[k_y \omega \mu_0 \left(k_{zp}^- \tilde{\Psi}_n^+ - k_{zn}^+ \tilde{\Psi}_n^- \right) - \\ k_{xn}^+ \left(k^2 \tilde{\Phi}_n^+ - k_{zn}^+ k_{zp}^- \tilde{\Phi}_n^- \right) \Big] k_{xn}^+ F_{pn}, \; p > 0, \\ C_p = 2 \exp(jp\pi/2) / \left(d(k_{xp}^{-2} + k_y^2) \right), \end{aligned} \tag{6.31}$$

resulting directly from Eq. (6.18) and Eq. (6.19). Substituting Eq. (6.31) into Eq. (6.9) the field amplitudes for $z < 0$ can be found. Investigation of the uniqueness and existence of the solution of infinite system of linear equations like that given by Eqs. (6.28) through (6.30) is fraught with difficulties and is beyond the scope of present study. A detailed discussion concerning a similar problem can be found e.g. in [125]. To obtain a numerical solution the systems of equations like that given by Eqs. (6.28) through (6.30) should be truncated. Physically this means that only the modes transporting the energy away from the $y = 0$ plane and a finite number of lower order evanescent modes are accounted for in the solution. The truncated system for unknown vectors α_m and β_m, $m = -M..M$ (where M is a truncation index) has the coefficients in the form of infinite series (summation over n). In order to calculate the matrix elements of the truncated system, the series have to be truncated too at some index N large enough to assure convergence. Taking into account that $P_n^{\mu} = O(n^{-2/3})$ for $\mu = -1/6$ (see

e.g. [126], Eq. (2)) and the term $F_{pn} = O(n^{-2}),\ n \to \infty$ in Eq. (6.15) one readily obtains: the coefficients of the system give by Eq. (6.28) and Eq. (6.29) behave like $O(n^{-5/3})$ for α_m and $O(n^{-8/3})$ for β_m, whereas the coefficients in Eq. (6.30) behave like $O(n^{-5/3})$ which makes them suitable for numerical evaluation. Generally, the series in Eq. (6.28) through Eq. (6.30) are fast converging [127] and even for $M = 15 \div 30$ the results assure acceptable accuracy, provided that N is at least about one order of magnitude higher than M [42]. Eliminating the coefficients α_m from Eq. (6.28) and Eq. (6.29) the following truncated system for unknown coefficients β_m is obtained:

$$\mathrm{B}\beta = \mathrm{b}, \tag{6.32}$$

where the elements of matrix B and vector b are:

$$\begin{gathered} B_{0m} = \sum_n \frac{(-1)^n}{k_{xn}^+} P_{n-m}^{\mu}, \qquad b_0 = 0, \\ B_{pm} = \sum_n \left(\frac{k_{zn}^+ + k_{zp}^-}{k_{xn}^+} \right) F_{pn} P_{n-m}^{\mu},\ b_p = 2F_{p0} k_z \left(\omega\mu_0 k_x \Psi^I - k_y k_z \Phi^I \right), \end{gathered} \tag{6.33}$$

and $m = -M...M$, $n = -N...N$, $p = 1...2M-1$ hereinafter. Solving Eq. (6.32) for the unknown β and substituting them into the second system of equations in Eq. (6.28) and into Eq. (6.29) yields the system of linear equations for the unknown coefficients α:

$$\mathrm{A}\alpha = \mathrm{a}, \tag{6.34}$$

where the elements of A and a are defined below:

$$\begin{gathered} A_{0m} = \sum_n \frac{k_{xn}^+}{k_{zn}^+} \left(k_{zn}^+ (k_{zn}^+ + k_{z0}^-) + k_{xn}^{+\,2} \right) F_{0n} P_{n-m}^{\mu}, \\ a_0 = \sum_m \left(\sum_n \frac{k_{xn}^+}{k_{zn}^+} k_y F_{0n} P_{n-m}^{\mu} \right) \beta_m + 2F_{00} \left(\omega\mu_0 k_y k_z \Psi^I + k^2 k_x \Phi^I \right), \\ A_{pm} = \sum_n \left(\frac{k_{zn}^+ + k_{zp}^-}{k_{zn}^+ k_{zp}^-} \right) k_{xn}^+ F_{pn} P_{n-m}^{\mu}, \\ a_p = \sum_m \left(\sum_n \left(\frac{k_{zn}^+ + k_{zp}^-}{k_{xn}^+ k_{zn}^+} \right) \frac{k_y}{k_{zp}^-} F_{pn} P_{n-m}^{\mu} \right) \beta_m + 2F_{p0} (k_{xn}^{+\,2} + k_y^2) \Phi^I. \end{gathered} \tag{6.35}$$

Some computed examples are shown in Fig. 6.2 where the dependence of the transmitted field power versus the normalized period is shown. The former is defined as the real part of the complex Poynting flux:

$$P^{-} = \frac{d}{2\Lambda} \sum_{p:k_{zp}^{-}\text{real}} (1+\delta_{p0})(k_{xp}^{-\,2} + k_y^2) k_{zp}^{-} \omega \left(\mu_0 \left| \Psi_p^{-} \right|^2 + \epsilon_0 \left| \Phi_p^{-} \right|^2 \right). \tag{6.36}$$

Similarly, the reflected field power is:

$$P^{+} = \sum_{n:k_{zn}^{+}\text{real}} (k_{xn}^{+\,2} + k_y^2) k_{zn}^{+} \omega \left(\mu_0 \left| \Psi_n^{+} \right|^2 + \epsilon_0 \left| \Phi_n^{+} \right|^2 \right). \tag{6.37}$$

In turn, the incident wave power is:

$$P^{I} = (k_x^2 + k_y^2) k_z \omega \left(\mu_0 \left| \Psi^{I} \right|^2 + \epsilon_0 \left| \Phi^{I} \right|^2 \right). \tag{6.38}$$

The incident wave of unit power density is assumed here. Moreover, for simplicity, $\Phi^I = 0$ is applied (the electric field vector of the incident wave is parallel to the $z = 0$ plane, see Fig. 6.1). The resonant phenomena (the peaks of the transmitted field power) are clearly observable for the values of $\Lambda/\lambda \geq 0.5$. The inflection points of the curves correspond to the critical values of wavelength λ_k of the harmonics in the upper and lower half-planes. From Eq. (6.4) in the upper half-plane one has:

$$\Lambda/\lambda_k = n \left(\frac{\sin\theta \sin\varphi + S_n \sqrt{\sin^2\theta \cos^2\varphi + \cos^2\theta}}{\cos^2\theta} \right),$$

where $S_n = 1$ for $n > 0$ and -1 for $n < 0$; $+$ and $-$ signs correspond to the backward and forward propagating harmonics respectively. In the waveguides, $y < 0$, from Eq. (6.6) it results:

$$d/\lambda_k = p/\sqrt{1 - \sin^2\theta \sin^2\varphi}, \quad p = 1, 2, \ldots .$$

Thus, for instance, in the case of $\theta = 30^\circ$ and $\varphi = 45^\circ$ the inflection points are located at $\Lambda/\lambda \approx 0.76n$ for the backward propagating modes and $\Lambda/\lambda \approx 1.72n$ for the forward propagating ones in the upper half-plane, whereas the waveguide modes start propagating at $\Lambda/\lambda \approx 1.07p$ (for the considered case of $\Lambda/\lambda = 2$).

In Fig. 6.3 the dependence of the transmitted filed power versus the incidence angle θ for different fixed values of the angle φ (see Fig. 6.1) and unit power density of the incident wave is shown. In the case, illustrated in Fig. 6.3(a), the

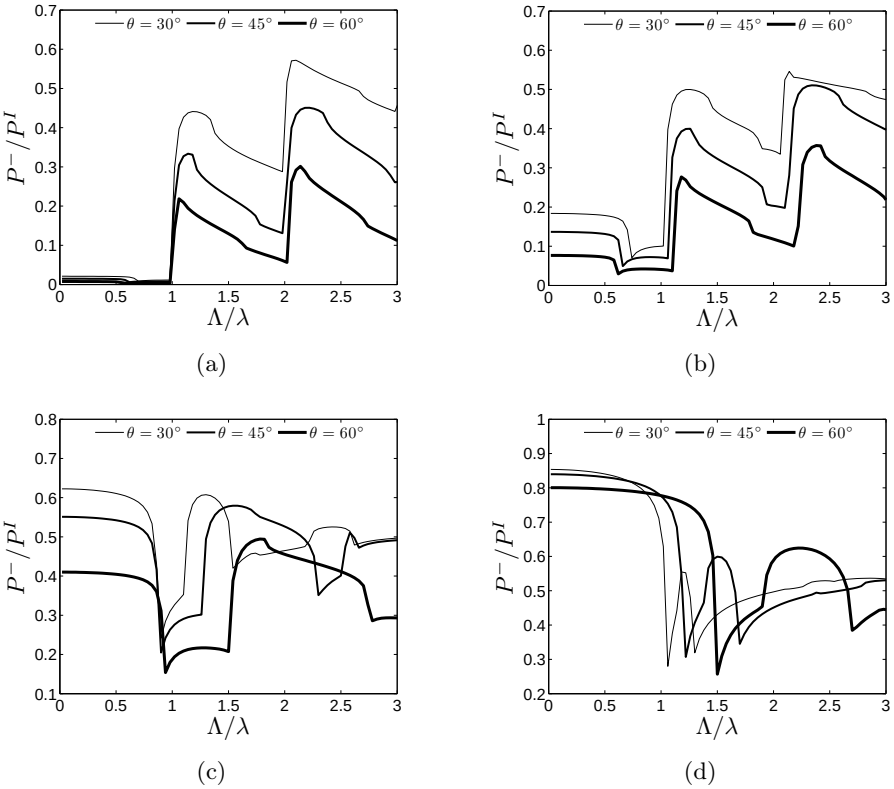

Figure 6.2. Dependence of the transmitted field power versus the normalized period for different angles ϕ and θ: (a) $\phi = 10^\circ$, (b) $\phi = 30^\circ$, (c) $\phi = 60^\circ$, (d) $\phi = 80^\circ$; $\Lambda/d = 2$

electric field vector of the incident wave is parallel to the plane $z = 0$, and in Fig. 6.3(b) a similar polarization of the magnetic field vector of the incident wave is assumed. These examples correspond to $\Phi^I = 0$, $\Psi^I = 1/\sqrt{\rho_0}k^2 \sin\theta$ (Fig. 6.3(a)) and $\Psi^I = 0$ and $\Phi^I = \sqrt{\rho_0}/k^2 \sin\theta$ (Fig. 6.3(b)), respectively, where $\rho_0 = \sqrt{\mu_0/\epsilon_0}$ is the intrinsic impedance of free space

Finally, in Fig. 6.4 an example analogous to the one considered in [128] where the diffraction by an infinite array of infinitesimal strips was studied. For the limiting case of semi-infinite strips the authors derive the expression for the magnitude of the reflection coefficient (see Eq. (27) on p.1928 in [128]):

$$|H_{y0}^{+}/H^I| = (1 - \cos\theta)/(1 + \cos\theta) \tag{6.39}$$

provided $\Lambda < \lambda/2$. In Fig. 6.4 the magnitude of the reflection coefficient defined by Eq. (6.39) is shown for two different values of the waveguide walls thickness

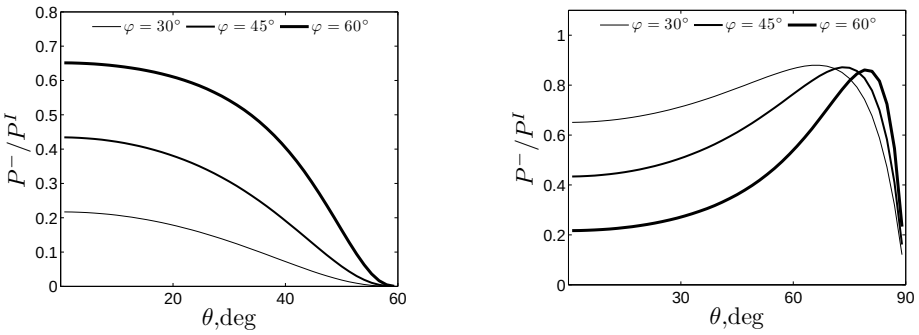

Figure 6.3. Dependence of the transmitted field power versus the angle θ for fixed values of φ: a) $\vec{E}^I$ parallel to the plane $z = 0$; b) $\vec{H}^I$ parallel to the plane $z = 0$. 30°, 45° and 60° and b) φ for fixed values of θ: 30°, 45° and 60°; $\Lambda/d = 2,\ \Lambda/\lambda = 0.5$.

w. The case of $\varphi = 0$ is considered. It should be noted that for waves propagating in the $y = 0$ plane, with $k_y = 0$ (see Fig. 6.1), the field components separate in H and E polarized waves. In this example the reflection coefficient $|H^+_{y0}/H^I|$ concerns the H wave ($\Psi^I = 0$). It is easy to observe that the curves approach

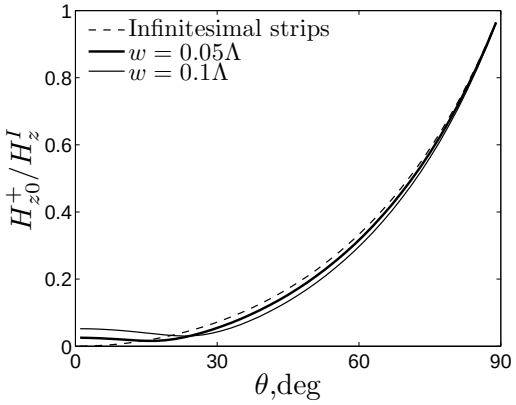

Figure 6.4. Dependence of the reflection coefficient versus the incidence angle θ for small values of the waveguide walls thickness w; $\Lambda = \lambda/4$. Dashed line corresponds to the limiting case of infinitesimal strips (see Eq. (6.39)).

the limiting case of infinitesimal strips depicted by the dashed line in Fig. 6.4, which corresponds to Eq. (6.39), as $w \to 0$.

6.1.2. Plane wave scattering by a periodic system of thick electrodes.

The method of analysis presented in the previous Section for the case of a thick-walled parallel-plate waveguide array can be easily generalized for the case of a grating comprised of perfectly conducting electrodes of finite thickness (bars), shown in Fig. 6.5. The period of the structure is again denoted as Λ; d

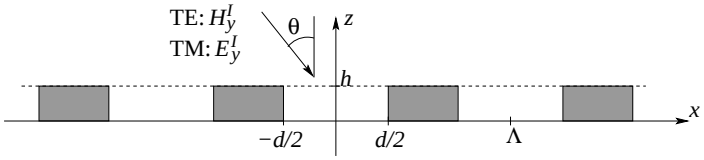

Figure 6.5. Periodic array of perfectly conducting electrodes of finite thickness (bars).

and h are the distance between bars and the bar's thickness, respectively. The following variables are introduced to shorten notation in the further analysis: $\hat{\Lambda} = \Lambda/2$, $\hat{d} = d/2$ and $\hat{h} = h/2$. The system homogeneous in the y-axis direction and periodic in the x-axis direction is assumed. An incident plane harmonic wave of the angular frequency ω impinges on the system at the angle θ counted from the z-axis and the term $e^{j\omega t}$ will be omitted again. In the case of TM incidence the only nonzero component of the magnetic field vector is H_z, whereas E_z is the only nonzero component of the electric field in the case of TE polarization of the incident wave. The total field resulting from the Maxwell equations can be represented as follows:

$$\begin{aligned} &\text{TM incidence: } H_y,\ E_x = -j\nu H_{y,z},\ E_z = j\nu H_{y,x} \\ &\text{TE incidence: } E_y,\ H_x = -j\nu E_{y,z},\ H_z = j\nu E_{y,x}, \end{aligned} \tag{6.40}$$

where $\nu = (\omega\epsilon_0)^{-1}$ for TM and $\nu = (\omega\mu_0)^{-1}$ for TE case. The total field can be represented in the following form (TM):

$$\begin{aligned} \text{TM incidence:}\quad & H_y = H_y^+ + H_y^I,\ E_i = E_i^+ + E_i^I,\ z > h, \\ & H_y = H_y^-,\ E_i = E_i^-,\ z < h, \\ \text{TE incidence:}\quad & E_y = E_y^+ + E_y^I,\ H_i = H_i^+ + H_i^I,\ z > h, \\ & E_y = E_y^-,\ H_i = H_i^-,\ z < h, \end{aligned} \tag{6.41}$$

where $i = x, z$ and I denotes the field of given incident wave:

$$\begin{aligned}
&\text{TM incidence: } H_y^I = e^{-j(k_x x - k_z z)}, E_x^I = \nu k_z H_y^I,\ E_z^I = \nu k_x H_y^I,\\
&\text{TE incidence: } E_y^I = e^{-j(k_x x - k_z z)}, H_x^I = \nu k_z E_y^I,\ H_z^I = \nu k_x H_y^I,\\
&k_x = k\sin\theta, k_z = k\cos\theta,\ k = 2\pi/\lambda,
\end{aligned} \tag{6.42}$$

and the superscripts $+/-$ in Eq. (6.41) denote the scattered field above and below the bars, respectively. Due to the system periodicity the scattered field outside the bars ($z > h$ or $z < 0$) can be represented by a series of spatial harmonics according to the Floquet's theorem:

$$\begin{aligned}
&\psi_n^{\pm} = e^{-j(k_{xn}x \pm k_{zn}(z+\hat{h}\pm\hat{h}))},\ k^2 = k_{xn}^2 + k_{zn}^2,\ k_{xn} = k_x + nK,\\
&k_{zn} = \begin{cases} (k^2 - k_{xn}^2)^{1/2}, & k \geq k_{xn},\\ -j(k_{xn}^2 - k^2)^{1/2}, & k < k_{xn}, \end{cases} \quad K = 2\pi/\Lambda,
\end{aligned} \tag{6.43}$$

with amplitudes $\Psi_n^{\pm}$. Substituting Eq. (6.43) into Eq. (6.40) one obtains for the scattered field the following expression:

$$\begin{aligned}
&\text{TM incidence: } H_y^{\pm} = \sum_n \Psi_n^{\pm}\psi_n^{\pm},\\
&E_x^{\pm} = -\nu\sum_n k_{zn}\Psi_n^{\pm}\psi_n^{\pm},\ E_z^{\pm} = \nu\sum_n k_{xn}\Psi_n^{\pm}\psi_n^{\pm},\\
&\text{TE incidence: } E_y^{\pm} = \sum_n \Psi_n^{\pm}\psi_n^{\pm},\\
&H_x^{\pm} = \nu\sum_n k_{zn}\Psi_n^{\pm}\psi_n^{\pm},\ H_y z^{\pm} = -\nu\sum_n k_{xn}\Psi_n^{\pm}\psi_n^{\pm},
\end{aligned} \tag{6.44}$$

where $n \in \mathbb{Z}$, unless otherwise stated. The scattered field between bars can be represented by a series of the parallel plate waveguide modes as follows (for

$-\hat{\Lambda} < x < \hat{\Lambda}, 0 < z < h$):

$$\begin{aligned}
& & H_y^b &= \sum_p \left(\Phi_p^+ e^{j\eta_p z} + \Phi_p^- e^{-j\eta_p z}\right) \cos(\xi_p(x+\hat{d})), \\
& \text{TM:} & E_x^b &= \nu \sum_p \eta_p \left(\Phi_p^+ e^{j\eta_p z} + \Phi_p^- e^{-j\eta_p z}\right) \cos(\xi_p(x+\hat{d})), \\
& & E_z^b &= -j\nu \sum_p \xi_p \left(\Phi_p^+ e^{j\eta_p z} + \Phi_p^- e^{-j\eta_p z}\right) \sin(\xi_p(x+\hat{d})),
\end{aligned} \tag{6.45}$$

$$\begin{aligned}
& & E_y^b &= \sum_p \left(\Phi_p^+ e^{j\eta_p z} + \Phi_p^- e^{-j\eta_p z}\right) \sin(\xi_p(x+\hat{d})), \\
& \text{TE:} & H_x^b &= -\nu \sum_p \eta_p \left(\Phi_p^+ e^{j\eta_p z} + \Phi_p^- e^{-j\eta_p z}\right) \sin(\xi_p(x+\hat{d})), \\
& & H_z^b &= -j\nu \sum_p \xi_p \left(\Phi_p^+ e^{j\eta_p z} + \Phi_p^- e^{-j\eta_p z}\right) \cos(\xi_p(x+\hat{d})),
\end{aligned}$$

where $\Phi_p^{\pm}$ are unknown mode amplitudes; $p \in \mathbb{N} \cup 0$ for TM and $p \in \mathbb{N}$ for TE incidence, unless otherwise stated. The propagation constants ξ_p and η_p are defined below:

$$\xi_p = p\pi/d, \;\; \eta_p = \begin{cases} \left(k^2 - (\xi_p)^2\right)^{1/2} & \text{for real } \eta_p, \\ -j\left((\xi_p)^2 - k^2\right)^{1/2} & \text{for imaginary } \eta_p. \end{cases} \tag{6.46}$$

The mode amplitudes in different periods of the array are related to that defined in Eq. (6.45) by simple relation (see also Eq. (6.8))

$$\Phi_p^{\pm m} = \Phi_p^{\pm} e^{-jk_x m\Lambda}, \;\; \Phi_p^{\pm} = \Phi_p^{\pm 0}, \; m \in \mathbb{Z}. \tag{6.47}$$

The boundary and edge conditions similar as in the case of the waveguide array (see Eq. (6.10) and Eq. (6.11)) must be satisfied. Namely, for TM polarization of the incident wave:

$$\begin{aligned}
& E_x = 0, \;\; \hat{d} < |x| < \hat{\Lambda}, \;\; z = +h, z = -0, \text{ outside bars}, \\
& E_z = 0, \;\; x = \pm\hat{d}, \;\; 0 < z < h, \text{ between bars}.
\end{aligned} \tag{6.48}$$

In the case of TE polarization the above conditions hold for the E_z component of electric field. Besides, near the bars' edges the tangential components of the electric (TM) and magnetic (TE) field vectors exhibit singular behavior:

$$\begin{gathered}
\text{TM: } E_i = O(\varrho^{-\frac{1}{3}}), \;\; \text{TE: } H_i = O(\varrho^{-\frac{1}{3}}), \;\; i = x, z, \\
\varrho = \sqrt{(x \pm \hat{d})^2 + z^2}, \;\; \varrho \to 0.
\end{gathered} \tag{6.49}$$

Conditions between bars given by Eq. (6.48) are satisfied directly by field representation, Eq. (6.45). To obey the boundary conditions outside the bars, the solution for the E_x component of the electric field in TM case is assumed in the form of expansion (compare with Eq. (6.22)):

$$\begin{aligned} E_x(x,+h) &= \nu \sum_{n,m} \alpha_m^+ P_{n-m}^{\mu}(\cos\Delta) e^{-jk_{xn}x}, \\ E_x(x,-0) &= \nu \sum_{n,m} \alpha_m^- P_{n-m}^{\mu}(\cos\Delta) e^{-jk_{xn}x}, \end{aligned} \tag{6.50}$$

where $\mu = -1/6$; P are the Legendre functions; $\Delta = \pi d/\Lambda$.

Comparing Eq. (6.50) with Eq. (6.41) through Eq. (6.43) the following relationship between the corresponding amplitudes of spatial harmonics $\Psi_n^{\pm}$ and the expansion coefficients $\alpha_m^{\pm}$ can be deduced:

$$\begin{aligned} \Psi_n^+ &= \delta_{n0} e^{jk_z h} - k_{zn}^{-1} \sum_m \alpha_m^+ P_{n-m}^{\mu}, \\ \Psi_n^- &= k_{zn}^{-1} \sum_m \alpha_m^- P_{n-m}^{\mu}, \end{aligned} \tag{6.51}$$

where δ_{nI} is Kronecker delta. In Eq. (6.51) the arguments of the Legendre functions were dropped to shorten notation. In the case of TE polarization a similar expansion is applied to the x-derivative of the E_y component (compare with Eq. (6.23)):

$$\begin{aligned} E_{y,x}(x,+h) &= \sum_{n,m} \alpha_m^+ P_{n-m}^{\mu} e^{-jk_{xn}x},\ E_y(l\Lambda,+h) = 0, \\ E_{y,x}(x,-0) &= \sum_{n,m} \alpha_m^- P_{n-m}^{\mu} e^{-jk_{xn}x},\ E_y(l\Lambda,-0) = 0,\ l \in \mathbb{Z}. \end{aligned} \tag{6.52}$$

In Eq. (6.52) the additional condition is applied to obey the boundary conditions outside the bars, Eq. (6.48) for the E_y component of the electric field. Taking into account Eq. (6.41) through Eq. (6.43) the following relationship between $\Psi_n^{\pm}$ and $\alpha_m^{\pm}$ can be obtained for TE polarization:

$$\begin{aligned} \Psi_n^+ &= -\delta_{n0} e^{jk_z h} + k_{xn}^{-1} \sum_m \alpha_m^+ P_{n-m}^{\mu}, \\ \Psi_n^- &= k_{xn}^{-1} \sum_m \alpha_m^- P_{n-m}^{\mu}. \end{aligned} \tag{6.53}$$

To find the unknown expansion coefficients $\alpha_m^{\pm}$ the continuity of tangential field components on the planes $z = h$ and $y = 0$:

$$\begin{aligned} &\text{TM: } H_y = H_y^b,\ E_x = E_x^b,\ x \in (-\hat{d}, \hat{d}), \\ &\text{TE: } E_y = E_y^b,\ H_x = H_x^b,\ x \in (-\hat{d}, \hat{d}), \end{aligned} \tag{6.54}$$

combined with the mode matching is used, as in the case of the parallel-plate waveguide array discussed earlier (see Section 6.1.1.)

It could be easily noticed from the above discussion that the field representations for both TM and TE polarization are quite similar. It appears that it is sufficient to derive the system of linear equations for unknown $\alpha_m^{\pm}$ for the TM incidence only. Applying the same considerations and following a similar scheme one can easily solve the problem for TE polarization too. Hence, in what follows, the case of TM incidence will be addressed in details. Only the general remarks will be given, if needed, to emphasize the main differences of both TM and TE polarizations. Substituting the expressions for the tangential components from Eq. (6.41) through Eq. (6.45) into Eq. (6.54) and multiplying the resulting equations by $\cos(\xi_p x + p\pi/2)$, after integration with respect to x from $-\hat{d}$ to $\hat{d}$, the following system of linear equations can be obtained for the case of TM polarization of the incident wave:

$$(\Phi_p^+ + \Phi_p^-)e^{j2\eta_p h} = L_p \sum_n k_{xn} F_{pn} (\delta_{n0} e^{jk_z h} + \Psi_n^+), \tag{6.55a}$$

$$(\Phi_p^+ - \Phi_p^-)e^{j2\eta_p h} = L_p \eta_p^{-1} \sum_n k_{xn} F_{pn} k_{zn} (\delta_{n0} e^{jk_z h} - \Psi_n^+), \tag{6.55b}$$

$$\Phi_p^+ + \Phi_p^- = L_p \sum_n k_{xn} F_{pn} \Psi_n^-, \tag{6.55c}$$

$$\Phi_p^+ - \Phi_p^- = L_p \eta_p^{-1} \sum_n k_{xn} F_{pn} k_{zn} \Psi_n^-, \tag{6.55d}$$

where

$$F_{pn} = \frac{\sin \hat{d}(k_{xn} - \xi_p)}{k_{xn}^2 - \xi_p^2}, \quad L_p = \frac{2e^{jp\pi/2}}{\hat{d}(1 + \delta_{p0})}. \tag{6.56}$$

To eliminate the waveguide mode amplitudes $\Phi_p^{\pm}$ from the above one first subtracts the sum of Eq. (6.55b) and Eq. (6.55d) from the sum of Eq. (6.55a) and Eq. (6.55c). Afterwards, one subtracts the sum of Eq. (6.55b) and Eq. (6.55c)

from the sum of Eq. (6.55a) and Eq. (6.55d). This yields:

$$\begin{aligned}(\eta_p \tan \eta_p \hat{h}) \sum_n k_{xn} F_{pn} (\delta_{n0} e^{jk_z h} + \hat{\Psi}_n^+) = \\ j \sum_n k_{xn} F_{pn} k_{zn} (\delta_{n0} e^{jk_z h} - \hat{\Psi}_n^+), \\ (\eta_p j \cot \eta_p \hat{h}) \sum_n k_{xn} F_{pn} (\delta_{n0} e^{jk_z h} + \hat{\Psi}_n^-) = \\ \sum_n k_{xn} F_{pn} k_{zn} (\delta_{n0} e^{jk_z h} - \hat{\Psi}_n^-),\end{aligned} \tag{6.57}$$

where the new amplitudes have been introduced: $\hat{\Psi}_n^{\pm} = \Psi_n^+ \pm \Psi_n^-$. The coefficients $\hat{\Psi}_n^{\pm}$ can be expanded in a similar way into the series like those given by Eq. (6.51) and Eq. (6.53):

$$\hat{\Psi}_n^{\pm} = \delta_{n0} e^{jk_z h} - k_{zn}^{-1} \sum_m \beta_m^{\pm} P_{n-m}^{\mu}, \tag{6.58}$$

and the relation between coefficients $\beta_m^{\pm}$ and $\alpha_m^{\pm}$ can be readily obtained:

$$\beta_m^{\pm} = \frac{1}{2}(\alpha_m^+ \pm \alpha_m^-) \Rightarrow \alpha_m^{\pm} = \frac{1}{2}(\beta_m^+ \pm \beta_m^-). \tag{6.59}$$

Substituting the expansions given by Eq. (6.58) into Eq. (6.55), after some straightforward algebra the following systems of linear equations for unknown coefficients $\beta_m^{\pm}$ can be deduced:

$$\sum_m G_{pm}^{\pm} \beta_m^{\pm} = g_p^{\pm}, \tag{6.60}$$

where

$$\begin{aligned}G_{pm}^+ &= \sum_n P_{n-m}^{\mu} F_{pn} \left(j k_{xn} \eta_p^{-1} \cos \eta_p \hat{h} - k_{xn} k_{zn}^{-1} \sin \eta_p \hat{h} \right), \\ G_{pm}^- &= \sum_n P_{n-m}^{\mu} F_{pn} \left(k_{xn} \eta_p^{-1} \sin \eta_p \hat{h} - j k_{xn} k_{zn}^{-1} \cos \eta_p \hat{h} \right), \\ g_p^+ &= -2 F_{p0} k_x \sin \eta_p \hat{h} e^{jk_z h}, \\ g_p^- &= -2 F_{p0} j k_x \cos \eta_p \hat{h} e^{jk_z h}.\end{aligned} \tag{6.61}$$

Following the same steps as above a similar system of linear equations can be obtained for the case of TE incidence. The corresponding coefficients $G_{pm}^{\pm}$ can be obtained from Eq. (6.61) by swapping over $k_{xn}\eta_p^{-1}$ with $k_{zn}k_{xn}^{-1}$, whereas $g_p^{\pm}$ can be obtained by swapping over k_x with k_z and the sine with cosine functions, respectively. Besides, in the case of the TE polarization to obey the conditions in the centers of the bars on the planes $z = h$ and $z = 0$ (see Eq. (6.52)) the constraint should be added:

$$\sum_m \beta_m^{\pm} \sum_n (-1)^n P_{n-m}^{\mu}/k_{xn}. \tag{6.62}$$

The doubly infinite systems of linear equations given by Eq. (6.60) through Eq. (6.62) should be solved numerically. If the coefficients $\beta_m^{\pm}$ are known, the corresponding $\alpha_m^{\pm}$ and $\Psi_n^{\pm}$ can be found from Eq. (6.58) and Eq. (6.51), Eq. (6.53), respectively. The scattered field outside the bars can be evaluated then using Eq. (6.44). Between bars the scattered field can be found from Eq. (6.45), where $\hat{\Psi}_p^{\pm}$ can be evaluated from Eq. (6.55). Here, the final results are given for TM incidence case:

$$\begin{aligned}
\Phi_p^{\pm} &= e^{\mp\eta\pi\hat{h}}(\hat{\Phi}_p^{+} \pm \hat{\Phi}_p^{-})/4, \\
\hat{\Phi}_p^{+} &= \sec(\eta_p\hat{h})L_p \sum_n k_{xn}F_{pn}(\delta_{n0}e^{jk_zh} + \hat{\Psi}_n^{+}), \\
\hat{\Phi}_p^{-} &= j\csc(\eta_p\hat{h})\eta_p^{-1}L_p \sum_n k_{zn}k_{xn}F_{pn}(\hat{\Psi}_n^{+} - \delta_{n0}e^{jk_zh}),
\end{aligned} \tag{6.63}$$

where $\hat{\Psi}_n^{+} = \Psi_n^{+} + \Psi_n^{-}$ as before. For TE polarization in the above expressions the k_{xn} should be replaced with $-j\xi_p$, $p \in \mathbb{N}$ for TE and $p \in \mathbb{N} \cup 0$ for TM polarization of the incident wave; $n \in \mathbb{Z}$; F_{pn} and L_p are defined by Eq. (6.56).

For numerical computations the system of equations given by Eq. (6.60) through Eq. (6.62) should be truncated so as to take into account only the propagating modes and a finite number of lower order evanescent modes in the solution in a similar manner as it was done in the case of the thick-walled parallel-plate waveguide array, discussed in the Section 6.1.1. The truncated system for unknown vectors $\beta_m^{\pm}$, $m = -M..M$, M is the truncation index, have the coefficients in the form of infinite series (summation over n). In order to calculate the matrix elements of the truncated system from Eq. (6.61), the corresponding series have to be truncated too at some index N large enough to assure convergence. Taking into account that $P_n^{\mu} = O(n^{-2/3})$ for $\mu = -1/6$ (see e.g. [126], Eq. (2)) and the term $F_{pn} = O(n^{-2})$ for large n in Eq. (6.55), one

readily obtains: the coefficients of the system given by Eq. (6.61) behave like $O(n^{-5/3})$ for TM and $O(n^{-8/3})$ for TE incidence, respectively; the coefficients of the system given by Eq. (6.62) behave like $O(n^{-5/3})$. Generally, the series like that appearing in Eq. (6.61) and Eq. (6.62) are fast converging [127] and even for $M = 15 \div 30$ the results assure acceptable accuracy, provided that N is at least about one order of magnitude higher than M [42]. Some computed numerical examples are shown in Fig. 6.6 where the dependence of the transmission coefficient Ψ_0^- versus Λ/λ is shown for different values of the incidence angle. The examples are analogous to those considered in [125] (for convenience they are referred in the embedded graphs) where a similar problem was solved by the direct mode matching method. The comparison reveals a good qualitative agreement of the results obtained by two different methods.

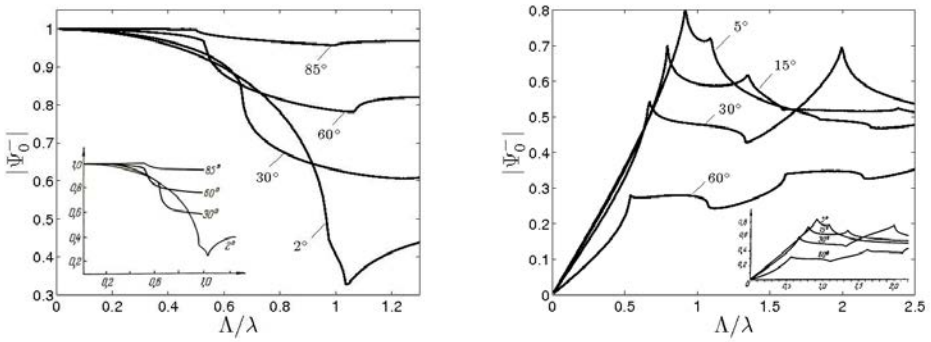

(a) (b)

Figure 6.6. Dependence of the transmission coefficient Ψ_0^- versus Λ/λ for different values of the incident angle and $d = \Lambda/2$, (a) TM and (b) TE polarization. The embedded graphs illustrate the results shown in Figs. 92, 82 of [125] for comparison.

Another example is shown in Fig. 6.7 where the dependence of the transmission coefficient Ψ_0^- versus the Λ/λ is shown for incidence close to normal: the angle of incidence 10^{-2} degrees is applied in the computations (compare with Figs. 86, 87 and Figs 70, 71 of [125]). It should be noted that, similarly as in the case of thick-walled parallel-plate waveguide, the method fails for the case of $\theta = 0°$ since the corresponding systems of equations given by Eq. (6.60) through Eq. (6.62), as well as those given by Eq. (6.32) through Eq. (6.35) in the analysis of the parallel-plate waveguide array, become near singular and numerical solution can not be obtained. But the method works well for $\theta \to 0$ (10^{-6} degrees) provided that the double precision arithmetic is used for calculations.

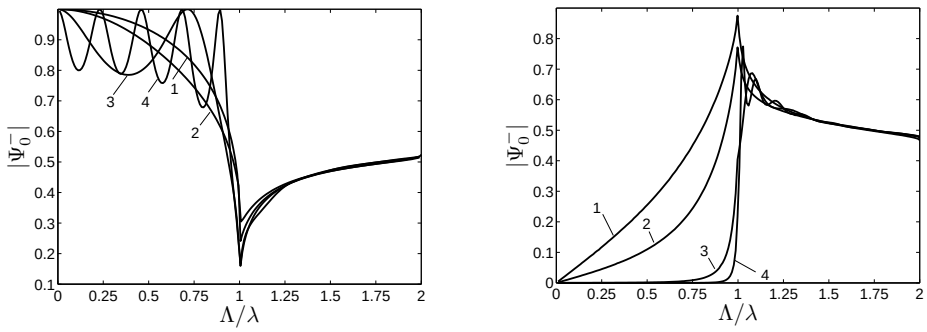

Figure 6.7. Dependence of the transmission coefficient Ψ_0^- versus Λ/λ for normal incidence and $d = \Lambda/2$, (a) TM and (b) TE polarization; the values of h are fixed: 1–$h = 0$, 2–$h = \Lambda/20$, 3–$h = \Lambda/2$, 4–$h = 2\Lambda$.

6.2. Electrostatics of strips with broken periodicity

In this Section another example of application of the suitably generalized BIS-expansion method is presented. Namely, a planar system of conducting strips with broken periodicity applied in electrostatic analysis is considered. The considered structure (see Fig. 6.8) results from a periodic system by inclusion of certain narrower strip and spacing in the middle of it and is also referred as a 'quasi-periodic' system. Far from this inclusion it remains "periodic", although the positions of strips and spacings at the left-hand side of the inclusion are interchanged with respect to the original periodic structure. The defective

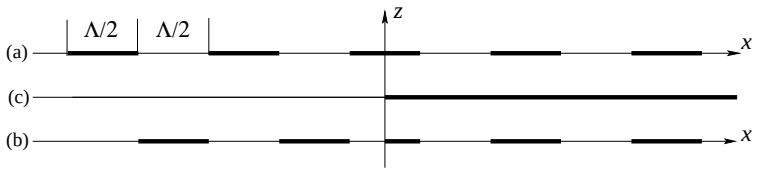

Figure 6.8. A periodic system of strips (a), and its quasi-periodic counterpart (b). E_z takes real values on strips (thick lines), and E_x is real in the other domains. The position of the conducting half-plane discussed in Sec. 2.1. is shown in (c).

periodic structures are known in physics; they are used in the Fabry-Perot resonators of solid-state lasers, for instance. Two distributed reflectors (which are periodic structures) are placed there at certain distance (a cavity region), usually of $\Lambda/2 + n\Lambda$ length, where Λ is the structural period of the reflectors. In

the considered system of strips, this cavity region is $\Lambda/2$ wide where Λ is the strip period.

The basic solution for the electric field in periodic system of strips arranged on the plane $z = 0$ plane was derived in the Section 2.2., Eq. (2.18), and the corresponding complex field function is given by Eq. (2.20) and Eq. (2.21) in spatial and spectral domains, respectively. On the other hand, the basic electrostatic solution for the half-plane $x > 0$ is given by Eq. (2.7), the complex field function being defined by Eq. (2.8) in the Section 2.1. The product of two complex field functions given by Eq. (2.18) and Eq. (2.8) is also a valid solution for certain electrostatic problem, like the product of two laterally shifted functions defined by Eq. (2.8) resulting in the solution for a strip, (see Section 2.3., Eq. (2.63)). This is because the product of analytic functions is an analytic one, hence describing certain electrostatic field (this can be easily checked by inspection). Thus, multiplication of Eq. (2.18) and Eq. (2.8) yields a basic solution for the quasi-periodic system of strips, shown in Fig. 6.8(b)

$$\Phi(x) = \Phi_p(x)\Phi_h(x), \tag{6.64}$$

where a new notation was introduced for convenience; Φ_p denotes the solutions for periodic system given by Eq. (2.20) and $\Phi_h(x)$ is the solution for the half-plane, Eq. (2.8). It results from Eq. (2.3) that the normal induction $D(x)$ evaluated form the corresponding complex field $\Phi(x)$ given by Eq. (6.64) using Eq. (2.8) remains real-valued in the same domains of $x > 0$ because of the real-valued $1/\sqrt{x}$. On the other hand, for $x < 0$ the value of $1/\sqrt{x}$ is imaginary causing that the domains of real and imaginary values of the complex field $\Phi(x)$, given by Eq. (6.64), are interchanged with respect to the corresponding field of periodic system. Therefore, the electric field components correspond to the system of strips shown in Fig. 6.8(b). It should be noted that the original strip placed at $x = 0$ is divided: its part placed at $x > 0$ remains the strip where $E(x) = 0$ and $D(x) \neq 0$, and the other part placed at $x < 0$ becomes the spacing, where $E(x) \neq 0$ and $D(x) = 0$. Therefore, the system is no longer periodic, but quasi-periodic, because outside this perturbation at $x \approx 0$ the remaining strips are 'periodic'. The spectral representation of the $\Phi(x)$ for the considered system is a convolution of two spectral functions $\Phi_p(\xi)$ and $\Phi_h(\xi)$:

$$\Phi(\xi) = \Phi_p(\xi) * \Phi_h(\xi), \tag{6.65}$$

where ξ is the spatial spectral variable corresponding to the x spatial coordinate. Due to the half-finite support of both spectral functions and simple form of $\Phi_p(\xi)$ given by Eq. (2.21) and $\Phi_h(\xi)$ given by Eq. (2.8), the convolution can be easily

evaluated [58], as presented below schematically:

$$\int_0^p \frac{P_{\lfloor\eta\rfloor}}{\sqrt{p-\eta}}d\eta = \sum_{n=0}^{\lfloor p\rfloor-1} 2P_n\left(-\sqrt{p-n-\eta}\right)\Big|_0^1 + \int_{\lfloor p\rfloor}^p \frac{P_{\lfloor p\rfloor}}{\sqrt{p-\eta}}d\eta,$$

where $p=\xi/K$, $K=2\pi/\Lambda$. This yields for the $\Phi(\xi)$:

$$\Phi(\xi) = \frac{4(1+j)}{\sqrt{\Lambda}}\left(\sum_{n=0}^{\lfloor p\rfloor-1}\frac{P_n}{\sqrt{p-n}+\sqrt{p-n-1}} + P_{\lfloor p\rfloor}\sqrt{p-\lfloor p\rfloor}\right), \qquad (6.66)$$

from which the spectral representations of the field components $E(\xi)$ and $D(\xi)$ can be easily evaluated using Eq. (2.11). The integration of the field in spatial domain corresponds to division by ξ in spectral domain.

The solution for arbitrary distribution of strip potentials along the system can be obtained using the same technique discussed in the Section 2.2., Eq. (2.33). To this end the complex field $\Phi(x)$ in Eq. (6.64) must be multiplied by arbitrary real-valued function $\alpha(x)$ having its spectral representation closed within domain $\xi\in(0,K)$:

$$\Phi(x)=\alpha(x)\Phi_p(x)\Phi_h(x) \Rightarrow \Phi(\xi)=\alpha(\xi)*\Phi_p(\xi)*\Phi_h(\xi). \qquad (6.67)$$

Particularly, for $\alpha(\xi)=1$, $\xi\in(0,K)$, the function $\Phi(x)$ has its spatial spectrum distributed over the entire positive semi-axis $\xi>0$ (Fig.6.9).

In general case arbitrary function $\alpha(\xi)$ can be conveniently approximated by a step function taking constant values in subsequent sub-domains. For instance, the series of Walsh functions can be used, which take constant values α_i on the sub-intervals $((i-1)\kappa<\xi\le i\kappa)$ of the domain $(0,K)$, where $\kappa=K/M$, $i=1\ldots M$; M is the number of applied sub-intervals. This enables one to evaluate the convolution integrals like in Eq. (6.66), which corresponds to the function $\alpha(\xi)$ taking unitary value in the entire domain $\xi\in(0,K)$. In a similar manner as in Eq. (6.66) (which corresponds to the case of $M=1$), each component of $\alpha(\xi)$ contributes to the convolution integral in the following way:

$$\int_{\frac{i}{M}}^{\frac{i+1}{M}} \frac{\alpha_i P_{\lfloor\eta\rfloor}}{\sqrt{p-\eta}}\,d\eta = 2\alpha_i\sum_{n=0}^{\lfloor p\rfloor-1} P_n\left(-\sqrt{p-n-\eta}\right)\Big|_{\frac{i}{M}}^{\frac{i+1}{M}} + \int_{\lfloor p\rfloor+\frac{i}{M}}^{b}\frac{\alpha_i P_{\lfloor p\rfloor}}{\sqrt{p-\eta}}\,d\eta, \qquad (6.68)$$

where the second integral appears in the equation only if $\xi>\lfloor p\rfloor+i/M$, in which case $b=\min(\xi,\lfloor p\rfloor+(i+1)/M)$. Also note that the first component (the sum)

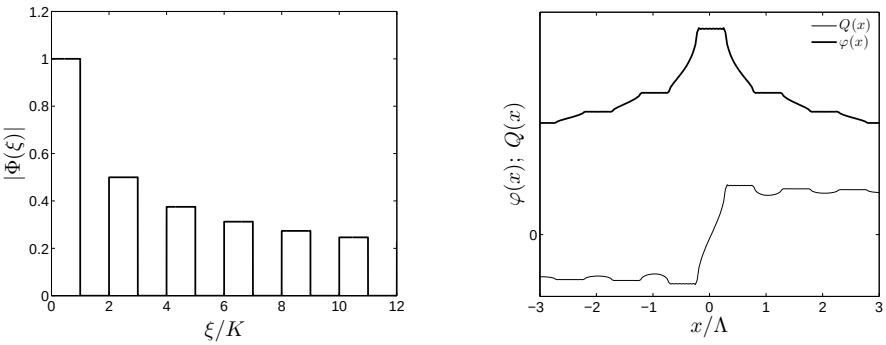

(a) (b)

Figure 6.9. (a) The applied spectral function $|\Phi_p(\xi)|$ for periodic system of planar strips. (b) The spatial distribution of electric potential $\varphi(x)$ (thick line); thin line presents the spatial charge distribution $Q(x)$.

disappears if $\lfloor p \rfloor = 0$. The above discussion presents how the functions $\Phi^{(i)}(\xi)$ can be obtained for each α_i and for any value of $\xi = \xi_n = n\kappa, n = 0 \ldots N-1$ used in computations, with adequate small κ (correspondingly large number M of Walsh functions involved in approximation of $\alpha(\xi)$) and sufficiently large N required by the numerical FFT algorithm. In the final form $\Phi(\xi)$ is given by a series:

$$\Phi(\xi) = \sum_{i=0}^{M-1} \alpha_i \Phi^{(i)}(\xi), \tag{6.69}$$

truncated here to finite M. In the numerical analysis the truncated function is represented by its values at discrete points $\xi_n = n\kappa$, $n = 0 \ldots N-1$ (typically, N is an integer power of 2 for the purpose of FFT algorithm), yielding a numerical vector of data Φ_n:

$$\Phi_n = \sum_{i=0}^{M-1} \alpha_i \Phi_n^{(i)},\ \Phi_n^{(i)} = \Phi^{(i)}(\xi_n). \tag{6.70}$$

It results from Eq. (6.68) that $\Phi^{(i)}(0) = 0$ hence $\Phi_0 = 0$. Applying Eq. (2.11), one easily obtains the analogous vector data of length $2N$ for electric field $E(\xi_n)$, $n = -N \ldots N-1$, and similarly for $D(\xi_n)$. Taking into account that

$$E(x) = -\partial\varphi/\partial x \Rightarrow E(\xi) = j\xi\varphi(\xi), \tag{6.71}$$

where φ is the electric potential distribution in the plane of strips $z = 0$, the strip potentials can be evaluated with the help of FFT algorithm in a similar

manner as discussed in the Section 2.3.:

$$[\varphi_n] = \alpha_i \mathrm{FFT}\{[-jE(\xi_n)/\xi_n]\},\ \Phi_0/\xi_0 \to 0, \tag{6.72}$$

where the numerical data vectors are denoted by $[\cdot]$. The evaluated φ_n are the potentials at discrete spatial points $x \sim n(N\kappa)^{-1}$ in the plane of strips. Let m denote these values of n corresponding to the points nearest to the centers of strips. The immediate verification of the computation accuracy, depending on both κ and N, is whether $\varphi_n = \text{const}$ on strips (certain violation of this condition cannot be avoided at the strip edges even for the smallest κ and largest N possible due to the known Gibbs phenomenon). The values of α_i is obtained by solving the above equation from the constraints that the φ_m takes given values (in the m^{th} strip's center).

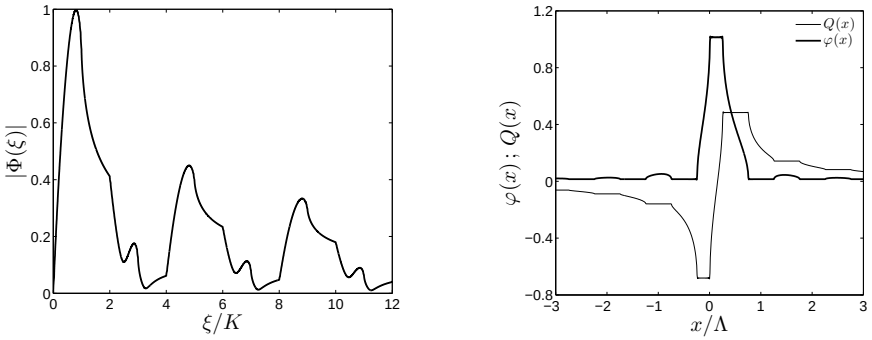

(a) (b)

Figure 6.10. (a) The evaluated spectrum $|\Phi(\xi)|$, and (b) the spatial distribution of electric potential $\varphi(x)$ (solid line); thin line presents the spatial charge distribution $Q(x)$.

In Fig. 6.10 the numerical example is shown for the case when the unity potential is given only to the narrow strip at $x \in (0, \Lambda/4)$; the other strips are assumed grounded. The results shown in Fig. 6.10(a) present both $\Phi(\xi)$ and $\varphi(x)$. The constant values of the potential on strips (thick line) can be easily noticed, as well as good accuracy concerning the strip voltages. In the presented examples the following values of parameters were used: $\Lambda = 1$, $M = 2^5$ and $\kappa = 2\pi/32$, $N = 2^{16}$. Computations show that the evaluated strip potentials vanishes fast for farther strips from the system center. This justifies the above mentioned truncation of the vector of unknowns α_i. The thin line presents the spatial charge distribution being the integral of $2\epsilon_0 D(x)$.

7

Conclusion

Electrostatics of planar systems of conducting strips is a problem of fundamental importance in the theory of surface acoustic wave (SAW) devices. Particularly, the interdigital transducer [59], which are widely used for the surface acoustic wave generation, detection and scattering in a variety of SAW devices, including delay lines, band-pass filters (these are the key components of the terminals and base stations of mobile radio networks, satellite receivers, multimedia equipment etc.) can be wholly characterized by the spatial spectrum (spatial Fourier transform) of the electric charge distribution on the surface of its electrodes. It is defined as a jump discontinuity of the normal electric induction on the surface of conducting body (planar system of conducting strips, modeling the transducer). It directly results from the solution of the classical boundary value problem formulated for electric field or its potential, governed by the Laplace equation, and the boundary conditions defined on the surface of the conducting body and in the general case a numerical solution can be obtained for example as discussed in [31]. In the particular case of the planar system of conducting strips, which was of main concern in this study, also the analytical solution can be obtained using approach exploiting the theory of complex functions [32, 129, 130]. Both these methods allow to find the electric charge distribution on the surface of conducting body - conducting strips. For instance, in the case of N strips the charge distribution is:

$$\sigma(x) = \begin{cases} \dfrac{\epsilon \sum_{m=0}^{N-2} (-1)^{m+N} \alpha_m x^m}{\sqrt{\prod_{n=1}^{N} |(x - x_{2n-1})(x - x_{2n})|}}, & x \text{ on strips}, \\ 0, & \text{otherwise}, \end{cases} \tag{7.1}$$

where (x_{2n-1}, x_{2n}) are the n^{th} strip's edge positions on the x-axis and α_m are some unknown coefficients which can be determined from the circuits con-

straints. The corresponding charge spatial spectrum evaluated by direct Fourier transform gives rise to a serious numerical problems due to the square-root singularity of the charge distribution on strips. For example, attempting to perform the Fourier transformation using the fast Fourier transform (FFT) algorithm, one has to sample the singular field at discrete values of the spatial variable. Due to the charge singularities at the strip edges and strong dependence of the spectrum on the distribution details over the entire system, the direct application of the Fourier transformation to the charge spatial distribution yields results with unsatisfactory accuracy (even if the field is perfectly evaluated [63, 131]). To overcome this difficulty, another approach, called the 'spectral approach' is favorable which evaluates the charge spatial spectrum directly, formally without any earlier evaluation of the spatial charge distribution and subsequent application of the FFT algorithm. The spatial field distributions are only necessary for evaluation of the strip potential and charge integrals in order to formulate the equations resulting from the circuit theory (the Kirchhoff's laws), taking into account that some strips have given potentials, others can be isolated or interconnected, yielding the conditions for the strips total charges. In fact, several independent solutions, called the 'template' solutions or 'template functions' (in the case finite aperiodic system of strips) for the spatial spectrum of electric charge can be constructed for given strip system. In the case of planar system of periodic strips having arbitrary potentials or charge distributions, the spectrum can be obtained using the so-called generalized BIS-expansion method [34], [37]. Here the 'template' solutions are defined in the form of a series of spatial harmonics with the coefficients further expanded in a series of the properly chosen Legendre polynomials (see discussion in the Section 2.2.1.). In this case the spectral representation of the 'template functions' is given by expression:

$$\Phi^m(\xi) = P_{\lfloor \xi/K \rfloor - m}(\cos\Delta),\ \xi \geq 0, \tag{7.2}$$

where $K = 2\pi/\Lambda$ is the spatial wave-number of the Λ-periodic system; $\Delta = Kd$, d being the strip width. In turn for a finite system of strips of arbitrary width and spacing a set of 'template functions', being multiple convolutions of the 0^{th} and 1^{th} order Bessel functions of the first kind, can be defined [38] (see discussion in the Section 2.3.) in the spectral domain directly:

$$\Phi^{(N,m)}(\xi) = \Phi'_1(\xi) * \cdots * \Phi'_m(\xi) * \Phi_{m+1}(\xi) * \cdots * \Phi_N(\xi), \tag{7.3}$$

where

$$\begin{aligned} \Phi_i(\xi) &= J_0(\xi d_i)\, e^{j\xi b_i},\ \xi \geq 0, \\ \Phi'_i(\xi) &= -j[\delta(\xi) - \xi_i J_1(\xi d_i)]\, e^{j\xi b_i},\ \xi \geq 0. \end{aligned} \tag{7.4}$$

In the above d_i and b_i are the i^{th} strip's half-width and center position on the x-axis.

A general solution in spatial spectrum domain is given by a superposition of finite number of 'template functions' both for finite aperiodic and infinite periodic systems of strips. In the case of feasible system of N strips having vanishing net charge there are $N-1$ terms in the linear combination (see Eq. (2.77)). A corresponding system of linear equations can be constructed using the circuit constraints (see discussion in the Section 2.3.) to find unknown real-valued coefficients. And as concerns a periodic system of strips, the BIS-expansion approximation (see Eq. (2.50)) can be used to obtain a finite linear combination of 'template function' representing a solution also in this case. The system of linear equations for unknown coefficients is obtain in a similar manner (see Eqs. (2.55) and (2.62) and corresponding discussion in the Section 2.2.1.). The field spatial distribution is often the least important in applications (measured are either the mutual strip capacitances depending on the total strip charges (the integrals of the charge distribution), or the spatial spectrum (in the scattering cases, like the Bragg scattering by strips or frequency characteristics of surface wave transducers)). Having the spatial spectrum, one can easily evaluate the spatial distribution and its integral (in order to evaluate the measured total charges of strips) with similar high accuracy, what is not true in the reverse way. The inverse Fourier transformation yields the tool for verification of the spectral results, lacking in the standard analysis [132–134]. Moreover, the feature of high importance in the numerical analysis is the semi-finite support of the spectral representations of 'template solutions'. This simplifies evaluation of multiple convolutions in Eq. (7.3) in particular. However, the main advantage of the 'spectral approach' worked out in the electrostatic theory of planar systems of conducting strips is its versatility and flexibility. Namely, it allows further successful extension over a wide range of the wave generation and scattering problems of different nature. In this study the main attention was focused on the acoustic phenomena. Specifically, the emphasis was put on generalization of the above electrostatic methods for solving the problems of acoustic wave generation and scattering by planar structures used in beam-forming applications. To this end the mixed boundary-value problem for planar system of rigid baffles was formulated. The following boundary conditions were specified on the plane of baffles: the normal component of particle velocity field vanishes on baffles and the pressure is given constant values in the case of wave generation problem. In the case of acoustic wave scattering the pressure vanishes between baffles and the pressure exerted by the incident and scattered waves on the acoustically hard baffles models the response signal from the individual piezoelectric elements of

the array transducer. Generalization of the BIS-expansion method (see discussion in the Section 2.2.1.) made it possible to solve the problem of acoustic wave generation and scattering in the case of infinite periodic baffle array. Similarly as in the electrostatic analysis, application of the BIS-expansion approximation (see Eq. (3.12)) results in a small system of linear equations which can be solved numerically:

$$\begin{aligned}
&\sum_m \alpha_m [g(r+nK)S_{n-m} - g_\infty] P_{n-m}(\cos\Delta) = 2g(r+nK)q^I\delta_{nI}, \\
&\sum_m (-1)^m \alpha_m P_{-r/K-m}(-\cos\Delta) = j\frac{K}{\pi}\, p_l\, e^{jrl\Lambda} \sin \pi r/K, \\
&n \in [-N, N]\,,\ m \in [-N, N+1]\,,
\end{aligned} \tag{7.5}$$

where $g(r+nK)$ is the harmonic admittance given by Eq. (3.3) and g_∞ is defined in Eq. (3.4).

Specifying arbitrary aperiodic constant (complex in general case) amplitudes p_l of the pressure in the slots between baffles one can easily evaluate the spatial distribution of the generated wave-field in the acoustic media using the solution for spatial spectrum of the pressure distribution on the baffle plane. The far-field radiation pattern also results immediately. To this end the stationary phase method, for example, can be used to evaluate certain fast varying integrals (see discussion in the Section 3.2.) yielding the angular radiation characteristics of the baffle array with arbitrary aperiodic excitation:

$$p_R(\theta) \sim p(k\sin\theta)\cos\theta, \tag{7.6}$$

where $p(\cdot)$ is the spatial spectrum of pressure distribution on the baffle plane. The wave scattering problem was approached by the method for the plane harmonic acoustic wave incidence without any loss of generality. In the case of arbitrary non-planar incident wave, its spatial Fourier expansion on the plane of baffles should be applied instead, and certain wider domain (dependent on particular application) of the spatial spectral variable must be included in the analysis of such non-plane incident wave. Numerous examples presented in the Section 3.2. confirm that the applied generalization of electrostatic BIS-expansion method is worth consideration for numerical experiments concerning the beam-forming systems. It is very efficient numerically, yielding all interesting characteristics of the system within the same simple analysis. Using the BIS-expansion approximation (see Eq. (3.12)) the problem is reduced to solving the system of linear equations given by Eq. (7.5). In beam-forming applications usually $k \sim K$ (k - the acoustic wave-number; K - the spatial wave-number

of the baffle array) is relevant. As discussed in the Section 3.2. in this case applying $N \sim 10$ in the BIS-expansion approximation yields the results with sufficient accuracy for practical applications. Moreover, the energy conservation law is satisfied (with machine accuracy [36, 39]), which is the valuable feature allowing one to check the computed results easily. The system of linear equation (dependent on $r \in (0, K)$, see Eq. (7.5)), is generally well-conditioned, except the case $r \to 0$ or $r \to K$. This is illustrated in the Fig. 7.1 where the dependence of the matrix condition number for $N = 16$ (the value applied in the numerical results presented in the Section 3.2.) versus the r/K is shown. In the proximity of 0 and K, the values $r = 10^{-4}k$ and $r = K - 10^{-4}k$ were used in the numerical computations, in order to avoid evaluation of the corresponding limits [39] (see also discussion at the end of the Section 3.2.2.).

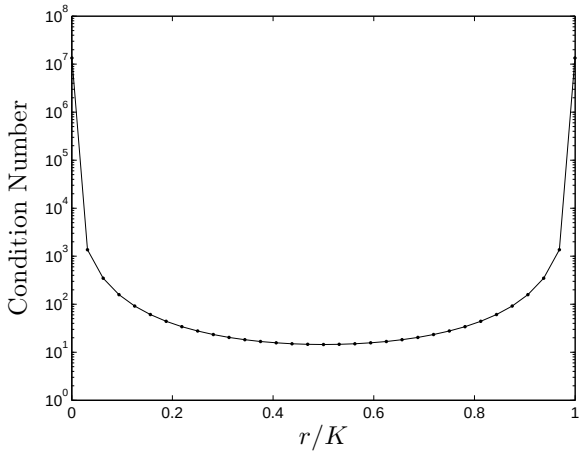

Figure 7.1. Dependence of the condition number of the matrix of system of linear equations, Eq. (7.5) for $N = 16$ (34×34 matrix size) versus r/K. In the example $\Lambda/\lambda = 1$; $d/\Lambda = 0.75$, d being slot width.

Evidently, for the considered 34×34 matrix the condition number is $\sim 10^2$ in the entire domain of $r \in (0, K)$, except the boundaries, where it growth to $\sim 10^7$. But even in this cases the system of equations can be efficiently solved using the double-precision arithmetics and the singular value decomposition (SVD) algorithm [65]. In Fig. 7.2 the relative error in power relation δP versus r/K is shown for the same parameters Λ/λ as above. The δP is defined as follows:

$$\delta P = \frac{|\Pi_z - P|}{P} * 100\%,$$

where Π_z and P are the total power radiated from the baffle plane and the delivered power defined by Eq. (3.23) and Eq. (3.25), respectively. As shown in Fig. 7.2 the energy conservation law is satisfied accurately for $N = 16$ and the relative error $\delta P \sim 10^{-10}$ in the entire domain of $r \in (0, K)$, as expected (see discussion in the Section 3.2.1.). This evidences the numerical efficiency of the BIS-expansion method in acoustic beam-forming applications, discussed in the following.

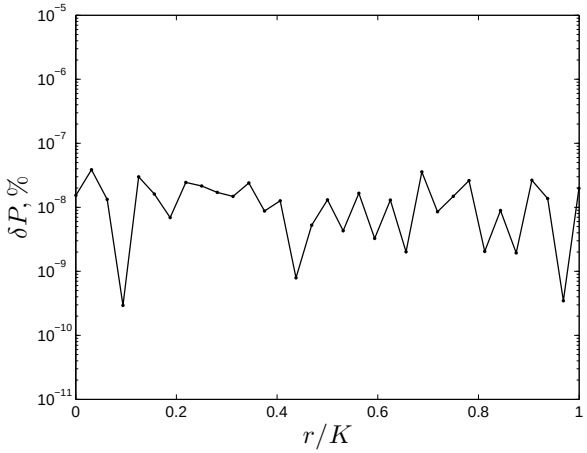

Figure 7.2. Dependence of the relative error in power relation δP for $N = 16$ (34×34 matrix size) versus r/K. In the example $\Lambda/\lambda = 1$; $d/\Lambda = 0.75$, d being slot width.

Further generalization of the BIS-expansion method (applicable for periodic arrays) and the 'template functions' approach (applicable for the finite system of strips of arbitrary width and spacing) allowed to worked out the method of analysis of the acoustic wave generation problem by a finite array of rigid baffles (see discussion in the Section 3.3.). To this end the initial system was considered as a single cell of certain multi-periodic system with large (tending to infinity) but finite period. Application of the approximation made possible generalization of the results of electrostatic analysis concerning the finite system of conducting strips in external spatially harmonic electric field, discussed in details in the Section 2.4. This allowed to construct the solution as superposition of 'template functions' obtained from the basis one:

$$\Phi^{(N)}(\xi) = \Phi_1(\xi) * \Phi_2(\xi) * \cdots * \Phi_N(\xi), \tag{7.7}$$

defined in electrostatics of finite system of strips (see Eqs. (7.3) and (7.4)) by simple index shift (discrete series of samples in spatial spectrum domain in the

applied numerical analysis as discussed in details in the Section 3.3., Eq. (3.36) through Eq. (3.38)). This is analogous to discrete convolution with certain functions whose spectral representation yields the unknown coefficients of the linear combination. Using the BIS-expansion approximation (see Eq. 3.41) the problem was reduced to numerical solving of certain system of linear equations for the above unknowns:

$$\begin{aligned} & g_\infty \sum_m \alpha_m [S_{n-m} - j(\eta_n/\xi_n)] Q_{n-m}^{(N)} = 0,\ n \in [-N_1, N_1], \\ & \sum_m \alpha_m \mathcal{F}^{-1} \left\{ Q_{l-m}^{(N)}/\xi_l \right\} = p_i, i \in [1, N_s]\,,\ n \in [N_1+1, N_1+N_s] \\ & m \in [-N_1 - M_l, N_1 + M_u]\,,\ l \in [-L, L-1]\,, \end{aligned} \tag{7.8}$$

where N_s is the number of active slots with given constant pressures p_i, and M_u, M_l are some integers dependent on N_s: $M_u + M_l = N_s$ (see discussion in the Section 3.3.). In the above $\xi_i = i\Delta\xi$ is the spectral variable evaluated at discrete points with sampling interval $\Delta\xi$, directly related to the period of the above multi-periodic system $\Delta\xi = 2\pi/\Lambda$. Generally, the larger Λ/P, the finer the multi-periodic approximation. For the number of baffles $N = 10 \div 20$ it is sufficient to apply $\Lambda/P \approx 10^2$, which yields $N_1 \sim 10^3$ for $k \sim 2\pi/P$ in Eq. (7.8) (see discussion in the Section 3.3.1.) and approximately $2N_1$ unknown coefficients α_m to be determined. In this case for evaluation of integrals representing the pressure on the plane of baffles by means of the inverse Fourier transform (computed using FFT algorithm), the 'template functions' should be evaluated within the spatial spectrum domain bounded by the upper frequency $\xi_u' \approx 50k$ [38, 63]. This yields $L \sim 2^{13}$ samples in corresponding data-sets in Eq. (7.8). It should be noted, that here the advantage was taken of the semi-finite support of the spectral representation of the 'template functions' (see Eqs. (7.7) and (7.4)). Generally, for accurate evaluation of the multiple convolutions in Eqs. (7.3) and (7.7) the advanced numerical algorithms developed in [63] for analysis of electrostatic problem for finite system of conducting strips can be used (see also discussion in Section 2.3.). However, for larger number of baffles, $N = 35 \div 40$, to maintain the same accuracy of integral evaluation in Eq. (7.8), the data-sets representing the 'template functions' should be evaluated with the step $\Delta\xi$ quartered, at least, within the same domain $(0, \xi_u')$ [63]. This yields $L \sim 2^{15}$ samples in the data-sets in Eq. (7.8). Decrease of the sampling step $\Delta\xi$ also results in increase of $\Lambda \approx 5 \cdot 10^2 P$, which, in turn, yields $N_1 \approx 5 \cdot 10^3$ in Eq. (7.8). Moreover, the resulting system of linear equations, Eq. (7.8), become bad-conditioned as the number of elements in the baffle array grows. This is illustrated in Fig. 7.3 where a condition number of the matrix of the system of

equations is shown versus the number of active slots N_s. Evidently, for baffle array comprising up to 20 elements the condition number is approximately within bounds $10^{12} \div 10^{14}$ and the corresponding system of equations can be solved using, for example, the singular value decomposition (SVD) method [63, 65]. The limitations connected with evaluation of multiple convolutions in Eq. (7.7) and bad-conditioning of the system given by Eq. (7.8), however, restrict application of this method to small systems consisting of about $10 \div 20$ baffles, which is far insufficient to meet the needs of modeling of the modern practical transducer arrays used in ultrasound applications.

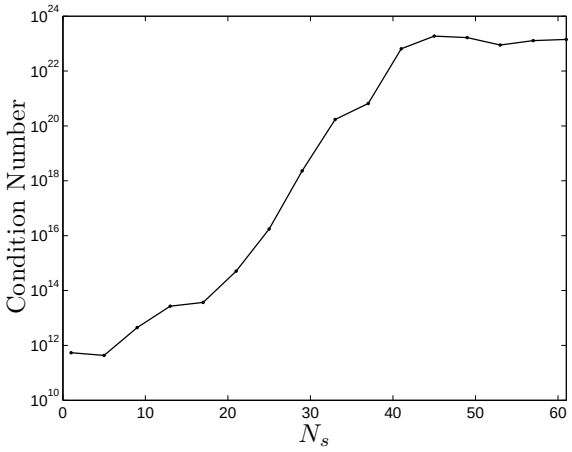

Figure 7.3. Dependence of the condition number of the matrix of system of linear equations, Eq. (7.8) versus the number of active slots N_s. In the example $\Lambda/\lambda = 1$; $d/\Lambda = 0.75$, d being slot width.

Nevertheless, it presents original and uncommon theoretical approach to solving the acoustic beam-forming problem for finite baffle system. On the other hand, the modern ultrasound transducer arrays, comprised at least of 128 elements, can be successfully approximated by a periodic system of baffles and modeled with sufficient accuracy using the generalized BIS-expansion method, worked out and discussed in details in the Section 3.2. This was well illustrated in the Chapter 4 where this method was used to improve the performance of the Multi-element Synthetic Transmit Aperture (MSTA) ultrasound imaging technique exploiting the principles of synthetic aperture. The modified MSTA method (see discussion in the Chapter 4) is based on the coherent summation of the received backscattered echo signals with weights which account for the

finite size of the transmit and receive apertures:

$$S^{mod}_{MSTA}(r,\theta) = \sum_{m=1}^{M}\sum_{n=1}^{N} w_{mn} s_{m,n}\left(\frac{2r}{c} - \tau_{m,n}\right), \tag{7.9}$$

where $s_{m,n}$ are back-scattered echo signals corresponding to m^{th} transmit and n^{th} receive apertures, delayed properly by $\tau_{m,n}$ (see discussion in the Chapter 4). The apodization weights w_{mn} were calculated for each imaging point and all combinations of the transmit-receive pairs using their angular directivity functions:

$$w_{mn} = f_T(\theta_m) f_R(\theta_n),\ \theta_i = \theta_i(r,\theta),\ i = m,n, \tag{7.10}$$

denoted by the superscripts T and R, respectively. To this end the results of the analysis of the mixed boundary-value problem for periodic baffle array, discussed in details in the Section 3.2., where used with great success. Specifically, the far-field radiation pattern, given by Eq. (7.6) was used for the purpose of apodization weights evaluation, as discussed in details in the Chapter 4. This allowed to develop a new and efficient imaging algorithm which improves considerably the imaging quality, especially in the immediate vicinity of the transducer surface. More specifically, the hazy blurring artifacts observable in the images obtained using conventional MSTA algorithm were substantially suppressed due to the directivity weights applied in the modified MSTA. Moreover, an increase in the visualization depth was demonstrated at the cost of slight degradation of the lateral resolution, which degradation, however, decreased with increasing penetration depth, as evidenced in the Chapter 4. The developed modified MSTA algorithm is an important contribution to the nowadays imaging techniques used in the modern ultrasound scanners for real-time imaging applications. It proves to be well suited for clinical examinations, especially in the applications where the quality of the "near-field" image, that is the image in the immediate vicinity of the scanhead is of critical importance such as for instance in skin- and breast-examinations. The presented method is now being further investigated and implemented within the framework of ongoing project designed to develop a research ultrasound imaging platform.

The acoustic beam-forming analysis related to the linear transducer arrays is not the only problem which can be approached by the methods of electrostatics discussed above. They proved to be suited for analysis of the doubly periodic structures as demonstrated in the Chapter 5, where a novel 2D transducer array geometry was examined. It is comprised of crossed periodic metal

electrodes placed on both sides of electrostrictive layer which represent the rows and columns of 2D beam-forming matrix. Such a system has potential capability of electronic beam-steering of generated wave both in elevation and azimuth as required for fast volumetric imaging in modern ultrasound scanners. The wave-beam control can be achieved by addressable driving of 2D matrix transducer through proper voltage supply of electrodes on opposite surfaces of the layer. A proper generalization of the BIS-expansion method (see discussion in the Section 2.2.1.) allowed to extend it to the case of doubly periodic structures and enabled development of an efficient semi-analytical method of analysis of the considered problem. The obtained results are being subjected to further generalization for the case of doubly periodic crossed-electrode array on thin periodic layer within the framework of ongoing research project connected with development and design of 2D planar transducer array for application in volumetric ultrasound imaging.

Finally, some non-acoustic extensions and applications of the generalized BIS-expansion method were presented in the Chapter 6. Specifically, the problems of electromagnetic wave scattering by periodic gratings like thick-walled parallel-plate waveguide array and periodic system of conducting electrodes of finite thickness were considered in the Section 6.1. The developed methods of analysis represent original and valuable contribution to the theoretical modeling of the waveguiding structures which are widely used in many practical applications. Moreover, these extensions illustrate well and prove the suitability and versatility of the considered electrostatic methods, which were successfully generalized for efficient solving the variety of wave generation and scattering problems of different physical nature related to planar and non-planar, periodic and finite aperiodic arrangements of elements - the arrays.

Bibliography

1. K. E. Thomenius. Evolution of ultrasound beamformers. *Proc. 1996 IEEE Ultrason. Symp.*, pages 1615–1622, 1996.
2. R. J. Zemp, C. K. Abbey, and M. F. Insana. Linear system models for ultrasonic imaging: application to signal statistics. *IEEE Trans. Ultrason., Ferroelectr. Freq. Contr.*, 50(6):642–654, JUN 2003.
3. V. A. Kramb. Use of phased array ultrasonics for automated aerospace testing applications. *Materials Evaluation*, 65(1):67–73, JAN 2007.
4. J. D. Buttram. Manual ultrasonic phased array technique for accurate through- wall sizing of planar discontinuities in dissimilar metal welds. *Materials Evaluation*, 65:62–66, 2007.
5. B. W. Drinkwater and P. D. Wilcox. Ultrasonic arrays for non-destructive evaluation: A review. *NDT & E International*, 39(7):525–541, OCT 2006.
6. S. Chatillon, G. Cattiaux, M. Serre, and O. Roy. Ultrasonic non-destructive testing of pieces of complex geometry with a flexible array transducer. *Ultrasonics*, 38(1-8):131–134, MAR 2000.
7. S. Mahaut, O. Roy, C. Beroni, and B. Rotter. Development of phased array techniques to improve characterization of defect located in a component of complex geometry. *Ultrasonics*, 40(1-8):165–169, MAY 2002.
8. S. Chatillon, L. de Roumilly, J. Porre, C. Poidevin, and P. Calmon. Simulation and data reconstruction for ndt phased array techniques. *Ultrasonics*, 44:e951–e955, 2006.
9. R. Huang and L. W. Schmerr Jr. Characterization of the system functions of ultrasonic linear phased array inspection systems. *Ultrasonics*, 49(2):219–225, FEB 2009.
10. W. Rotman and R. Turner. Wide-angle microwave lens for line source applications. *IEEE Trans. Antennas Propagat.*, 11(6):623–632, JUN 1963.
11. P. S. Naidu. *Sensor Array Signal Processing.* CRC Press, Boca Raton, 2001.

12. E. Kuhnicke. Plane arrays - fundamental investigations for correct steering by means of sound field calculations. *Wave Motion*, 44(4):248–261, MAR 2007.
13. S. C. Wooh and Y. J. Shi. Influence of phased array element size on beam steering behavior. *Ultrasonics*, 36(6):737–749, APR 1998.
14. R. Y. Chiao and L. J. Thomas. Analytic evaluation of sampled aperture ultrasonic-imaging techniques for nde. *IEEE Trans. Ultrason., Ferroelectr. Freq. Contr.*, 41(4):484–493, JUL 1994.
15. R Ahmad, T Kundu, and D Placko. Modeling of phased array transducers. *J. Acoust. Soc. Am.*, 117(4):1762–1776, Part 1 APR 2005.
16. F. Lingvall, T. Olofsson, and T. Stepinski. Synthetic aperture imaging using sources with finite aperture: Deconvolution of the spatial impulse response. *J. Acoust. Soc. Am.*, 114(1):225–234, JUL 2003.
17. R Lerch. Simulation of piezoelectric devices by 2-dimensional and 3- dimensional finite-elements. *IEEE Trans. Ultrason., Ferroelectr. Freq. Contr.*, 37(3):233–247, MAY 1990.
18. G. G. Yaralioglu, A. S. Ergun, and B. T. Khuri-Yakub. Finite-element analysis of capacitive micromachined ultrasonic transducers. *IEEE Trans. Ultrason., Ferroelectr. Freq. Contr.*, 52(12):2185–2198, DEC 2005.
19. M. Wilm, R. Armati, W. Daniau, and S. Ballandras. Cross-talk phenomena in a 1-3 connectivity piezocomposite. *J. Acoust. Soc. Am.*, 116(5):2948–2955, MAY 2004.
20. A. McNab, A. Cochran, and M. A. Campbell. The calculation of acoustic fields in solids for transient normal surface sources of arbitrary geometry and apodisation. *J. Acoust. Soc. Am.*, 87(4):1455–1465, APR 1990.
21. A. McNab, A. Cochran, and M. A. Campbell. The calculation of acoustic fields in solids for transient normal surface sources of arbitrary geometry and apodisation. *J. Acoust. Soc. Am.*, 87(4):1455–1465, APR 1990.
22. S. C. Wooh and Y. Shi. Three-dimensional beam directivity of phase-steered ultrasound. *J. Acoust. Soc. Am.*, 105(6):3275–3282, JUN 1999.
23. B. Erbas and I. D. Abrahams. Scattering of sound waves by an infinite grating composed of rigid plates. *Wave Motion*, 44(4):282–303, MAR 2007.
24. J. D. Achenbach and Z. L. Li. Reflection and transmission of scalar waves by a periodic array of screens. *Wave Motion*, 8(3):225–234, MAY 1986.
25. E. J. Danicki. Electrostatics of interdigital transducers. *IEEE Trans. Ultrason., Ferroelectr. Freq. Contr.*, 51(4):444–452, APR 2004.

26. E. J. Danicki. Strip electrostatics - spectral approach. *Proc. 1996 IEEE Ultrason. Symp.*, pages 193–196, 1996.
27. Y. Tasinkevych. Methods of idt charge spatial spectrum evaluation. *J. Tech. Phys.*, 45:155–172, 2004.
28. J. Boersma and E. Danicki. On the solution of an integral equation arising in potential problems for circular and elliptic disks. *SIAM J. Appl. Math.*, 53(4):931–941, AUG 1993.
29. R. E. Collin. *Field theory of guided waves.* New York: McGraw-Hill, 1960.
30. D. S. Jones. *The Theory of Electromagnetism.* Pergamon Press, Oxford-London-New York-Paris, 1964.
31. N. G. Green, A. Ramos, and H. Morgan. Numerical solution of the dielectrophoretic and traveling wave forces for interdigitated electrode arrays using the finite element method. *J. Electrostatatics*, 56:235–254, 2002.
32. N. I. Mushelishvili. *Singular integral equations.* Moscow: Nauka, 1946.
33. Y. Tasinkevych. *Electrostatics: Theory and Applications*, chapter Electrostatics of planar system of conducting strips, pages 189–221. New York: Nova Science Pub Inc., 2011.
34. K. Blotekjaer, K. A. Ingebrigtsen, and H. Skeie. Methods for analyzing waves in structures consisting of metal strips on dispersive media. *IEEE Trans. Electron Devices*, ED20(12):1133–1138, 1973.
35. E. Danicki, B. Langli, and K. Blotekjaer. Spectral theory of em wave scattering by periodic strips. *IEEE Trans. Antennas Propagat.*, 43(1):97–104, 1995.
36. E. J. Danicki. Scattering by periodic cracks and theory of comb transducers. *Wave Motion*, 35(4):355–370, APR 2002.
37. E. J. Danicki and Y. Tasinkevych. Nonstandard electrostatic problem for strips. *J. Electrostatics*, 64(6):386–391, JUN 2006.
38. E. J. Danicki and Y. Tasinkevych. On electrostatics of finite system of strips applied in surface acoustic wave interdigital transducers. *J. Tech. Phys.*, 46:175–193, 2005.
39. E. J. Danicki. Resonant phenomena in bulk-wave scattering by in-plane periodic cracks. *J. Acoust. Soc. Am.*, 105(1):84–92, JAN 1999.
40. S. Holm. *Focused multi-element synthetic aperture imaging.* Department of Informatics, University of Oslo, 1995.
41. E. Danicki and Y. Tasinkevych. Beam-forming electrostrictive matrix. In *Proc. 31th Int. Conf. Acoustical Imaging*, pages 1–4, 2011.

42. Y. Tasinkevych. Scattering of h-polarized wave by a periodic array of thick-walled parallel plate waveguides. *IEEE Trans. Antennas Propagat.*, 56(10):3333–3337, OCT 2008.
43. Y. Tasinkevych. Em scattering by the parallel plate waveguide array with thick walls for oblique incidence. *J Electromagn. Waves Appl.*, 23(11-12):1611–1621, 2009.
44. Y. Tasinkevych. Electromagnetic scattering by periodic grating of pec bars. *J Electromagn. Waves Appl*, 25(5-6):641–650, 2011.
45. S. Peng and G. M. Morris. Experimental demonstration of resonant anomalies in diffraction from two-dimensional gratings. *Optics Letters*, 21(8):549–551, APR 1996.
46. S. Peng and G. M. Morris. Resonant scattering from two-dimensional gratings. *Journal of the Optical Society of America A-Optics Image Science and Vision*, 13(5):993–1005, MAY 1996.
47. C. M. Horwitz. New solar selective surface. *Opt. Commun.*, 11(2):210–212, 1974.
48. D. Sievenpiper, L. J. Zhang, R. F. J. Broas, N. G. Alexopolous, and E. Yablonovitch. High-impedance electromagnetic surfaces with a forbidden frequency band. *IEEE Transactions on Microwave Theory and Techniques*, 47(11):2059–2074, NOV 1999.
49. V. Veremey. Superdirective antennas with passive reflectors. *IEEE Antennas and Propagation Magazine*, 37(2):16–27, APR 1995.
50. CR Simovski and SL He. Antennas based on modified metallic photonic bandgap structures consisting of capacitively loaded wires. *Microw. Opt. Tech. Lett.*, 31(3):214–221, NOV 5 2001.
51. M. M. Sigalas, R. Biswas, K. M. Ho, C. M. Soukoulis, and D. D. Crouch. Waveguides in three-dimensional metallic photonic band-gap materials. *Phys. Rev. B*, 60(7):4426–4429, AUG 1999.
52. B. K. Minhas, W. Fan, K. Agi, S. R. J. Brueck, and K. J. Malloy. Metallic inductive and capacitive grids: theory and experiment. *Journal of the Optical Society of America A-Optics Image Science and Vision*, 19(7):1352–1359, JUL 2002.
53. L. Jelinek, R. Marques, F. Mesa, and J. D. Baena. Periodic arrangements of chiral scatterers providing negative refractive index bi-isotropic media. *Physical Review B*, 77(20):205110, May 2008.
54. C.-W. Kuo and S.-Y. Chen. Analyzing the multilayer optical planar waveguides with double-negative metamaterial. *PIERS*, 110:163–178, 2010.

55. B. Gimeno, J. L. Cruz, E. A. Navarro, and V. Such. Electromagnetic scattering by a strip grating with plane-wave 3-dimensional oblique-incidence by means of decomposition into e-type and h-type modes. *J Electromagn. Waves Appl.*, 7(9):1201–1219, 1993.
56. T. Kushta and K. Yasumoto. Electromagnetic scattering from periodic arrays of two circular cylinders per unit cell. *Journal of Electromagnetic Waves and Applications*, 14(6):853–854, 2000.
57. E. J. Danicki and Y. Tasinkevych. Electrostatics of quasiperiodic system of conducting strips. In *Proc. 17th Int. Conf. Microwaves, Radar and Wireless Communications MIKON 2008*, pages 1–4, 2008.
58. E. J. Danicki. *Spectral theory of interdigital transducers of surface acoustic waves*, chapter 3. http://www.ippt.gov.pl/∼edanicki/danickibook.pdf, 2006.
59. D. P. Morgan. *Surface acoustic wave devices*. Elsevier Science Publishers B. V., Amsterdam, 1991.
60. P. Moon and D. E. Spencer. *Field theory for engineers*. D. Van Nostrand Company Inc., Princeton, 1961.
61. R Mittra and S. W. Lee. *Analytical techniques in the theory of guided waves*. The Macmillan Company, 1971.
62. A. Erdelyi, W. Magnus, F. Oberhettinger, and F. G. Tricomi. *Higher Transcendental Functions*, volume 1, chapter 3, pages 166–167. McGraw-Hill, New York, 1953.
63. Y. Tasinkevych. *Numerical efficiency of interdigital transducers charge spatial spectrum evaluation methods*. PhD thesis, IFTR, Polish Acad. of Sci., Warsaw, 2004.
64. A. Erdelyi, W. Magnus, F. Oberhettinger, and F. G. Tricomi. *Higher Transcendental Functions*, volume 1, chapter 3, pages 144–145. McGraw-Hill, New York, 1953.
65. W. H. Press, S. A. Teukolsky, B. P. Vetterling, and B. P. Flannery. *Numerical Recipes in C. The art of scientific computing*. Cambridge University Press, second edition, 1992.
66. J. T. Yen, J. P. Steinberg, and S. W. Smith. Sparse 2-d array design for real time rectilinear volumetric imaging. *IEEE Trans. Ultrason., Ferroelectr. Freq. Contr.*, 47(1):93–110, JAN 2000.
67. C. H. Seo and J. T. Yen. 256x256 2-d array transducer with row-column addressing for 3-d imaging. *Proc. 2007 IEEE Ultrason. Symp.*, pages 2381–2384, 2007.

68. A. R. Selfridge, G. S. Kino, and B. T. Khuriyakub. A theory for the radiation pattern of a narrow-strip acoustic transducer. *Appl. Phys. Lett.*, 37(1):35–36, 1980.

69. J. A. Jensen and N. B. Svendsen. Calculation of pressure fields from arbitrary shaped, apodized, and excited ultrasound transducers. *IEEE Trans. Ultrason., Ferroelectr. Freq. Contr.*, 39(2):262 – 267, Mar. 1992.

70. P. Crombie, P. A. J. Bascom, and R. S. C. Cobbold. Calculating the pulsed response of linear arrays: Accuracy versus computational efficiency. *IEEE Trans. Ultrason., Ferroelectr. Freq. Contr.*, 44(5):997–1009, SEP 1997.

71. M. W. Fedoryuk. *The Steepest Descent Method*, chapter 3. Nauka, Moscow, 1997.

72. L. B. Felsen and N. Marcuvitz. *Radiation and Scattering of Waves*, volume 1, chapter 4. Prentice Hall, Englewood Cliffs, 1973.

73. J. W. Goodman. *Introduction to Fourier Optics*. New York: McGraw-Hill, 2005.

74. B. D. Steinberg. *Principles of aperture and array system design including random and adaptive arrays*. New York: John Wiley and Sons, 1976.

75. Ch. Cook and M. Bernfeld. *Radar Signals, An Introduction to Theory and Application*, chapter 7. Academic Press, New York, 1967.

76. Y. Tasinkevych. Wave generation by a finite baffle array in applications to beam-forming analysis. *Archives of Acoustics*, 35(4):677–686, 2010.

77. R. M. Perry and L. W. Martinson. *Radar matched filtering, Radar Technology*, chapter 11, page 163–169. Artech House, Boston, 1978.

78. A. Moreira. Real-time synthetic aperture radar (sar) processing with a new subaperture approach. *IEEE Trans. Geosci. Remote Sens.*, 30(4):714–722, 1992.

79. N. C. Yen and W. Carey. Application of synthetic aperture processing to towed-array data. *J. Acoust. Soc. Am.*, 86(2):754–765, 1989.

80. S. Stergiopoulos and E. J. Sullivan. Extended towed array processing by an overlap correlator. *J. Acoust. Soc. Am.*, 86(1):158–171, 1989.

81. K. Nagai. A new synthetic-aperture focusing method for ultrasonic b-scan imaging by the fourier transform. *IEEE Trans. Sonics Ultrason.*, 32(4):531–536, 1985.

82. R. N. Thomson. Transverse and longitudinal resolution of the synthetic aperture focusing technique. *Ultrasonics*, 22(1):9–15, 1984.

83. M. Karaman, Pai-Chi Li, and M. O'Donnell. Synthetic aperture imaging for small scale systems. *IEEE Trans. Ultrason., Ferroelectr. Freq. Contr.*, 42(3):429–442, 1995.

84. G. R. Lockwood, J. R. Talman, and S. S. Brunke. Real-time 3-d ultrasound imaging using sparse synthetic aperture beamforming. *IEEE Trans. Ultrason., Ferroelectr. Freq. Contr.*, 45(4):980–988, 1998.

85. I. Trots, A. Nowicki, and M. Lewandowski. Synthetic transmit aperture in ultrasound imaging. *Archives of Acoustics*, 34(4):685–695, 2009.

86. J. A. Jensen, S. I. Nikolov, K. L. Gammelmark, and M. H. Pedersen. Synthetic aperture ultrasound imaging. *Ultrasonics*, 44, Suppl.:e5–e15, 2006.

87. P. J. Thoen. Aperture apodization to reduce the o -axis intensity of the pulsed-mode directivity fucntion of linear arrays. *Ultrasonics*, 20(5):231–236, 1982.

88. C. M. W. Daft and W. E. Engeler. Windowing of wide-band ultrasound transducers. In *Proc. 1996 IEEE Ultrasonics Symp.*, volume 2, pages 1541–1544, 1996.

89. D. A. Guenther and W. F. Walker. Optimal apodization design for medical ultrasound using constrained least squares part ii simulation results. *IEEE Trans. Ultrason., Ferroelectr. Freq. Contr.*, 54(2):343–358, 2007.

90. J.-F. Synnevg, A. Austeng, and S. Holm. A low-complexity data-dependent beamformer. *IEEE Trans. Ultrason., Ferroelectr. Freq. Contr.*, 58(2):281–289, 2011.

91. S. Repetto and A. Trucco. A stochastic approach for the apodization of very short arrays. *Ultrasonics*, 42:425–429, 2004.

92. S. M. Sakhaei, A. Mahloojifar, and H. Ghassemian. A transformation based method to design ultrasound array. *Ultrasonics*, 49(2):179–184, 2009.

93. I. Trots, A. Nowicki, M. Lewandowski, and Y. Tasinkevych. Multi-element synthetic transmit aperture in medical ultrasound imaging. *Arch. Acoust.*, 35(4):687–699, 2010.

94. Y. Tasinkevych, I. Trots, A. Nowicki, and P. A. Lewin. Modified synthetic transmit aperture algorithm for ultrasound imaging. *Ultrasonics*, 52(2):333–342, 2012.

95. J. W. Goodman. *Introduction to Fourier Optics*, page 49. McGraw-Hill, Roberts and Company Publishers, 2005.

96. J. A. Jensen. Field: A program for simulating ultrasound systems. In *10th Nordic-Baltic Conference on Biomedical Imaging published in Medical & Biological Engineering & Computing*, volume 34, page 351–353, 1996.

97. http://fantom.dk/571.htm.

98. Y. Tasinkevych, I. Trots, and A. Nowicki. Optimization in the multi-element synthetic transmit aperture method for ultrasound imaging. In *Proc. 31th Conference "Acoustical Imaging"*, (in press), 2011.

99. S. W. Smith, Jr. Pavy, H. G., and O. T. von Ramm. High-speed ultrasound volumetric imaging system. i. transducer design and beam steering. *IEEE Trans. Ultrason., Ferroelectr. Freq. Contr.*, 38(2):100–108, 1991.

100. S. W. Smith, G. E. Trahey, and O. T. von Ramm. Two-dimensional arrays for medical ultrasound. In *Proc. 1991 IEEE Ultrasonics Symp.*, pages 625–628, 1991.

101. John W. Hunt, Marcel Arditi, and F. Stuart Foster. Ultrasound transducers for pulse-echo medical imaging. *IEEE Trans. Biomedical Eng.*, (8):453–481, 1983.

102. P. C. Eccardt, K. Niederer, and B. Fischer. Micromachined transducers for ultrasound applications. In *Proc. 1997 IEEE Ultrason. Symp.*, volume 2, pages 1609–1618, 1997.

103. E. D. Light, J. O. Fiering, P. A. Hultman, W. Lee, and S. W. Smith. Update of two dimensional arrays for real time volumetric and real time intracardiac imaging. In *Proc. 1999 IEEE Ultrasonics Symp*, volume 2, pages 1217–1220, 1999.

104. S. W. Smith, W. Lee, E. D. Light, J. T. Yen, P. Wolf, and S. Idriss. Two dimensional arrays for 3-d ultrasound imaging. In *Proc. 2002 IEEE Ultrason. Symp*, volume 2, pages 1545–1553, 2002.

105. H. C. Schau. Edge-connected, crossed-electrode array for two-dimensional projection and beamforming. *IEEE Trans. Signal Process.*, 39(2):289–297, 1991.

106. I. Fujishima, Y. Tamura, H. Yanagida, J. Tada, and T. Takahashi. Edge-connected, crossed-electrode array comprising non-linear transducers. In *Proc. 2009 IEEE Ultrason. Symp.*, pages 2221–2224, 2009.

107. A. Pimpin, Y. Suzuki, and N. Kasagi. Micro electrostrictive actuator with metal compliant electrodes for flow control applications. In *Proc. 17th IEEE Int Micro Electro Mechanical Systems Conf. (MEMS)*, pages 478–481, 2004.

108. A. Strachan and W. A. Goddard. Large electrostrictive strain at gigahertz frequencies in a polymer nanoactuator: Computational device design. *Applied Physics Letters*, 86(8):083103, 2005.

109. S. Resset, M. Niklaus, P. Dubois, M. Dadras, and H. Shea. Mechanical properties of electroactive polymer microactuators with ion implanted electrodes. In *Proc. SPIE 6524*, page 652410, 2007.

110. E. J. Danicki. Electrostatics of crossed arrays of strips [correspondence]. *IEEE Trans. Ultrason., Ferroelectr. Freq. Contr.*, 57(7):1701–1705, 2010.

111. E. Danicki and Y. Tasinkevych. Beam-forming electrostrictive matrix. In *Proc. 31 International Symposium on Acoustical Imaging*, volume 31. Springer, 2011.

112. E. J. Danicki. A method for analyzing periodic strips with apodization. *IEEE Trans. Ultrason., Ferroelectr. Freq. Contr.*, 55(9):1890–1894, 2008.

113. O. P. Thakur and A. K. Singh. Electrostriction and electromechanical coupling in elastic dielectrics at nanometric interfaces. *Material Science*, 27:839–850, 2009.

114. Q. Jiang and Z. B. Kuang. Stress analysis in two dimensional electrostrictive material with an elliptic rigid conductor. *Europ. J. Mech. A/Solids*, 23:945–956, 2004.

115. A. V. Ivanov, A. N. Shalygin, V. Y. Galkin, A. V. Vedyayev, and K. N. Rozanov. Metamaterials with tunable negative refractive index fabricated from amorphous ferromagnetic microwires: Magnetostatic interaction between microwires. *PIERS 2009 Mosciw Vols I and II, Proceedings*, pages 1775–1778, 2009.

116. N. V. Ryazantseva and V. V. Yachin. Electromagnetic wave scattering by rectangular-cell double-periodic magneto-dielectric gratings. *1998 International Conference on Mathematical Methods in EM Theory, Vols 1 and 2*, pages 192–194, 1998.

117. K. Y. Sirenko, Y. K. Sirenko, and N. P. Yashina. Modeling and analysis of transients in periodic gratings. ii. resonant wave scattering. *Journal of the Optical Society of America A-Optics Image Science and Vision*, 27(3):544–552, MAR 2010.

118. Shung Wu Lee. Radiation from an infinite array of parallel-plate waveguides with thick walls. *IEEE Trans. Microw. Theory Tech.*, 15(6):364–371, 1967.

119. R. I. Primich. A semi-infinite array of parallel metallic plates of finite thickness for microwave systems. *IRE Trans. Microw. Theory Tech.*, 4(3):156–166, 1956.

120. V. Galindo and C. Wu. Numerical solutions for an infinite phased array of rectangular waveguides with thick walls. *IEEE Trans. Antennas Propagat.*, 14(2):149–158, 1966.

121. Yong Cai and C. Mias. Finite-element time-domain modelling of broadside radiation from a 2d parallel-plate waveguide antenna array. In *Proc. 36th European Microwave Conf*, pages 5–8, 2006.

122. H. Toyama and K. Yasumoto. Electromagnetic scattering from periodic arrays of composite circular cylinders with cylindrical inclusions. In *Proc. IEEE Int. Workshop Antenna Technology: Small Antennas and Novel Metamaterials IWAT 2005*, pages 355–358, 2005.

123. W. H. Zhu and D. A. McNamara. Electromagnetic scattering from a nonplanar periodic conducting grating, and its equivalent surface impedance. *J. of Electromagn. Waves and Appl.*, 18(11):1485–1504, 2004.

124. E. A. N. Whitehead. The theory of parallel-plate media for microwave lenses. *Proceedings of the IEE -Part III: Radio and Communication Engineering*, 98(52):133–140, 1951.

125. V. P. Shestopalov, L. N. Litvinenko, S. A. Masalov, and V. G. Sologub. *Diffraction of waves by gratings*. Kharkov University Publishers, Kharkov, Ukraine, 1973.

126. A. Erdelyi, W. Magnus, F. Oberhettinger, and F. G. Tricomi. *Higher Transcendental Functions*, volume 1, chapter 3, page 162. McGraw-Hill, New York, 1953.

127. Y. Tasinkevych. Electromagnetic scattering by a periodic array of thick-walled parallel plate waveguides. *J. Tech. Phys.*, 50:41–53, 2009.

128. W. H. Kent and S. W. Lee. Diffraction by an infinite array of parallel strips. *J. Math. Phys*, 13(12):1926–1930, 1972.

129. E. Bausk, E. Kolosovsky, A. Kozlov, and L. Solie. Optimization of broadband uniform beam profile interdigital transducers weighted by assignment of electrode polarities. *IEEE Trans. Ultrason., Ferroelectr. Freq. Contr.*, 49(1):1–10, 2002.

130. S. V. Biryukov and V. G. Polevoi. The electrostatic problem for the saw interdigital transducers in an external electric field. i. a general solution for a limited number of electrodes. *IEEE Trans. Ultrason., Ferroelectr. Freq. Contr.*, 43(6):1150–1159, 1996.

131. Y. Tasinkevych and E. J. Danicki. Numerical efficiency of idt charge spatial spectrum evaluation methods. *Proc. 2002 IEEE Ultrason. Symp.*, pages 297–300, 2002.

132. B. P. Abbott and C. S. Hartmann. An efficient evaluation of the electrostatic fields in idts with periodic electrode sequences. In *Proc. 1993 IEEE Ultrasonics Symp.*, pages 157–160, 1993.

133. S. V. Biryukov and V. G. Polevoi. General approach to the electrostatic problem of the idt in an external electric field. In *Proc. 1995 IEEE Ultrasonics Symp.*, volume 1, pages 325–328, 1995.

134. R. C. Peach. A general approach to the electrostatic problem of the saw interdigital transducer. *IEEE Trans. Sonics Ultrason.*, 28(2):96–104, 1981.